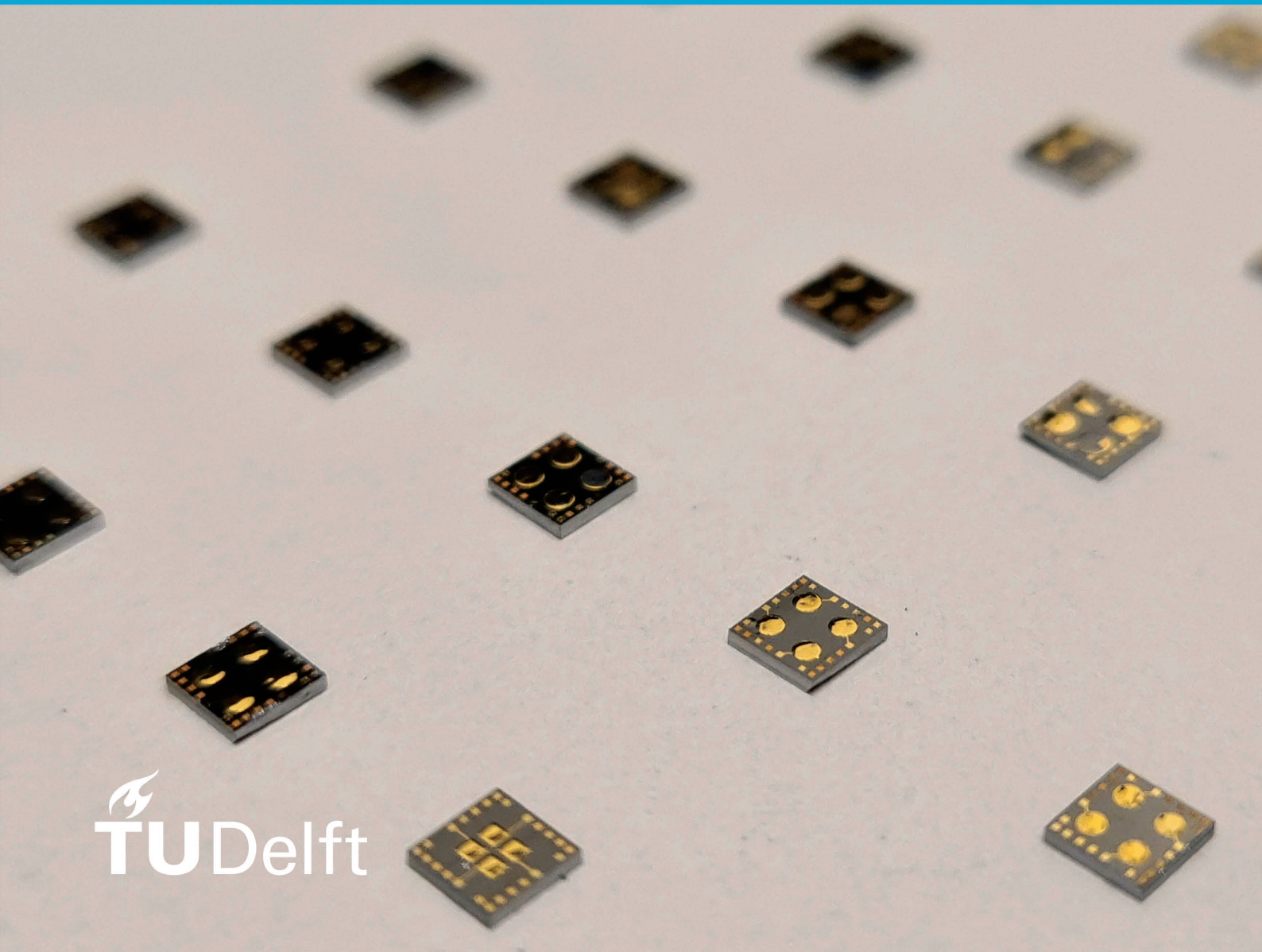


# Design, Production and Characterisation of an LPCVD-Based Poly-Silicon Carbide Pressure Sensor for Extreme Environments

Tom Salden  
2022







DESIGN, PRODUCTION AND CHARACTERISATION OF AN  
LPCVD-BASED POLY-SILICON CARBIDE PRESSURE SENSOR FOR  
EXTREME ENVIRONMENTS

A thesis submitted to the Delft University of Technology in partial fulfillment  
of the requirements for the degree of

Master of Science in Electrical Engineering

To be publicly defended on the 16th of December 2022

by

Tom Salden

Tom Salden, student number: 4430263  
*Design, Production and Characterisation of an LPCVD-based Poly-Silicon Carbide Pressure Sensor for Extreme Environments (2022)*

The work in this thesis was made in the:



Else Kooi Laboratory  
ECTM Group  
Department of Microelectronics  
Faculty of Electrical Engineering,  
Mathematics and Computer Science  
Delft University of Technology

Thesis committee:	Prof.dr. GuoQi Zhang	TU Delft	Supervisor
	Prof.dr.ir. Willem van Driel	TU Delft, Signify	
	Dr.ir. Andre Bossche	TU Delft	
	Dr.ir. Brahim El Mansouri	TU Delft	Daily supervisor

## ABSTRACT

Sensors are extremely valuable to this world. Without sensors, we would not be able to live as we do in this data-driven environment. Therefore, finding new ways to measure the matter around us is a continuous process. In this work, an addition to the new sensors is attempted, using materials that can withstand the most extreme circumstances. This work describes the process of designing, simulating, producing, measuring and validating a pressure sensor based on LPCVD Silicon Carbide.

The created sensor should be modular and back-end-of-line compatible. In addition, the sensor should measure pressures from  $80Pa$  up to  $1MPa$  at temperatures from room temperature to  $600^{\circ}C$ . Because of a favourable reaction to high temperatures, a capacitive sensor type that uses a sealed membrane for absolute pressure measurements is chosen.

Due to the large pressure range, the design has been split into three distinct parts, each with its specialised pressure range. A low-range for  $80Pa$  to  $100kPa$ , a mid-range sensor for  $100kPa$  to  $300kPa$  and a high-range sensor for  $300kPa$  to  $1MPa$ . To compensate for the nonlinearity in the device, two approaches are taken. One method splits the bottom electrodes, generating a more linear output with the correct division. This approach is used for low-and-mid-pressure devices. The other approach uses touch mode to decrease nonlinearity. After the membrane touches the bottom contact, a linear range is found. This approach is taken for the high-pressure device.

A flowchart has been developed based on the necessary layers to create the sensors. Using this flowchart, masks have been designed. During production, the process was adjusted, as delamination of the dielectric layer was observed. In addition, because of difficulty with sealing, the membrane is thicker than the original design.

During production, buckling of the membranes was observed. This causes the sensors to behave differently compared to the simulations. One effect the buckling may have caused is the reaction to temperature. This is opposite to the simulations. In addition, subjecting the sensors to a vacuum also causes behaviour opposite to what was intended. When high pressure is applied, the sensors do work as intended. Due to the design alterations and buckling effect, the sensors are less sensitive to pressure than intended. The best sensor has a sensitivity of  $0.025fF/100Pa$  compared to the designed  $0.3fF/100Pa$ . However, the output of the sensor is linear without needing the designed compensation techniques.

## ACKNOWLEDGEMENTS

During this project, a view into the world of miniature electronics is gained. In contrast to a large part of the Master Electrical Engineering, a very practical approach has been taken to complete this work. I really enjoyed this new view, and I have learned a lot during the cleanroom sessions. I would therefore like to thank my supervisor, prof. GuoQi Zhang for suggesting this department for a graduation topic and enabling me to work on this project.

Next, I would like to thank my daily supervisor, dr. Brahim El Mansouri for his incredible help during the project. With a great amount of knowledge of the cleanroom and a very practical view of the project, he could aid me in all kinds of situations. Even at difficult times, he did not hesitate to come over and help, even during weekends.

A big part of the project was spent in the cleanroom. Therefore, I would like to thank all engineers and managers to keep the lab running. A special thanks to dr. Paolo Sberna for always being extremely cheerful in the cleanroom and being very helpful with many tools and problems.

Outside of the cleanroom, I would like to thank dr. Henk van Zeijl for giving me great advice and helping me out with my project. Next, I would like to thank Filip Simjanoski for helping me with last-minute measurement issues.

Finally, I would like to express my gratitude to the members of the ECTM group. I had a great time during my thesis project, and it was made very enjoyable by the many nice researchers and master students that are members of this group. Thank you for letting me enjoy this project as much as I have!

# CONTENTS

Abstract	v
List of Tables	ix
List of Figures	x
Acronyms	xiv
1 INTRODUCTION	1
1.1 Background	1
1.1.1 Wide-Bandgap devices	2
1.1.2 Silicon Carbide	3
1.1.3 Pressure sensor	3
1.1.4 Measuring pressure	3
1.2 Motivation	4
1.3 Literature study	5
1.3.1 Current pressure sensors	5
1.3.2 Overview on state-of-the-art pressure sensor	8
1.3.3 Possible usages for high-temperature pressure sensors	10
1.4 Goals	12
1.5 Thesis outline	13
2 DESIGN	14
2.1 Theoretical approach non-touching membrane	14
2.1.1 Membrane center deflection	14
2.1.2 General membrane deflection	16
2.1.3 Capacitance of membrane	17
2.2 Mathematical Approximation touching membranes	19
2.2.1 Dielectric layer	19
2.2.2 Membrane division	19
2.3 COMSOL simulations	22
2.3.1 Creating the model	22
2.3.2 Validating mathematical model with COMSOL simulations	24
2.3.3 Temperature simulations	26
2.4 Creating designs	27
2.4.1 Design extremes	27
2.4.2 Sensitivity analysis	28
2.4.3 Increasing linearity non-touching membranes	30
2.4.4 Design decision	33
2.5 Chosen designs	34
2.6 Mask design	36
2.6.1 Mask alignment	36
2.6.2 Fabrication layers	37
2.6.3 Mask 1 - Bottom contact patterns	39
2.6.4 Mask 2 - Membrane hole etch mask	40
2.6.5 Mask 3 and 4 - Sacrificial layer definition	41
2.6.6 Mask 5 - Sensor edge definition	42
2.6.7 Mays 6 - Opening Via holes	43
2.6.8 Mask 7 - Overlay metal layer	43
3 PROCESS	44
3.1 Cleanroom processes	44
3.1.1 Contamination	44
3.1.2 Cleaning	44
3.1.3 Photoresist coating	45
3.1.4 Deposition	45
3.1.5 Etching	47



3.2	Flowchart . . . . .	48
3.2.1	Creation of overlay layer . . . . .	50
3.3	Cleanroom production . . . . .	50
3.3.1	Etch rates and deposition rates . . . . .	50
3.3.2	New wafers . . . . .	51
3.3.3	Preparation of the substrate . . . . .	52
3.3.4	Application of the passivation layer . . . . .	52
3.3.5	Construction of bottom-contacts . . . . .	53
3.3.6	Application dielectric layer including anti-stiction structures . . . . .	55
3.3.7	Construction of sacrificial structures . . . . .	57
3.3.8	Construction of the first (thin) SiC layer with release holes . . . . .	58
3.3.9	Removing of the sacrificial structures . . . . .	60
3.3.10	Construction of the thick SiC membrane . . . . .	61
3.3.11	Construction of via's to contact bottom-contacts . . . . .	62
3.3.12	Creation of overlay layer . . . . .	63
3.4	Postprocessing the wafers . . . . .	64
3.4.1	Wafer dicing . . . . .	64
3.4.2	Wire-bonding . . . . .	64
4	CHARACTERISATION SETUPS . . . . .	67
4.1	Characterisation setups inside EKL lab . . . . .	67
4.1.1	Atmospheric pressure with probestation . . . . .	67
4.1.2	Vacuum to atmospheric pressure with vacuum probe station . . . . .	68
4.2	Characterisation setup for elevated pressures . . . . .	69
4.3	Custom measurement PCB . . . . .	69
4.3.1	Measurement board list of requirements . . . . .	70
4.3.2	Component decisions . . . . .	70
4.3.3	Design of the schematic . . . . .	73
4.3.4	Design of the PCB . . . . .	73
4.3.5	Software development for the measurement board . . . . .	73
4.3.6	Validation of the PCB . . . . .	75
5	MEASUREMENTS AND CHARACTERISATION OF SENSORS . . . . .	77
5.1	Sensor production results . . . . .	77
5.1.1	Produced design values . . . . .	77
5.1.2	Compressive stress and buckling of membranes . . . . .	78
5.2	Characterisation results . . . . .	79
5.2.1	Atmospheric pressure at room temperature . . . . .	79
5.2.2	Contact division confirmation . . . . .	81
5.2.3	Atmospheric pressure at elevated temperatures to 200°C . . . . .	82
5.2.4	Elevated temperatures up to 600°C . . . . .	83
5.2.5	Vacuum to atmospheric pressure at room temperature . . . . .	84
5.2.6	Measurements at elevated pressures . . . . .	86
5.3	Verification of simulation . . . . .	86
5.3.1	Sensors at atmospheric pressure . . . . .	87
5.3.2	Sensors at elevated temperatures . . . . .	88
5.3.3	Sensors at vacuum . . . . .	89
5.3.4	Sensors at elevated pressures . . . . .	89
5.4	Conclusion . . . . .	90
6	CONCLUSION AND FUTURE WORK . . . . .	92
6.1	Future work . . . . .	92
6.1.1	Sensor design improvements . . . . .	92
6.1.2	Mask design improvements . . . . .	92
6.1.3	Process improvements . . . . .	93
6.1.4	Measurement improvements . . . . .	93
A	APPENDIX: PCB SCHEMATICS . . . . .	101

## LIST OF TABLES

Table 1.1	Material properties of Silicon Carbide and Gallium Nitride compared to Silicon [1] . . . . .	2
Table 1.2	An overview of the current state-of-the-art on pressure sensors . . . . .	9
Table 1.3	Sensor requirements for this work . . . . .	12
Table 2.1	Material properties used in the COMSOL simulations . . . . .	23
Table 2.2	Maximum design parameters for the sensor . . . . .	28
Table 2.3	Optimum normalised division of bottom electrodes . . . . .	32
Table 2.4	Chosen parameters for the design . . . . .	34
Table 2.5	Expected performance of chosen designs . . . . .	34
Table 2.6	Key fabrication layers for the sensor . . . . .	37
Table 2.7	Designed contact arrangements of bottom electrodes . . . . .	40
Table 3.1	The etch rates of the different layers using the etch techniques necessary . . . . .	51
Table 3.2	The properties of the Silicon wafers used for processing . . . . .	51
Table 3.3	The stress and bow after each deposition of silicon oxide . . . . .	57
Table 4.1	An overview of the most promising <a href="#">Capacitance to Digital Converter (CDC)</a> chips . . . . .	71
Table 5.1	The produced wafer parameters . . . . .	77
Table 5.2	Buckling factors for each sensor type . . . . .	78
Table 5.3	Designed and measured contact arrangements of bottom electrodes . . . . .	82

## LIST OF FIGURES

Figure 1.1	An illustrative example of a Pirani gauge . . . . .	6
Figure 1.2	Active implementation of a capacitive sensor. The capped cylinder is read out with electrodes on the side, which can introduce a bias voltage as well [2]. . . . .	7
Figure 1.3	Implementation of a capacitive sensor with a comb-shaped capacitor on top [3]. . . . .	7
Figure 1.4	Implementation of a touch-mode capacitive sensor. in (a), the sensor is workin in normal mode and in (b), the sensor is working in touch-mode [4]. . . . .	8
Figure 1.5	Overview of different fields that can benefit from Silicon Carbide pressure sensors . . . . .	11
Figure 2.1	An illustrative design of a capacitive pressure sensor on a substrate . . . . .	14
Figure 2.2	A 2D representation of Figure 2.1. The 3D representation can be reconstructed if this model is revolved around the dotted line. This representation is experiencing a pressure difference between the cavity and the environment . . . . .	15
Figure 2.3	Mathematical models of the centre deflection of the membrane over the pressure. $R = 200\mu m, h = 5\mu m$ . . . . .	16
Figure 2.4	Mathematical models of the membrane deflection over the radius. $P = 500kPa, h = 5\mu m$ . . . . .	17
Figure 2.5	Capacitance of the membrane calculated analytically with the small deflection model and thick membrane model and calculated numerically with the large deflection and thin membrane models. $R = 200\mu m, h = 5\mu m, g = 6\mu m$ . . . . .	19
Figure 2.6	An illustrative design of a capacitive pressure sensor on a substrate when the membrane is pushed past its maximum. The darker colours show the part of the membrane past the limit . . . . .	20
Figure 2.7	An illustrative design of the error this mathematical model makes compared to the real deformation of the membrane. The mathematical derivation is shown in orange and the real deformation is shown in red . . . . .	20
Figure 2.8	The numerically analysed radius of the touching portion of the membrane over a range of pressures. $R = 200\mu m, h = 5\mu m, g = 2\mu m$ . . . . .	21
Figure 2.9	The capacitance of a touch-mode model made in Matlab. $R = 200\mu m, h = 5\mu m, g = 2\mu m$ . . . . .	21
Figure 2.10	An example of the 2D circular model from COMSOL . . . . .	22
Figure 2.11	An example of 3D square model from COMSOL . . . . .	23
Figure 2.12	An illustration of the building blocks for the COMSOL simulation. The total model is based on a union between the blocks. . . . .	23
Figure 2.13	Comparison of the large deflection model and the COMSOL simulation. $R = 200\mu m, h = 5\mu m$ . . . . .	25
Figure 2.14	Comparison of the thick and thin membrane model and the COMSOL simulation. $R = 200\mu m, h = 5\mu m$ . . . . .	25
Figure 2.15	Comparison of the numerical model and the COMSOL simulation. $R = 200\mu m, h = 5\mu m, g = 6\mu m$ . . . . .	26

Figure 2.16	Comparison of the numerical model and the COMSOL simulation for touch-mode sensors. $R = 200\mu m$ , $h = 5\mu m$ , $g = 2\mu m$	26
Figure 2.17	Temperature simulation of a sensor. $R = 200\mu m$ , $h = 5\mu m$ , $g = 2\mu m$	27
Figure 2.18	Sensitivity function of the sensor using the small-deflection and thick-membrane models. $R = 200\mu m$ , $h = 5\mu m$ , $g = 6\mu m$	29
Figure 2.19	Capacitance of a model that has the maximum design parameters. $R = 370\mu m$ , $h = 5\mu m$ , $g = 14\mu m$	30
Figure 2.20	Capacitance per pressure of two membrane parts, a centre part and an outside ring. $R = 200\mu m$ , $h = 5\mu m$ , $g = 6\mu m$	31
Figure 2.21	An illustrative design showing isolated contacts at the bottom of the sensor, displayed in yellow (inner electrode) and green (outer electrode)	31
Figure 2.22	The result of Matlab optimization	32
Figure 2.23	Optimum division of bottom electrodes. Neighbouring electrodes have opposite capacitances	32
Figure 2.24	Results from different designs that measure from $80Pa$ up to a specified pressure	33
Figure 2.25	Simulated response of the low-pressure sensor design	35
Figure 2.26	Simulated response of the mid-range pressure sensor	35
Figure 2.27	Simulated response of the high-range pressure sensor	35
Figure 2.28	A photo of one of the masks used for processing	36
Figure 2.29	The two different alignment marker designs used on the wafer	37
Figure 2.30	Two different die designs for Mask 1	40
Figure 2.31	Zoomed-in illustration of mask 1 of a circular sensor with 5 bottom contacts. Different colours are used to differentiate between the individual contacts	41
Figure 2.32	Zoomed-in design of Mask 2	41
Figure 2.33	Circular design of Mask 3 and Mask 4	42
Figure 2.34	An illustration of isotropic etching	42
Figure 2.35	The universal die design of Mask 6	43
Figure 2.36	A design for Mask 7	43
Figure 3.1	The stages of the process as described in the flowchart	48
Figure 3.2	Illustration of using step heights to determine the amount etched from a mask and the material	51
Figure 3.3	Alignment of the alignment mark with mask 1	53
Figure 3.4	Etched Molybdenum contacts using dry-etching. A combination of four microscope photos are stitched together for this result	54
Figure 3.5	Wet etching using a hard mask	54
Figure 3.6	A circular sensor after etching the anti-stiction holes	55
Figure 3.7	Delamination after Low Pressure Chemical Vapour Deposition (LPCVD) Silicon Carbide (SiC) deposition	56
Figure 3.8	Result of sacrificial structure formation	58
Figure 3.9	Uneven etching of the sacrificial oxide around the contact area	59
Figure 3.10	Step coverage of a photoresist layer at the edge of a $14\mu m$ square membrane	60
Figure 3.11	Visual confirmation of the step coverage using the Keyence VK-X250	60
Figure 3.12	The result of etching the sacrificial layer halfway during the process	61
Figure 3.13	Carefully pressing on a released membrane to see if it is released correctly	61
Figure 3.14	An image of a sealed release hole, taken by the electron microscope	62
Figure 3.15	Irregularities of the via holes due to hardened photoresist	63

Figure 3.16	The resulting wafer after processing is finished . . . . .	64
Figure 3.17	Dicing machine in the process of cutting through the substrate	65
Figure 3.18	Two connections to the die, a soldering connection on the left side and a wire-bonded connection on the right side . . . . .	65
Figure 3.19	Delamination of contacts after aluminium-silicon was deposited on top of the chromium-gold layer . . . . .	66
Figure 4.1	Probe station connection with a sensor using one of the needles	67
Figure 4.2	Measurement setup of Cascade 33 probe station . . . . .	68
Figure 4.3	Probe station connection with a die using the Nextron vacuum probe station . . . . .	68
Figure 4.4	Measurement setup of Nextron Vacuum probe station . . . . .	69
Figure 4.5	The setup for pressure measurements using the custom PCB .	70
Figure 4.6	The distribution of different contacts to three six-channel CDC chips . . . . .	71
Figure 4.7	The working principle of the PCAPo4 CDC chips . . . . .	72
Figure 4.8	PCAPo4 integration schematics . . . . .	74
Figure 4.9	The main screen of the webserver hosted by the ESP32 device	74
Figure 5.1	Buckling mode in the literature compared to this work . . . . .	78
Figure 5.2	Different modes of buckling in produced membranes . . . . .	79
Figure 5.3	Example of a circular buckling sensor with a low centre . . . .	80
Figure 5.4	Measurements of circular sensors with a buckling membrane, with a membrane height of $6.75\mu m$ at room temperature and atmospheric pressure . . . . .	80
Figure 5.5	Measurements of circular sensors with a membrane height of $6.75\mu m$ at room temperature and atmospheric pressure . . .	80
Figure 5.6	Measurements of circular sensors with a membrane height of $12.74\mu m$ at room temperature and atmospheric pressure . . .	81
Figure 5.7	Measurements of square sensors with a membrane height of $6.75\mu m$ at room temperature and atmospheric pressure . . . . .	81
Figure 5.8	Measurements of square sensors with a membrane height of $12.74\mu m$ at room temperature and atmospheric pressure . . . .	82
Figure 5.9	Temperature measurements of circular membranes with a height of $6.75\mu m$ and a buckled membrane . . . . .	82
Figure 5.10	Temperature measurements of circular membranes with a height of $12.74\mu m$ . . . . .	83
Figure 5.11	Temperature measurements of a circular membrane compared to a square membrane, both with a height of $12.74\mu m$ . . . . .	83
Figure 5.12	Measurement and calibration setup in the Nextron Vacuum probe station . . . . .	84
Figure 5.13	High-temperature measurements of circular and square sensors with both $6.75\mu m$ and $12.74\mu m$ height . . . . .	84
Figure 5.14	Pressure measurements of high circular sensors . . . . .	85
Figure 5.15	Pressure measurements of low circular sensors, from $80Pa$ to $100kPa$ . Two sensors are displayed, one with a radius of $500\mu m$ (left y-axis) and one with a radius of $400\mu m$ (right y-axis) . . . . .	85
Figure 5.16	Unfiltered high-pressure measurement of a low circular membrane with radius of $400\mu m$ . . . . .	86
Figure 5.17	Measurement results of two circular and one square sensor .	86
Figure 5.18	Measurements of sensors at elevated pressures . . . . .	87
Figure 5.19	Adjusted simulation including a high-centre buckling effect .	88
Figure 5.20	Measurements compared to the simulation of membranes at ambient pressure . . . . .	88
Figure 5.21	Measurements compared to the simulation of circular membranes at elevated temperatures . . . . .	89



Figure 5.22	Measurements compared to simulation of circular membranes at low pressures . . . . .	89
Figure 5.23	Simulations and measurements of low circular membranes at high-pressure. Membranes with $500\mu m$ radius use the left y-axis and membranes with $400\mu m$ radius use the right y-axis . . . . .	90
Figure 5.24	Simulation and measurement of a high circular membrane at high pressure . . . . .	90
Figure A.1	Schematic design for the PCB power design . . . . .	101
Figure A.2	PCAPo4 integration schematics . . . . .	102
Figure A.3	Schematic design for the Microcontroller, temperature sensor and piezoresistive readout . . . . .	103
Figure A.4	Schematic design for the SD card slot, buttons and indicator lights . . . . .	104
Figure A.5	Schematic design of the full PCB . . . . .	104

## ACRONYMS

BEOL	Back-end-of-line.
BHF	Buffered hydrofluoric acid.
CDC	Capacitance to Digital Converter.
DRIE	Deep Reactive Ion Etching.
DUT	Device Under Test.
EKL	Else Kooi Laboratory.
FADEC	Full Authority Digital Engine Control.
FEM	Finite Element Modelling.
IPA	Isopropyl alcohol.
LPCVD	Low Pressure Chemical Vapour Deposition.
NMP	1-methyl-2-pyrrolidone.
PCB	Printed Circuit Board.
PECVD	Plasma-enhanced chemical vapor deposition.
Si	Silicon.
Si <sub>3</sub> N <sub>4</sub>	Silicon Nitride.
SiC	Silicon Carbide.
SiO <sub>2</sub>	Silicon dioxide.
TEOS	Tetraethyl orthosilicate.
WBG	Wide-bandgap.

This chapter gives an introduction to this thesis work. First, a background with information about wide-bandgap devices and pressure sensors, in general, is given. Then the motivation for this work is explained. Finally, a literature review is given and the thesis goals are described.

## 1.1 BACKGROUND

We live in a world made up of an incredible variety of matter. This matter not only comes in many different elements, but combinations between those elements also exist. In addition, different states of matter expand these combinations even more.

This unique variety and the properties that matter can have, look pretty normal to us in daily life. Because we are accustomed to the world, including the very complex behaviour of this matter, we tend to take the possibilities we have for granted. However, over time, we gradually learned more about how matter interacts and how we can benefit from this behaviour. As a result, we created physical laws and theories that correctly model and describe the essence of what happens around us.

In this day and age, we can harness these properties and create sensors to visualise how matter behaves. These sensors can give us detailed information about the states of interest. In addition, we learn new and more accurate methods of reading the properties as we progress.

However, as technology improves and the need for more detailed sensors increases, new developments must be made. At this time, almost all computers and sensors are based on one material: [Silicon \(Si\)](#). While this material is highly suitable for these applications, some drawbacks are encountered. These drawbacks especially show themselves when using the material in extreme situations.

One example of an extreme situation, and the main focus of this work, is high temperature. Active silicon devices generally have a maximum temperature of around 125 – 150°C [5]. The reason is that with a temperature increase, leakage currents also increase. These currents alone degrade the reliability of the device. However, when the leakage current gets too big, devices can break due to short-circuiting [6]. The reason for leakage currents is that thermal energy is transmitted to electrons inside the silicon at higher temperatures. The energised electrons can break away from their covalent bonds, allowing them to travel throughout the lattice [7]. Inside active silicon devices, carefully doped areas contain a shortage or surplus of electrons. This limits or forces the silicon to conduct in specific manners. With an increase in free electrons, these areas will become less effective. Eventually, the effect of free electrons will dominate over the doped regions. Once this occurs, leakage currents will start to appear and break the device [8]. The charges induced by temperature are intrinsic charges, and the concentration of these charges can be calculated using [Equation 1.1](#).

$$n_i = \sqrt{N_C N_V} e^{-E_G/2kT} \quad (1.1)$$

In this equation,  $n_i$  is the concentration of intrinsic carriers in  $cm^{-3}$ .  $N_C$  and  $N_V$  are the material's electron and hole density of states.  $E_G$  is the energy bandgap,  $k$

is the Boltzmann constant and  $T$  is the temperature of the material. The higher the temperature, the more intrinsic charges can dominate the doped regions.

### 1.1.1 Wide-Bandgap devices

To solve these drawbacks, researchers are looking into [Wide-bandgap \(WBG\)](#) materials as a substitute for silicon. The reason for looking into these specific materials is that wide-bandgap devices are much more resilient to high temperatures. As the name implies, these materials have a larger electron bandgap, meaning that more energy is necessary for electrons to break free of their covalent bonding. Using [Equation 1.1](#), it is visible that a higher bandgap leads to a lower intrinsic charge concentration at the same temperature. Therefore, a higher temperature is necessary to free the same amount of electrons in wide-bandgap materials compared to silicon. As a result, active devices made from wide-bandgap materials keep working at temperatures that silicon cannot [8]. In addition, these materials have a high saturated drift velocity and electron mobility. These properties allow devices to have higher switching speeds. Next, the materials have a high critical breakdown electric field, allowing circuits to handle higher voltages or make smaller circuits in all dimensions [1, 9, 10]. Finally, these materials tend to be more resistant to applied radiation and are especially resilient to a larger amount of neutrons passing through them. The amount of neutrons passing through is measured in neutron fluence, and the maximum these materials can handle is two orders of magnitude larger than silicon [11, 12]. A summary of the material properties can be seen in [Table 1.1](#). A comparison between silicon and the wide-bandgap materials silicon carbide and gallium nitride has been made.

**Table 1.1:** Material properties of Silicon Carbide and Gallium Nitride compared to Silicon [1]

Material property	Silicon	Silicon Carbide	Gallium Nitride
Band gap [eV]	1.1	3.2	3.4
Critical Field [V/cm]	$0.3 \times 10^6$	$3 \times 10^6$	$3.5 \times 10^6$
Electron mobility [ $\text{cm}^2/\text{V} \cdot \text{s}$ ]	1450	900	2000
Electron Saturation Velocity [cm/sec]	$10 \times 10^6$	$22 \times 10^6$	$25 \times 10^6$
Thermal Conductivity [Watts/ $\text{cm}^2 \cdot \text{K}$ ]	1.5	5	1.3
Maximum Operating Temperature [°C]	150	Up to 600	Up to 600

Even though wide-bandgap materials have promising properties, these materials have yet to take over silicon. There are still some hurdles to overcome before designers can widely use the techniques and materials. Because silicon has been the standard material, most processes are optimised for the specific properties of silicon. When switching to wide-bandgap materials, manufacturing has to be modified for the new materials. Perfecting these manufacturing methods takes time, and until then, materials will suffer from lower reliability. This reduced reliability lies in the fact that manufacturing introduces defects that need to be fully understood. In addition to improving reliability, the production price is not competitive with silicon yet. Finally, the new materials have yet to be modelled completely. This lack of models makes it difficult to simulate the behaviour and design devices with these materials [1]. Therefore, to properly use these materials' advantages, they must first be thoroughly understood and characterised.

### 1.1.2 Silicon Carbide

One of the Wide-Bandgap materials is Silicon Carbide. This promising material is especially suited for high-temperature applications due to its high thermal conductivity [1]. A comparison including the thermal conductivity is shown in Table 1.1.

From this material, a variety of different devices have been created. High-power transistors have been successfully made in the form of MOSFETs and JFETs, and sensors like gas sensors, pressure sensors and optical sensors [11, 13, 14]. The variety of existing devices shows how promising the material is. However, there are still improvements possible. Because of the high chemical stability, several processing steps, like Deep Reactive Ion Etching (DRIE), are much harder with Silicon Carbide compared to Silicon. Therefore, optimising processes based on ease of fabrication is a valuable improvement for reliability and manufacturing costs.

### 1.1.3 Pressure sensor

This work will focus on a pressure sensor made from Silicon Carbide. While there are some excellent designs for pressure sensors in Silicon or Silicon Carbide, as shown in Section 1.3, this work will shine a light on some additional improvements compared to the listed results.

As mentioned, Silicon Carbide is a material specifically suited for high-temperature applications. Due to this fact, the pressure sensor has requirements that match these high-temperature performances. This work will create a sensor that should measure at temperatures up to 600 °C in theory. This work will test the temperature sensitivity of this sensor to a range that is possible using the measurement set-up available. In addition, the pressure range this specific sensor will work on is 80 Pa to 1 MPa.

Furthermore, this sensor should be modular and Back-end-of-line (BEOL) compatible. This means that the sensor should be placeable anywhere on the wafer and that the processes used for the wafer production should not interfere with already existing structures in the wafer. For example, extreme fabrication temperatures can not be used since this can influence the doping concentrations present in the wafer if transistors are already made in the substrate.

### 1.1.4 Measuring pressure

Before this sensor is created, it is important to understand what underlying physical phenomena are at work and what pressure is exactly. As a starting point, the definition of this phenomenon needs to be clarified. Pressure is described in the unit of Pa. This unit can be defined as  $\text{N m}^{-2}$  or as  $\text{kg m}^{-1} \text{s}^{-2}$  in SI units [15]. In other words, pressure is defined as the perpendicular force on a certain area. The cause of pressure can be anything that creates this force. For example, in the atmosphere, pressure is caused by the gas present. This is because the particles in the gas are free to move. Once a particle hits an object, the particle's momentum exerts a force on the area. Physically, it means that particles that bump into an object generate a force on the object in the form of pressure.

Now that pressure is defined, the next step is to determine how to measure it. Since pressure is caused by the number of collisions between ambient particles and objects, pressure can either be linked to the number of particles or the force each particle exerts. There are several techniques for reading this force on an area. These techniques can be divided into two categories: environmental deviation and differential pressure. The first category, environmental deviation, measures pressure by evaluating a change in the ambient particles. Either a difference in the number of particles or the momentum of the particles is measured in this category. The second category, differential pressure, evaluates the force by measuring the difference between two pressures. For both categories, there are different approaches to reading the pressure.



### *Environmental deviation*

The first category uses the environmental properties under specific pressure. As mentioned, a different pressure can either be related to the number of particles or the force each particle applies.

The pressure can be derived if one of these parameters can be measured. When there is a different number of particles, not only the pressure is influenced, but also the thermal conductivity of the ambient gas. When there are fewer particles, the thermal energy will not be transmitted as well as when there are more particles. Therefore, pressure and thermal conductivity can be linked to each other. The thermal conductivity for all types of gas grows with a rising pressure [16]. Pirani gauges are devices that use this property to measure pressure. More information about the sensors and the current state of development is shown in [Section 1.3](#)

### *Differential pressure*

In addition to using environmental properties to measure pressure, differential pressure sensors are another category of sensors. These sensors use the difference between two different pressures. If one of the pressures is a known, fixed pressure, then the measured pressure can be related to the known pressure. This means that creating an absolute pressure sensor is possible. If neither of the pressures is known or fixed, a relative pressure difference between the two can be measured.

One method of obtaining this measurement is by using a thin membrane. The force that the pressure differential creates causes the membrane to deform. In turn, this deformation is read and translated to a pressure level [17–21]. Reading this deformation can be done using capacitive or piezoresistive means, among others.

In [Section 1.3](#), the differences between the techniques are highlighted, and the advantages and disadvantages of each technique are displayed.

## 1.2 MOTIVATION

Technology is progressing with enormous speed, and the silicon industry is slowly searching for materials that are more suited for harsh environments and increase power efficiency. Silicon Carbide is one of the materials that promise these improvements. Therefore, it is essential to research this material's possibilities. In addition, research has to be done on how the material can best be processed for the purposes necessary.

It is a fact that the industry is used to the possibilities and limitations of Silicon. The result is that designs and manufacturing are designed on the limits of this material. Because of this proven material, it is hard to introduce a new contender. The first step is to show what this contender is capable of. Therefore, the best method to make the industry aware of the superior properties of SiC is to produce results. By showing the capabilities of this material, the industry will eventually pick up and start designing for the new limitations. Therefore, research must do its best to advance as far as possible with this material until this moment.

Advancements will be done on one device at a time. Once enough devices and applications have been examined, more complex combinations of sensors and circuitry can be implemented. At that stage, production can be generalised and optimised for this material.

This work aims to aid in the search for what is possible with this material. By making a modular sensor implemented at the BEOL, flexibility with the processes has to be discovered, and limits on the production have to be found. Especially since the development should be possible in an existing cleanroom with limited possibilities for Silicon Carbide, in the case of this work, the [Else Kooi Laboratory \(EKL\)](#) should be able to process this material and make devices from it.

## 1.3 LITERATURE STUDY

Before creating a sensor on a chip, the current state of the technology needs to be investigated. This will ensure that the sensor in this work has not already been designed elsewhere. In addition, a feeling for the possibilities with the technology is gained.

### 1.3.1 Current pressure sensors

In previous sections, possible sensor readout methods have been discussed. Since these are the most prevalent technologies used in literature, this study will evaluate these methods. Even though there are other methods of reading pressure, the literature study will be limited to Pirani gauges, capacitive differential pressure readouts and piezoresistive differential pressure readouts. After discussing the advantages and disadvantages of each sensor type, a table will be shown that summarises the current literature.

#### *Pirani Gauges*

Like mentioned in [Section 1.1.4](#), Pirani gauges work on the principle that an increase in pressure also brings an increase in thermal conductivity. These devices consist of a heated filament. Due to the thermal conductivity of the gas, a portion of this heat is lost. The gas molecules that bump into the filament take some thermal energy and convert it to motion. This in turn cools down the filament. If the pressure increases, relatively more gas molecules bump into the wire. Therefore, at higher pressure, more heat is lost [\[22\]](#). This device's disadvantage is that it depends on the specific gas composition. A different type of gas has a different thermal conductivity, which influences the measurement [\[23\]](#). Therefore, to measure the absolute pressure, knowing the exact composition of the environmental gas is necessary. The advantage of this type of device is that it has a very low power consumption and a high sensitivity in a large dynamic range. In addition, the readout is linear, as the thermal conductivity is proportional to the pressure.

This type of device has been miniaturised and included on-chip. In addition, it is compatible with wide-bandgap materials [\[24\]](#). Using exotic materials, even more extreme temperatures of 1600°C have been reached, using Sapphire as a heated filament [\[25\]](#).

The illustration in [Figure 1.1](#) shows an illustration of such a device. By sending current through the filament, displayed in orange, the free-hanging filament heats up. The thermal energy is then dissipated with four different processes. The total heat losses consist of thermal convection, thermal radiation, thermal conduction through touching structures and thermal conduction through the gas. Thermal convection and thermal conduction through the gas are directly linked to heat loss caused by the surrounding gas. However, only the thermal conduction through the gas is directly linked to pressure [\[24\]](#).

#### *Capacitive readout*

Capacitive sensors work on the principle that two conductors close to each other form a capacitance with each other. The value of a capacitance can be defined by the area of the contacts, the distance between the contacts and the permittivity of the material between the contacts. The relation between these properties can be summarised as shown in [Equation 1.2](#). Here,  $C$  is the capacitance value in Farad,

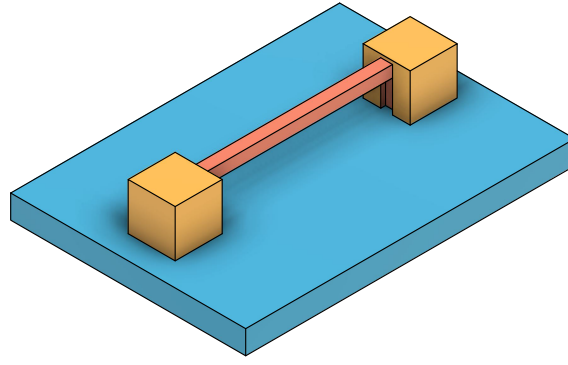


Figure 1.1: An illustrative example of a Pirani gauge

$\epsilon$  is the permittivity of the material between the contacts,  $A$  is the area in square meters, and  $d$  is the distance between the contacts in meters.

$$C = \epsilon \frac{A}{d} \quad (1.2)$$

By using the fact that a change in distance means a proportional change in capacitance, a pressure sensor can be constructed. This type of pressure sensor usually has a flexible membrane. The exact position of the membrane depends on the pressure inside of the membrane compared to the pressure outside of the membrane. If the inside pressure is higher, the membrane will bulge up and if the pressure is lower, the membrane will be pulled in.

The first conductor used in this sensor is usually placed in the area under the membrane. The membrane itself can now be used as the second electrode. Since the two conducting areas are close to each other, a capacitance is formed. And since the capacitance depends on the distance between the two plates when the membrane moves, the capacitance will change as well [26].

Unfortunately, during deformation, the centre of the membrane will have the highest deformation because it is the least constrained. In comparison, the sides of the membrane move very little or not at all. This difference in distance between contacts will result in non-linear behaviour. As a result of this disadvantage, there have been multiple attempts to create a more linear response using the membrane and capacitive readout.

While most sensors have electrodes that are shaped similarly to the membrane, one work tries to optimise the electrode shape. Instead of using a circular or rectangular membrane shape, it uses an irregular shape that can cancel out the nonlinearity [3].

Next to improving the electrode shape, sensors with servo-controlled feedback have been attempted as well [2, 27]. One implementation is seen in Figure 1.2 This implementation uses a capped cylinder. The sides of this cylinder are used for readout and to apply a voltage potential. This potential introduces an electrostatic force that opposes the force created by the pressure. By effectively pulling back the deformed membrane, this technique increases linearity a little. However, this technique is very effective in gaining a higher sensitivity. This particular implementation has an increase in sensitivity of 33% compared to the same sensor without voltage feedback [2].

Another technique to increase linearity is to use a different structure on top of the membrane to create a capacitance. An example is to use a comb structure on top of the moving membrane. By using the distance change of only the centre of the membrane, the capacitance change of this comb structure is more linear than using the membrane itself [3]. The implementation is visible in Figure 1.3.

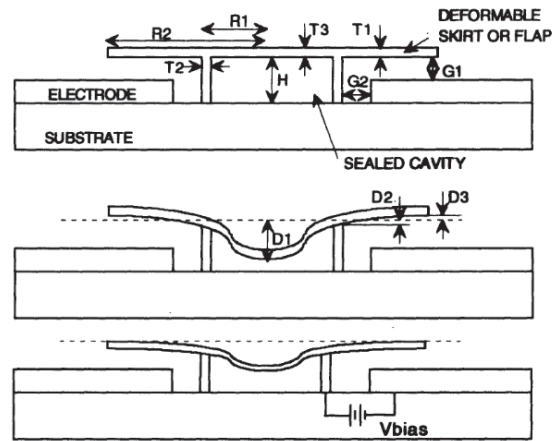


Figure 1.2: Active implementation of a capacitive sensor. The capped cylinder is read out with electrodes on the side, which can introduce a bias voltage as well [2].

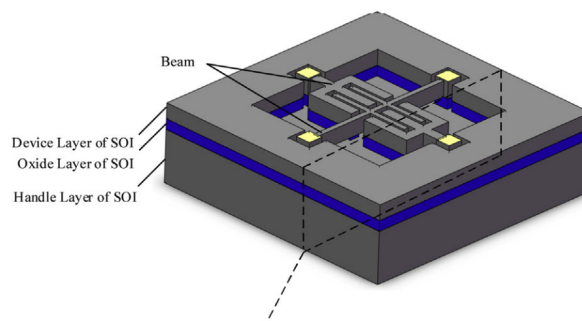


Figure 1.3: Implementation of a capacitive sensor with a comb-shaped capacitor on top [3].

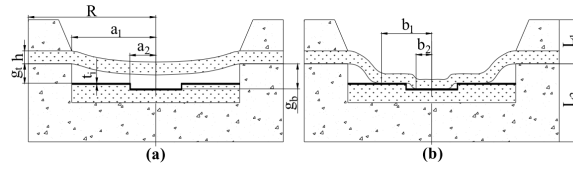


Figure 1.4: Implementation of a touch-mode capacitive sensor. in (a), the sensor is workin in normal mode and in (b), the sensor is working in touch-mode [4].

Finally, a common technique to increase the linearity of the sensor is to allow the membrane to touch the bottom of the cavity [4, 28]. At this point, the sensor is in 'touch mode', and the readout enters a linear area. At a certain pressure, the saturation point is reached, where the readout stops being linear. These sensors can be used in low pressures, where the membrane does not yet touch. In addition, the sensor can be used in higher pressure, where the membrane touches the bottom of the cavity. The linear range is limited to a specific pressure range, depending on the sizes of the design. An illustration of this type of sensor is shown in Figure 1.4.

### Piezoresistive readout

Just as with a capacitive sensor, a piezoresistive sensor uses the movement of the membrane to derive pressure. However, instead of using the capacitance between two conductors, it uses the piezoresistive effect. This effect causes a change in resistance when the material is under stress. Most semiconductors exhibit piezoresistive behaviour. For example, Si has a significant gauge factor. The higher the gauge factor, the more piezoresistive the material behaves. Piezoresistive sensors in silicon have therefore been successfully made. However, at elevated temperatures, the silicon sensor decrease in sensitivity. The reason for this decrease in sensitivity is that the gauge factor is temperature-dependent. And at elevated temperatures, this factor rapidly decays [29]. On the other hand, SiC has a gauge factor 3-5 times smaller than Si. However, this gauge factor decays less quickly at higher temperatures. To illustrate, at 400 degrees, Si has no gauge factor left, but only 50% of the gauge factor is lost for SiC [29].

There are two methods of implementing piezoresistive readout sensors. The first method is to place piezoresistors on top of the moving membrane. This can be done directly on the membrane [18, 19, 21, 30] or suspended above the membrane [31]. The advantage of directly placing the piezoresistors on the membrane is that it is straightforward to implement a Wheatstone bride. The advantage of using a suspended piezoresistor is that the sensitivity is increased significantly.

The second method of implementing a piezoresistive sensor is to use the material of the membrane itself. Since the membrane is created from SiC, reading the resistance over the points where the most stress occurs will give a change with changing pressure. This means that the extra processing steps to add a piezoresistor are omitted [17].

### 1.3.2 Overview on state-of-the-art pressure sensor

Now the different types of sensors have been discussed, including the advantages and disadvantages, current state-of-the-art sensors can be compared in a table. In Table 1.2, some of the literature of pressure sensors is summarised. The materials of the designs are broad. Even though this work will use Silicon Carbide, it is valuable to compare to other materials as well. The design parameters of the works include the method of measuring and the basic dimensions of the sensor if applicable. Here,  $R$  is the radius of a circular membrane.  $w$  is the width of a rectangular membrane.  $h$  is the thickness of the membrane and  $g$  is the size of the gap between the membrane and the substrate. Additionally, the sensitivity and pressure range are displayed.



The maximum temperature is the temperature on which the work has tested their sensor. Finally, additional notes and the reference to the work is shown.

**Table 1.2:** An overview of the current state-of-the-art on pressure sensors

Material	Design parameters	Sensitivity	Pressure range	Maximum temp.	Notes	Ref.
AlGaIn/ GaIn sensing unit	Piezo- electric readout, enhanced via 2DEG	$22.8\%/kPa$	0.01 kPa to 96 kPa	100 °C	-	[18]
3C-SiC mem- brane on 6H-SiC substrate	Capacitive readout $R = 200\mu m$ $h = 2\mu m$ $g = 5\mu m$	$3.5pF/MPa$	0.9 MPa to 1.4 MPa	500 °C	A double- notch de- sign	[4]
Poly 3C-SiC mem- brane on 4H-SiC substrate	Piezoresistive readout $w = 300\mu m$ $h = 2.7\mu m$	$1.6 \times 10^{-3}$ $\Delta R/Rbar^{-1}$	10 Pa to 100 kPa	124 °C	Square mem- brane	[17]
Si mem- brane on glass substrate	Capacitive readout $R = 500\mu m$ $h = 9.7\mu m$ $g = 10\mu m$	$1.21fF/kPa$	20 kPa to 100 kPa	400 °C	Servo controlled feedback	[32]
Si mem- brane on Si substrate	Capacitive readout $R = 7.35mm$ $h = 30\mu m$ $g = 20mm$		0 bar to 5 bar	70 °C	Optimized electrode shape	[33]
4H-SiC substrate and mem- brane	Piezoresistive readout	$3.4mV/MPa$	0 MPa to 7 MPa	500 °C	DRIE etching used and bottom is closed with ex- ternal structure	[19]
Poly SiC mem- brane	Touch-mode capacitive readout $R = 180\mu m$ $h = 5\mu m$ $g = 2\mu m$		7.5 MPa to 20 MPa	400 °C	Only sim- ulated re- sults	[34]
a-SiC mem- brane on Si substrate	Piezoresistive readout $w = 1800\mu m$ $h = 30\mu m$	$3.90mV/PSI$	0 to 12 psi	room temp	DRIE etching at back of substrate	[30]

4H-SiC membrane and substrate	Piezoresistive				Mass fabrication using femtosecond laser	[20]
Poly-SiC on Si substrate	Pirani Gauge	$0.47\Omega/Pa$	10 Pa to 100 kPa	750 °C		[24]
SOI substrate and SOI membrane	Capacitive with comb structure on membrane	$17aF/Pf$	0 kPa to 30 kPa	150 °C	Comb structure adds linearity to the device	[3]
SiC membrane on SiC substrate	Capacitive readout $R = 47\mu m$ $h = 3\mu m$ $g = 1.5\mu m$	$1.2 \times 10^{-2} fF/Pa$	0 MPa to 4.83 MPa	500 °C	Comparing Si and SiC membranes	[35]
Si membrane with Si substrate	Piezoresistive readout $w = 120\mu m$ $h = 5\mu m$ $g = 2\mu m$	$7.979 fF/bar$	0 kPa to 160 kPa	room temp		[26]
Silicon substrate between top glass and bottom glass	Touch-mode capacitive readout $w = 2800\mu m$ $h = 6.5\mu m$ $g = 4.3\mu m$	$28.1 fF/Pa$	150 Pa to 1000 Pa	100 °C		[36]
SiC membrane on SiC substrate	Touch-mode capacitive readout $R = 136\mu m$ $h = 3\mu m$ $g = 1.5\mu m$	$251\mu V/psi$	1.4 MPa to 3.2 MPa	600 °C	Produced for in-cylinder motor pressure sensing	[37]
Si membrane on SOI substrate	Piezoresistive $w = 1000\mu m$ $h = 350\mu m$	$1.1126 mV/MPa$	0 MPa to 150 MPa	200 °C		[38]
SiC piezoresistors on Si substrate	Piezoresistive readout		0 to 500 mbar	room temp	3C-SiC nanowires used for piezoelectric effect	[31]

### 1.3.3 Possible usages for high-temperature pressure sensors

In previous sections, the distinct advantages of wide-bandgap devices have been illustrated. In addition, the different pressure sensors that have been made using these materials have been listed. However, because the motivation states that this research has been done with the industry in mind, specific uses for these sensors still have to be discovered. If there are no use cases where silicon carbide pressure sensors have a clear advantage compared to silicon sensors, then this research will not contribute to the industry. Because of the novelty of this material, there is no

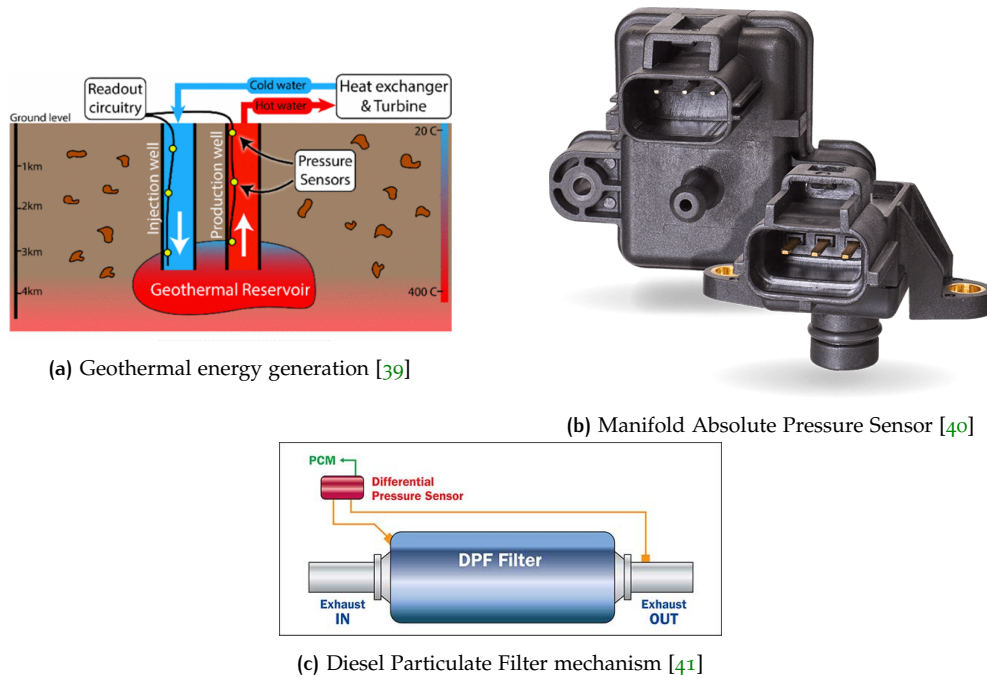


Figure 1.5: Overview of different fields that can benefit from Silicon Carbide pressure sensors

real proven use case for silicon carbide pressure sensors, but possible scenarios can be suggested.

Because of the promising possibilities that these materials bring, use cases that benefit specifically from the material properties are considered the most applicable. A few of the proposed fields where this kind of sensors can be useful are as follows:

**Geothermal wells:** During the search for green energy sources as alternatives to sources that emit greenhouse gasses, many different approaches are evaluated. One of these approaches is geothermal energy. This proposed idea uses heat that is emitted by the earth's core. By circulating fluids to the high temperature inside of the earth, energy can be retrieved and used for electricity generation. The mechanism is depicted in Figure 1.5a. Even though the idea is simple, the implementation is not trivial. The reason is that the temperature and pressure have to be monitored constantly. And with temperatures up to  $400^{\circ}\text{C}$ , normal silicon sensors are not suitable. Silicon carbide sensors can be the solution for this application [39].

**Automotive industry:** The automotive industry already uses pressure sensors to control pressures in the engine, filters, oil reservoirs and more. Most of these sensors are not placed directly inside the environment that should be measured but are placed in areas where the temperatures are manageable for the sensors. This introduces more components, complexity and weight. Silicon carbide sensors could be placed in these harsh environments directly, enabling more precise measurements and reduced complexity. Two examples of sensors used in the automotive industry will be given.

The first example of a sensor that is used in the automotive industry is the MAP sensor. This Manifold Absolute Pressure Sensor measures the absolute pressure inside the engine and as a result it can determine the intake airflow. The sensor should measure between 0 and  $100\text{kPa}$ , and temperatures inside the motor can reach up to  $200^{\circ}\text{C}$  [42]. A depiction of the sensor can be seen in Figure 1.5b.

The second example is a Diesel Particulate Filter Differential Pressure Sensor. This sensor measures the exhaust backpressure caused by a clogged filter. It signals the control module if there is too much diesel particulate present, and the sensor should be cleared. The particulate can get  $600^{\circ}\text{C}$ , and the pressure the chamber can reach is  $100\text{kPa}$  [43, 44]. At this moment, the sensor is placed away from the motor, connected with silicon tubes, as shown in Figure 1.5c.

**Industrial industry:** Next to the automotive industry, the industrial industry has some use cases as well. In laboratory and production facilities, vacuum annealing is used. This is a technique that heats up a part and slowly cools it to obtain a softer structure of the part. As the name implies, this is done in a vacuum. Vacuum levels of  $0.1\text{Pa}$  are used at temperatures up to  $650^{\circ}\text{C}$  [45, 46]. Next to annealing, vacuum tempering is another technique that is used. This technique releases stress from components and adjusts hardness and ductility. This is done at about  $300^{\circ}\text{C}$  and at vacuum levels up to  $10\text{Pa}$  [47–49]. Finally, a vacuum oven is an example that puts sensors in extreme environments. A vacuum oven is mostly used as laboratory equipment. Because of their versatility, the ovens should resist various chemical compounds, and they can be designed to handle temperatures from 200 to  $1000^{\circ}\text{C}$  at  $0.133\text{kPa}$  vacuum level [50].

These industrial applications feature extreme temperatures that silicon chips cannot reach. Devices like these could benefit from sensors that can be placed inside these harsh environments.

**Avionics and space:** The final category is avionics and spaceflight. Avionics mostly benefit from the high-temperature reach. An example is a pressure sensor inside the [Full Authority Digital Engine Control \(FADEC\)](#) system. This sensor should detect  $70\text{Pa}$  peak-to-peak fluctuations and operate in temperatures from  $54$  to  $400^{\circ}\text{C}$  [51]. Unlike most other use cases, space missions benefit not only from the temperature range but also from the fact that the materials are better resistant to radiation. Nasa is using Silicon Carbide sensors in its mission to Venus. The planet's temperature is  $460^{\circ}\text{C}$ , and because this temperature is permanent, electrical instruments need to be resistant to this temperature for a long time [52].

## 1.4 GOALS

The goal of this work is to make a pressure sensor that satisfies the requirements given in [Table 1.3](#). These requirements are given by the CHARM project, specified for a paper-milling company. The product for this project is a sensor platform. The sensor in this work is one of the sensors on this platform. By making this sensor modular and Back End Of Line compatible, the sensor can be integrated into the sensor platform.

Table 1.3: Sensor requirements for this work

Parameter	Requirement
Pressure range	80 Pa to 1 MPa
Temperature range	room temperature to $600^{\circ}\text{C}$
Substrate material	4H-SiC wafer
Process requirements	Modular design and Back End Of Line compatible

The sensor will be made in the [EKL](#). Even though the sensor can be sent to other cleanrooms for steps that are too complex for the [EKL](#), a goal for this work is to use steps that are all feasible in the [EKL](#). This way, the production of the sensor is accessible for more cleanrooms with similar equipment to this laboratory.

Like visible from [Table 1.2](#), not all SiC sensors have been tested at elevated temperatures. Even though some works mention that the sensor should theoretically be able to handle high temperatures, not all works actually tested this. A goal for this work is to test the sensor for the requirements given, including elevated temperatures.

## 1.5 THESIS OUTLINE

This work will review the design of a pressure sensor made from SiC. First, the design process will be discussed in [Chapter 2](#). In this chapter, theoretical models will be created for a circular non-touch capacitive pressure sensor in [Section 2.1](#). This model will be expanded for touching pressure sensors in [Section 2.2](#). Finally, the models will be verified with [Finite Element Modelling \(FEM\)](#) in the program COMSOL. This is discussed in [Section 2.3](#). Using these models, a final design decision will be made in [Section 2.5](#).

Once the design is defined, the process steps to make the design will be discussed in [Chapter 3](#). Firstly, a flowchart and the necessary steps are discussed in [Section 3.2](#). Finally, the steps taken in the cleanroom, including the challenges, are displayed in [Figure 3.4.2](#).

Now the devices are produced, the characterisation of the devices is the next step. The different setups used are discussed in [Chapter 4](#). Next, the devices are measured and verified in [Chapter 5](#).

Once the sensor has been characterised and the principle is verified, a conclusion will be given in [Chapter 6](#). Here, this project will be discussed, and suggestions for future work will be given.

## 2 | DESIGN

After defining the sensor type, the requirements and the limits, the design can be started. First, a mathematical model for a capacitive sensor will be set up. Afterwards, a simulation in COMSOL is created. This simulation is then verified with the mathematical model. Finally, design decisions will be made and the final design will be presented and simulated.

### 2.1 THEORETICAL APPROACH NON-TOUCHING MEMBRANE

To understand the behaviour of the capacitive sensor, a mathematical model can be created that approximates the nature of the device. This model can be split up into the deflection of the membrane due to the pressure and the change in capacity due to the changing distance between the terminals. Firstly, the deflection in the centre of the membrane will be characterized. Afterwards, the deflection at any point of the membrane will be evaluated. Finally, the corresponding capacitance will be calculated.

#### 2.1.1 Membrane center deflection

For this mathematical approximation, a simple capacitive pressure sensor design is used. An approximate design is visible in [Figure 2.1](#). Here, the substrate is cyan coloured, and a membrane covering a cavity is shown in orange. For illustrative purposes, the membrane is opened slightly. On top of the membrane, a contact is drawn in yellow, and inside of the cavity, another contact is present. If a pressure difference is present between the inside of the cavity and the outside of the sensor, the membrane will deflect. This deflection causes a difference in the average distance between the two contacts, altering their capacity.

Since the sensor in [Figure 2.1](#) has radial symmetry, the characteristics can be represented in a 2D model. The model corresponding to this illustrative design is shown in [Figure 2.2](#). In this model, the curvature is shown when a pressure difference is present. The membrane is deflected downwards, and thus, the electrodes are closer to each other.

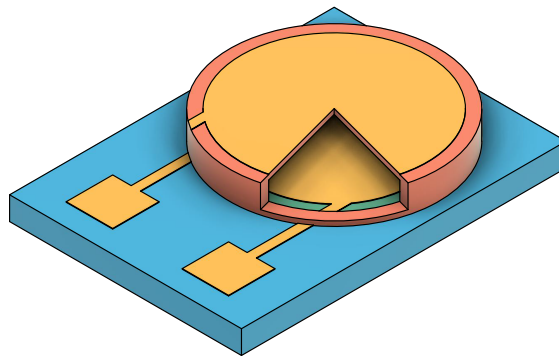


Figure 2.1: An illustrative design of a capacitive pressure sensor on a substrate

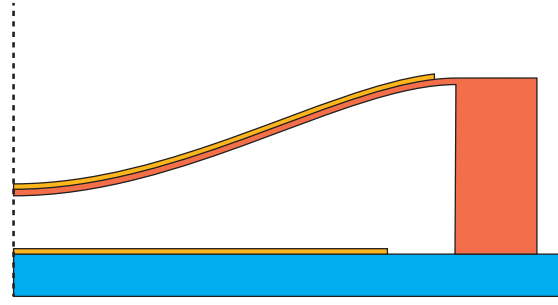


Figure 2.2: A 2D representation of Figure 2.1. The 3D representation can be reconstructed if this model is revolved around the dotted line. This representation is experiencing a pressure difference between the cavity and the environment

From this 2D representation, a mathematical model can be constructed. Since the electrode on top of the membrane will be an order of magnitude thinner than the thickness of the membrane, this part can be omitted from the calculations. In addition, because the sides of the sensor will be large compared to the thickness of the membrane, the sides can be seen as fixed columns. Therefore, the membrane can be approximated as a plate with clamped edges.

#### *Small deflection model*

Using the Kirchhoff-Love plate theory, the maximum deflection of a membrane is given with Equation 2.1 [34, 53].

$$w_0 = \frac{P \cdot R^4}{64D} \quad (2.1)$$

The maximum deflection of the membrane is at the centre. Therefore,  $w_0$  is in the middle of the membrane. In this equation,  $P$  is the applied pressure, and  $R$  is the radius of the diaphragm. In addition, this equation uses flexural rigidity, which is a material property defined with Equation 2.2 [34, 36, 54].

$$D = \frac{Eh^3}{12(1 - \nu^2)} \quad (2.2)$$

In this equation,  $E$  is the Young's modulus of the material,  $\nu$  is the Poisson's ratio, and  $h$  is the thickness of the diaphragm.

#### *Large deflection model*

The described model is viable for small deflections in relation to the membrane thickness. However, for this capacitive sensor, the deflection will likely be in the same order of magnitude as the thickness of the membrane. Therefore, Equation 2.1 can be expanded to Equation 2.3 to account for large deflections [34, 55].

$$w_0 = \frac{P \cdot R^4}{64D} \frac{1}{1 + 2\alpha \frac{w_0^2}{h^2}} \quad (2.3)$$

Here,  $\alpha$  is a term that is often set to 0.244, but a closer resemblance can be achieved using Equation 2.4 [34, 55]. Filling in this equation results in an  $\alpha$  of  $\alpha = 0.231$ .

$$\alpha = \frac{7505 + 4250\nu - 2791\nu^2}{35280} \quad (2.4)$$

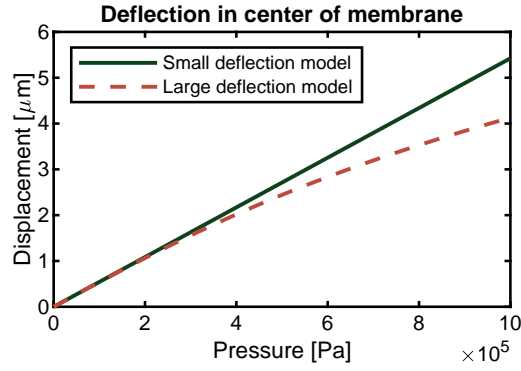


Figure 2.3: Mathematical models of the centre deflection of the membrane over the pressure.  $R = 200\mu m$ ,  $h = 5\mu m$

The difference of the two different models can be seen in Figure 2.3. The parameters used are the maximum membrane thickness of  $5\mu m$  that can be fabricated in the EKL environment without too much internal stress and a membrane radius of  $200\mu m$  [56]. Visible is that both models are very similar for low pressures. This is when the membrane is not deflecting a lot. At higher pressures, the difference becomes apparent. The small deflection model continues to deflect linearly, while the large deflection model decreases its slope with increasing pressures. This means that a gradually larger force is necessary to bend the membrane with the same amount.

### 2.1.2 General membrane deflection

Now the centre deflection is examined, the deflection at any given point of the membrane is of interest. As mentioned, because the membrane is circular, there is radial symmetry. Therefore, if the deflection at any point between the centre and the outer radius is known, the deflection of the whole membrane can be derived from this expression. Similar to the centre deflection, two models describe the deflection of any point of the membrane.

#### Thick membrane model

The most frequently used model is based on a thick membrane that behaves more like a plate [57]. However, when dealing with a thin membrane relative to the radius of the membrane, the model can be adjusted. The thick membrane model, however is based on Equation 2.5, where  $r$  is between 0 and  $R$  [34, 54, 55, 58].

$$w(r) = w_0 \left(1 - \frac{r^2}{R^2}\right)^2 \quad (2.5)$$

#### Thin membrane model

The thin membrane model is an extension of the previous model. It uses extra parameters that are derived from the thickness of the membrane. The model is shown in Equation 2.6 [57].

$$w(r) = \left[ w_0 + w_1 \left( \frac{r^2}{R^2} \right) + w_2 \left( \frac{r^4}{R^4} \right) \right] \left( 1 - \frac{r^2}{R^2} \right)^2 \quad (2.6)$$

In this equation,  $w_1$  and  $w_2$  are equal to:



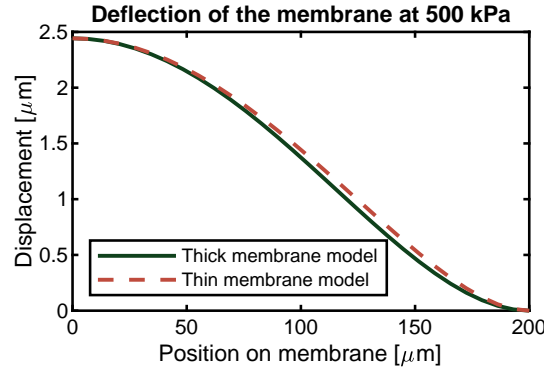


Figure 2.4: Mathematical models of the membrane deflection over the radius.  $P = 500\text{kPa}$ ,  $h = 5\mu\text{m}$

$$w_1 = \frac{0.0009}{\sqrt{h}} w_0$$

$$w_2 = \frac{0.001}{\sqrt{h}} w_0$$

The difference between the two models is visible in [Figure 2.4](#). In this figure, the deflection per position on the membrane is shown. The position at  $0\mu\text{m}$  is at the centre of the membrane, and the position at  $200\mu\text{m}$  is at the very edge of the membrane. The centre of the membrane is therefore deflected the largest amount, and the outer edge of the membrane is not deflected at all. If this figure is revolved around position  $0\mu\text{m}$ , the deflection of the whole membrane would be the result. The difference between the two models is that the thin membrane mode has a larger deflection halfway to the centre. This results in a larger average deflection compared to the thick membrane model.

### 2.1.3 Capacitance of membrane

Now the deflection of the membrane is known for every applied pressure, the capacitance can be calculated. The capacitance of two conductors is equal to the absolute permittivity of the dielectric separating the conductors multiplied by the area over the distance, displayed in [Equation 2.7](#)

$$C = \epsilon \frac{A}{d} \quad (2.7)$$

To approximate the capacitance of the membrane, a double integration can be performed to evaluate every point. The first integration is done to account for all values between the centre and the edge of the membrane, and the second integration revolves around the result around the centre of the membrane. The equation that evaluates the capacitance is shown in [Equation 2.8](#). Here  $g$  is equal to the total size of the gap. Subtracting the displacement from the total gap size will result in the distance between the two conductors at that point.

$$C = \int_0^{2\pi} \int_0^R \frac{\epsilon r}{g - w(r)} dr d\phi \quad (2.8)$$

This equation can be partly evaluated since there is radial symmetry. This is shown in [Equation 2.9](#)

$$C = 2\pi\epsilon \int_0^R \frac{r}{g - w(r)} dr \quad (2.9)$$

### capacitance with small deflection and thick membrane models

Now the expression for displacement can be filled in ( $w(r)$ ). The models for small deflection and a thick membrane will be inserted as a first approximation. This creates a more linear approximation to the real deflection. It will be valid for low pressures and small membrane radii. The large deflection and thin membrane will have to be substituted for a more realistic approach. However, due to the nonlinearity of the large deflection model and the added complexity of the thin membrane model, finding an analytical answer to the integration is not trivial.

Filling in the model for the thick membrane and rewriting Equation 2.9 will result in Equation 2.10.

$$C = \frac{2\pi\epsilon}{g} \int_0^R \frac{r}{1 - \frac{w_0}{g} \left(1 - \frac{r^2}{R^2}\right)^2} dr \quad (2.10)$$

When rewriting  $\frac{w_0}{g} \left(1 - \frac{r^2}{R^2}\right)^2$  to  $\left(\sqrt{\frac{w_0}{g}} - \sqrt{\frac{w_0}{g} \frac{r^2}{R^2}}\right)^2$ , this part can be substituted for  $x = \left(\sqrt{\frac{w_0}{g}} - \sqrt{\frac{w_0}{g} \frac{r^2}{R^2}}\right)$ . This means that  $dx = -2\sqrt{\frac{w_0}{g}} \frac{r}{R^2} dr$ . Finally, rewriting this for  $dr$  results in:  $dr = -\frac{R^2}{2\sqrt{\frac{w_0}{g}} r} dx$ . Now,  $x$  can be substituted, and  $dr$  can be rewritten in terms of  $dx$ . The result of this substitution is shown in Equation 2.11. Since the integration variable is changed from  $r$  to  $x$ , the integration limits will have to be rewritten in terms of  $x$  as well. Using  $x = \left(\sqrt{\frac{w_0}{g}} - \sqrt{\frac{w_0}{g} \frac{r^2}{R^2}}\right)$  and filling in the limits will result in new limits of  $r = 0 \rightarrow x = \frac{w_0}{g}$  and  $r = R \rightarrow x = 0$ .

$$C = -\frac{\pi\epsilon R^2}{g\sqrt{\frac{w_0}{g}}} \int_{\frac{w_0}{g}}^0 \frac{1}{1-x^2} dx \quad (2.11)$$

This integral can be solved, since  $\int \frac{1}{1-x^2} dx = \text{atanh}(x) + C$ . Therefore, the solution to Equation 2.11 is shown in Equation 2.12

$$C = \frac{\pi\epsilon R^2}{g} \cdot \frac{\text{atanh}\left(\sqrt{\frac{w_0}{g}}\right)}{\sqrt{\frac{w_0}{g}}} \quad (2.12)$$

Finally, the small deflection model can be filled in, resulting in an expression that is dependent on the pressure applied to the membrane. This expression is shown in Equation 2.13

$$C = \frac{\pi\epsilon R^2}{g} \cdot \frac{\text{atanh}\left(\sqrt{\frac{PR^4}{64Dg}}\right)}{\sqrt{\frac{PR^4}{64Dg}}} \quad (2.13)$$

### capacitance with large deflection and thin membrane

As already mentioned, using the large deflection and thin membrane models will result in an expression that is not trivial to evaluate. Luckily, Matlab can numerically integrate equations using:

$$q = \text{integral}(\text{function}, x_{\min}, x_{\max})$$

This means that although the model cannot be analyzed analytically, a result can still be gained numerically. The difference between the two models is shown in Figure 2.5. Since the small deflection model has an increased centre deflection compared to the large deflection model, a bigger nonlinearity is expected, emphasized

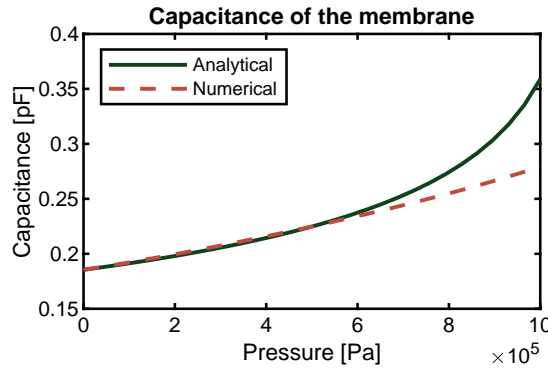


Figure 2.5: Capacitance of the membrane calculated analytically with the small deflection model and thick membrane model and calculated numerically with the large deflection and thin membrane models.  $R = 200\mu m$ ,  $h = 5\mu m$ ,  $g = 6\mu m$

at higher pressures. In addition, because the thick membrane model has a smaller average displacement, the capacitance is smaller than the thin membrane model. This effect is visible at low pressures.

## 2.2 MATHEMATICAL APPROXIMATION TOUCHING MEMBRANES

The previous section determined different models for calculating a non-touching membrane's capacitance. When the pressure increases, even more, the membrane will touch the bottom of the cavity. As shown in literature, this touch-point creates a linear response of the sensor[4, 28, 34, 36, 54, 55, 58–60]. Since a linear behaviour is desired, investigating in a touching membrane is performed.

To mathematically approach the behaviour of a touch-mode capacitive sensor, the model for a non-touch-mode sensor is expanded. Since the most accurate model is numerical, this model is used for calculating. That means that the result can only be gained from MATLAB compared to an analytical solution.

### 2.2.1 Dielectric layer

The first modification to the model is that a non-conducting layer should be added between the bottom electrode and the membrane. Now, when the membrane touches the bottom, there will not be a short between the membrane and the electrode.

The mathematical result for adding a layer is that the distance between the membrane and the bottom electrode is slightly larger than the gap size. This means that when the membrane is touching the bottom of the cavity, the distance between the conductors is not equal to  $0nm$ .

### 2.2.2 Membrane division

The mathematical model for the capacitance of the sensor does not stop when the membrane touches the bottom of the cavity. The centre displacement, shown in Equation 2.3, is only determined by the pressure and is not halted by maximum gap size. Therefore, once the pressure increases enough, the mathematical model states that the maximum deflection of the membrane is bigger than the gap size. A visual representation of this is shown in Figure 2.6

To extend the model so the result is valid when the membrane is pushed past its maximum, the membrane is split up into a part that is above and a part that is below the bottom of the cavity. The part that is above the membrane can be evaluated with

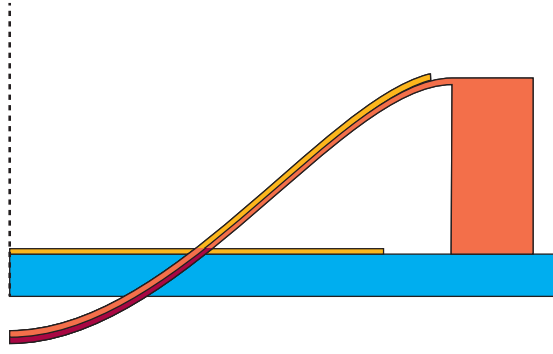


**Figure 2.6:** An illustrative design of a capacitive pressure sensor on a substrate when the membrane is pushed past its maximum. The darker colours show the part of the membrane past the limit

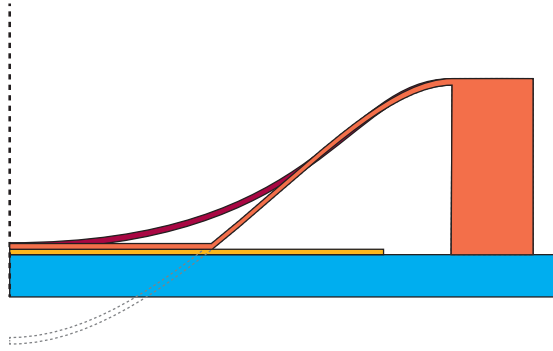


**Figure 2.7:** An illustrative design of the error this mathematical model makes compared to the real deformation of the membrane. The mathematical derivation is shown in orange and the real deformation is shown in red

the non-touching model. The part that is below the membrane is replaced with the membrane firmly pressed on the dielectric layer. This causes a slight error in the transition between the part that is above the membrane and pressed against the membrane. The difference between the reality and this calculation is visualised in [Figure 2.7](#).

To find the point where the membrane touches the bottom of the cavity, the equation for displacement should be rewritten. For the thick membrane model, the maximum displacement is equal to [Equation 2.5](#). The equation is repeated below:

$$w(r) = w_0 \left( 1 - \frac{r^2}{R^2} \right)^2$$

This equation can be rewritten in terms of  $r$ . The result is shown in [Equation 2.14](#). Since the displacement should equal the gap size,  $w$  can be substituted as  $g$ .

$$r(w) = R \sqrt{1 - \sqrt{\frac{w}{w_0}}} \quad (2.14)$$

To get a more realistic result, the thin membrane model should be used. However, this model results in an eighth-power polynomial. Therefore, the resulting radius can only be found numerically.

When solving the radius of the touching portion of the membrane for different pressures, the following result is gained, shown in [Figure 2.8](#)

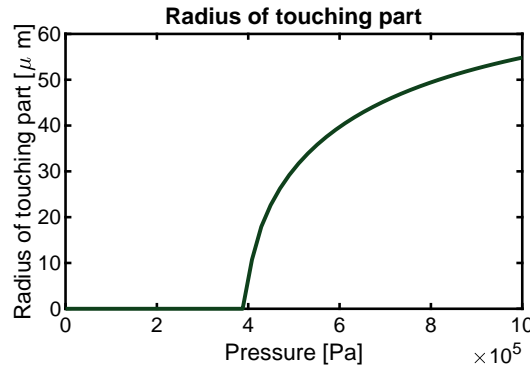


Figure 2.8: The numerically analysed radius of the touching portion of the membrane over a range of pressures.  $R = 200\mu m$ ,  $h = 5\mu m$ ,  $g = 2\mu m$

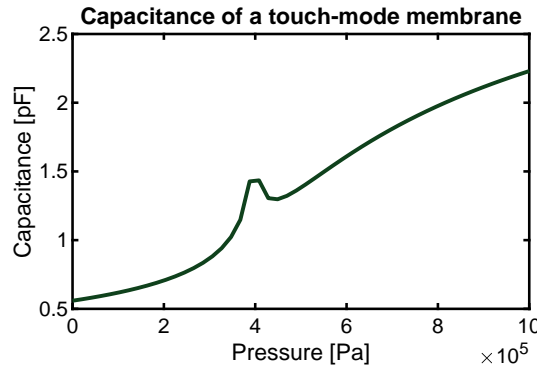


Figure 2.9: The capacitance of a touch-mode model made in Matlab.  $R = 200\mu m$ ,  $h = 5\mu m$ ,  $g = 2\mu m$

The radius of the touching part roughly follows a square root curve. This is approximated when the maximum deflection increases linearly with pressure. This happens at low pressures, as shown in Figure 2.3.

So for the total calculation of the capacitance, an addition of a circular capacitor with the same radius as the touching part and the previously calculated model from the point where the membrane touches until the edge of the membrane. The circular capacitor has a radius that is the same size as the radius of the touching part, and the thickness is the same as the dielectric. In addition, the permittivity is the same as the permittivity of the dielectric material between the membrane and the bottom electrode.

Once the two capacitor parts are added, a continuous model is created that can calculate the capacity even though the membrane is touching the bottom of the cavity. An example of the model is shown in Figure 2.9. The peak at around  $4 \times 10^5 Pa$  is caused by the transition between the two models. In reality, this peak does not exist, and in the simulation, this peak will not be visible either.

Visible in the figure is that the membrane touches at around  $4 \times 10^5 Pa$ , after which a linear region appears until  $8 \times 10^5 Pa$ . After this pressure, the sensor saturates.

The reason for this behaviour is that just after the point of contact, the radius of the touching part of the membrane increases linearly and is more significant to the non-touching part of the membrane. The linear area can be seen in Figure 2.8, just after  $4 \times 10^5 Pa$ , the radius of the touching part increases almost linearly. Since the capacitance is proportional to the radius of the capacitor, the total capacitance increases linearly as well.

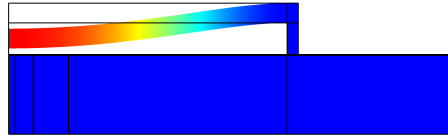


Figure 2.10: An example of the 2D circular model from COMSOL

After the initial linear increase of the touching part, the increase in radius saturates and eventually stops. This is directly reflected in the total capacitance of the device, causing a saturation region.

The advantage of the touching-mode sensors is that the sensitivity is significantly larger than the non-touching sensor. The disadvantages are that the membrane first has to touch before the linear region is created. In addition, the linear area is only limited until the touching radius does not increase linearly anymore.

## 2.3 COMSOL SIMULATIONS

Now that mathematical models have been created, mathematics can be validated by using software that simulates physics. In this case, COMSOL can simulate pressure on a membrane using FEM analysis. Even though this is no validation with the real world, the results of this analysis can be very realistic if the model is created appropriately.

### 2.3.1 Creating the model

First, the COMSOL model has to be created. The model used for quick but accurate results is a 2D model that is revolved around the centre of the membrane. As mentioned before, since the circular sensor is symmetric around the centre, a revolution can be done to discover the full characteristics. An example of the created model is shown in [Figure 2.10](#). The image shows the result of a simulation that applies pressure on the top membrane.

In addition to the 2D circular model, a 3D square model is created. This model can simulate what happens with sensors that have a square membrane. The simulation model is shown in [Figure 2.11](#)

#### *Geometry of the model*

The previously shown model is created with a union of different parts. [Figure 2.12](#) shows how the model is created. It consists of a series of rectangles with different properties attached to them. The substrate on the bottom consists of two rectangles next to each other. On top of that, two thin rectangles of [Silicon Nitride \( \$\text{Si}\_3\text{N}\_4\$ \)](#) are added as a dielectric layer. On top of that, a cavity rectangle is defined with the material properties of a vacuum. Next to this, a rectangle of [SiC](#) is placed that acts as a wall of the sensor. Finally, on top, a [SiC](#) rectangle is placed that acts as a membrane. The different rectangles are joined by creating a union. Finally, the union is formed into an assembly in COMSOL.

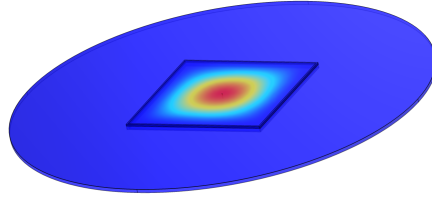


Figure 2.11: An example of 3D square model from COMSOL

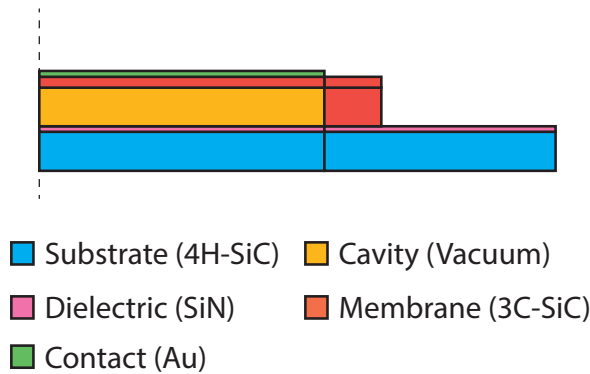


Figure 2.12: An illustration of the building blocks for the COMSOL simulation. The total model is based on a union between the blocks.

### Material properties

After the geometry is defined, the material properties need to be established. [Table 2.1](#) shows the used material properties for the simulation. Some properties are unnecessary for different materials based on their electrical or mechanical behaviour. Therefore, not all values are present in the table.

Table 2.1: Material properties used in the COMSOL simulations

Material	Young's Modulus	Poisson's ratio	Density	Relative permittivity	Coefficient of Thermal Expansion
<b>Substrate</b> 4H-SiC	$700 \times 10^9 [Pa]$ [61]	0.18 [61]	$3.20 [g/cm^3]$ [61]	-	$3.28 \times 10^6 [/^{\circ}C]$ [62]
<b>Dielectric</b> Si <sub>3</sub> N <sub>4</sub>	$200 \times 10^9 [Pa]$ [63]	0.25 [64]	$2.37 [g/cm^3]$ [64]	9.5 [64]	$3.26 \times 10^6 [/^{\circ}C]$ [62]
<b>Cavity</b> Vacuum	-	-	-	1	-
<b>Membrane</b> 3C-SiC	$430 \times 10^9 [Pa]$ [56]	0.168 [56]	$3.21 [g/cm^3]$ [56]	9.7 [56]	$14 \times 10^6 [/^{\circ}C]$ [65]

All materials are defined as solid except for the Cavity material. This has the property nonsolid.

### Applied physics

Now the different areas are defined, and each area is given material characteristics, the physical properties can be defined. Firstly, to make sure the cavity is freely movable, it is defined as a *deforming domain* in the *Moving Mesh* definition.

Then, for all domains except the cavity, *Solid Mechanics* physics can be applied. All domains are defined as a *Linear Elastic Material*. The substrate domains are held in place by applying a *Fixed Constraint*. Next, a *Boundary Load* is placed on the top of the membrane domain. The load type is set to *Pressure*. Sweeping this parameter will sweep the pressure applied on the membrane. Finally, since the model should also simulate the membrane touching the bottom of the cavity, a *Contact pair* is created between the bottom boundary of the membrane and the top boundary of the dielectric. To make sure the simulation converges, a minimum gap is placed between the two domains. The gap size is set to  $50\text{nm}$  and is applied in the *Offset from geometric destination surface*.

Next, *Electrostatics* physics is applied to the membrane, cavity and dielectric domains. A solid *Charge Conservation* is defined for the membrane and dielectric domains. A nonsolid *Charge Conservation* is selected for the cavity domain. A *Ground* is defined on the top boundary of the membrane, and a *Terminal* is applied on the bottom boundary of the dielectric. These terminals have a voltage of  $1\text{V}$  and effectively create the bottom electrodes.

### Physics study

With this information, COMSOL can determine how much the membrane deforms due to the applied load and what the capacity is due to the deformed membrane. To instruct COMSOL to calculate the deformation and capacitance, a *Study* has to be selected. Since the measurements of this sensor will be done in steady-state, a *Stationary* study is selected for this model. In this study, an *auxillary sweep* is enabled to sweep the parameter that expresses pressure. This sweeps the load placed on the top boundary of the membrane. Finally, this model can be computed and sensor designs can be extracted.

#### 2.3.2 Validating mathematical model with COMSOL simulations

Now the models are created correctly, the COMSOL models have to be validated with the mathematical models described previously. This can be done step-by-step, so each model is checked with the simulation.

##### Membrane center deflection

The first validation is the centre deflection of the membrane. The same parameters will be used for this validation as in [Section 2.1.1](#). The parameters are:

- Radius of the membrane =  $200\mu\text{m}$
- Thickness of the membrane =  $5\mu\text{m}$

Visible in [Figure 2.13](#) is that the previously derived model for large membrane deflections is accurate compared to the COMSOL physical model. With these parameters, the mathematical model has a deviation of 4% at  $1000\text{ kPa}$  compared to the COMSOL model. A conclusion is that the COMSOL model for deviation agrees with the mathematical model for membrane deflection.

##### General membrane deflection

Similarly, for the centre deflection, the model and simulation of the general deflection of the membrane can also be verified. Again, the same parameters will be used as in [Section 2.1.2](#). The parameters for the simulation will be:



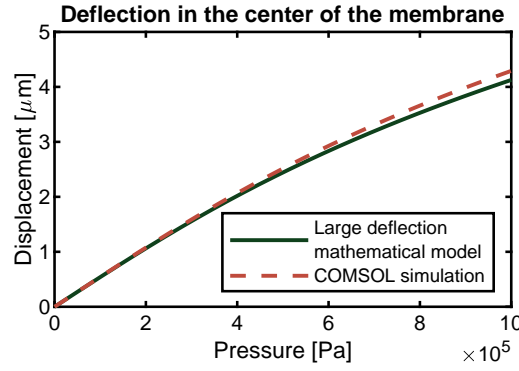


Figure 2.13: Comparison of the large deflection model and the COMSOL simulation.  $R = 200\mu m$ ,  $h = 5\mu m$

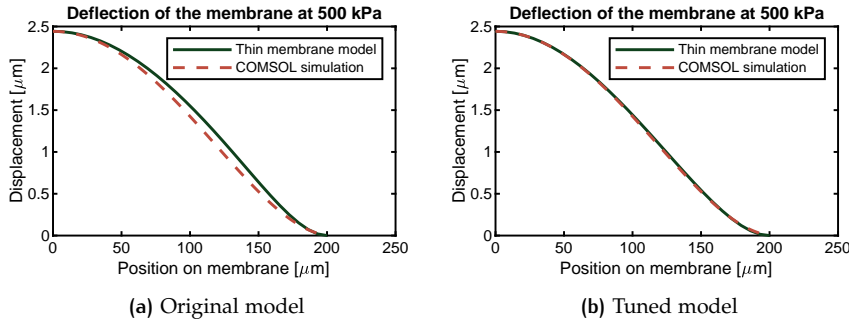


Figure 2.14: Comparison of the thick and thin membrane model and the COMSOL simulation.  $R = 200\mu m$ ,  $h = 5\mu m$

- Radius of the membrane =  $200\mu m$
- Thickness of the membrane =  $5\mu m$
- Pressure during simulation =  $500kPa$

Visible in Figure 2.14a is that the thin membrane model agrees with the COMSOL model for the most part. However, it does not precisely coincide with the simulation. To improve the result, it is possible to tune the thin membrane model by adjusting the parameters that make up  $w_1$  and  $w_2$  [57]. After tuning for different pressures, radii and other simulation parameters,  $w_1$  and  $w_2$  can be calculated as follows:

$$w_1 = \frac{0.0003}{\sqrt{h}} w_0$$

$$w_2 = \frac{0.0006}{\sqrt{h}} w_0$$

This decreases the maximum deflection error of the model compared to the simulation from 16% to 3%. The result is shown in Figure 2.14b

### Capacitance of the membrane

Finally, the capacitance of the COMSOL simulation can be determined. This is done by evaluating the *Maxwell Capacitance* between the corresponding bottom and top contact areas. The simulation has been carried out with the following parameters:

1. Radius of the membrane =  $200\mu m$
2. Thickness of the membrane =  $5\mu m$

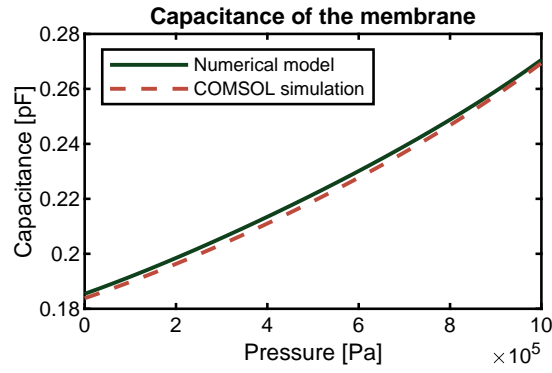


Figure 2.15: Comparison of the numerical model and the COMSOL simulation.  $R = 200\mu m$ ,  $h = 5\mu m$ ,  $g = 6\mu m$

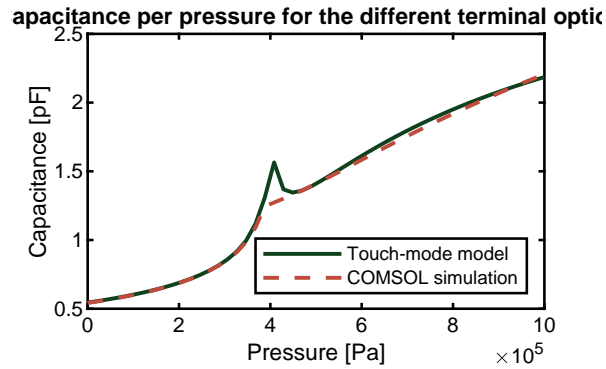


Figure 2.16: Comparison of the numerical model and the COMSOL simulation for touch-mode sensors.  $R = 200\mu m$ ,  $h = 5\mu m$ ,  $g = 2\mu m$

### 3. Height of cavity = $6\mu m$

The result of this simulation compared with the numerical model created in [Section 2.1.3](#) is shown in [Figure 2.15](#). Again, the simulation agrees with the model, meaning that the mathematical model can be used to find the best parameters for the design. Afterwards, COMSOL can be used to optimize and finetune the chosen parameters for a final design.

#### *Touch-Mode sensor*

Finally, the touch-mode sensor can be compared to the mathematical analysis. By decreasing the height of the cavity, the membrane will touch the bottom of the cavity in the specified pressure range. From the mathematical analysis, a linear region should appear after the membrane touches the bottom. This simulation is performed with the same parameters as the previous simulation, except for the height of the cavity. The height of the cavity now is  $2\mu m$ .

The result of this simulation is shown in [Figure 2.16](#). The mathematical model and the COMSOL simulation are similar for the most part. Only when the mathematical model moves from the non-touching calculation to the touching part, the mathematical model peaks more than the Matlab model. This could be due to the steps resolution of the simulation.

### 2.3.3 Temperature simulations

An advantage of having COMSOL models that represent the designs is that different simulations can be performed. These simulations can reveal conditions that can impact the behaviour of the design. In this case, effects due to temperature will

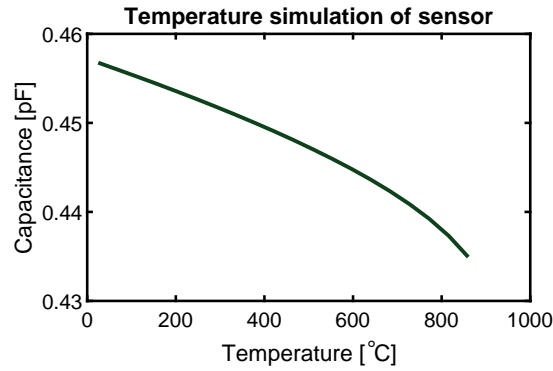


Figure 2.17: Temperature simulation of a sensor.  $R = 200\mu m$ ,  $h = 5\mu m$ ,  $g = 2\mu m$

also be verified using the simulation. The reason is that in addition to the pressure, this sensor should handle elevated temperatures. The expected behaviour is that the membrane will have a bigger displacement at high temperatures than it would be at room temperature. The reason for this behaviour is that the sensor materials experience thermal expansion.

### Simulation parameters

The model previously built can sweep different pressures, but it assumes a temperature of 25°C. To make the model simulate different temperatures, two new parameters are necessary. The first parameter is called  $T_{ref}$ . This is the temperature at which there are no internal stresses. This happens at the temperature at which the membrane is deposited. The deposition temperature of this membrane will be 860°C. This detail will be discussed in the process part of this report, in [Chapter 3](#). The second parameter is called  $T_0$ . This is the simulated temperature that will be swept during the simulation.

These parameters are added in to the *Linear Elastic Material* mechanic as a *Thermal Expansion* property.

The simulation results are shown in [Figure 2.17](#). Visible is that with a rising temperature, the capacitance value decreases. The reason is that at the reference temperature of 850°C, the membrane has no thermal stresses. When the temperature decreases, the membrane starts to experience stresses due to the difference between thermal expansion of the layer stack. The reaction from the membrane is that it moves down towards the bottom contact.

## 2.4 CREATING DESIGNS

Now the MATLAB and COMSOL models are very similar in result, the two models can be used to predict the final characteristics of the sensor. With the information, sensor designs can be created that abide by the requirements.

### 2.4.1 Design extremes

Unfortunately, the designs have some limitations in terms of physical feasibility. To make sure that the devices can be constructed and that their behaviour is as expected. Because multiple membrane-based sensors have been constructed in the [EKL](#), some design limitations can be established [17].

### Membrane radius

Based on earlier experiments in the [EKL](#), the radius of a clamped membrane should be limited to a maximum of  $500\mu m$ . Anything lower than this value is producible.

### Membrane thickness

The membrane thickness is limited by the thickness of [SiC](#) that can be deposited with [LPCVD](#). In the [EKL](#), the maximum thickness is  $5\mu m$ , as discovered in previous devices [\[17, 56\]](#).

### Gap height

The gap height is determined by the height of the sacrificial layer. From discussions with the staff of [EKL](#), the preferred height is a maximum of  $10\mu m$ , but a gap height of  $15\mu m$  might work.

### Design extreme conclusion

After determining the maximum design parameters, the sensor can be built anywhere within these parameter limits. A summarising table is shown in [Table 2.2](#)

Table 2.2: Maximum design parameters for the sensor

Parameter	Requirement
Membrane radius	Maximum of $500\mu m$
Membrane thickness	Maximum of $5\mu m$
Gap height	Preferred maximum of $10\mu m$ , absolute maximum of $15\mu m$

Now the design extremes are properly defined, the design can be evaluated. Looking back at the mathematical model and COMSOL simulations that were previously defined, the design parameters are within the limits imposed by the design extremes. [Figure 2.15](#) shows the response of this design. At  $0Pa$ , the capacitance is about  $0.18pF$ . At  $1000kPa$ , the capacitance is about  $0.27pF$ . While the response is relatively linear, the device's sensitivity is not very high. In the total range, the sensitivity of the device will be  $0.009fF/100Pa$ . Therefore, one of the improvements that will have to be made is sensitivity.

#### 2.4.2 Sensitivity analysis

To understand how to improve the sensitivity effectively, the mathematical model can be used. Since the analytical model is set up and valid for at least a low pressure and a small membrane, a sensitivity analysis can be performed with it. Ideally, there is a big capacitance change over the pressure range. The bigger the capacitance change, the more sensitive the sensor is, and small deviations of the pressure can be read out.

The sensitivity of the models can be found by taking the derivative of the capacitance with respect to the pressure:  $S = \frac{\partial C}{\partial P}$  [\[53\]](#). The result of taking this derivative is shown in [Equation 2.15](#)

$$S = \frac{\partial C}{\partial P} = \frac{\pi \epsilon R^2}{g} \frac{1}{2P} \left( \frac{1}{1 - \frac{PR^4}{64Dg}} - \frac{\operatorname{atanh}\left(\sqrt{\frac{PR^4}{64Dg}}\right)}{\sqrt{\frac{PR^4}{64Dg}}} \right) \quad (2.15)$$

This equation can be displayed in a figure, this is done in [Figure 2.18](#). Visible from this function is that there is a base sensitivity regardless of the pressure since,

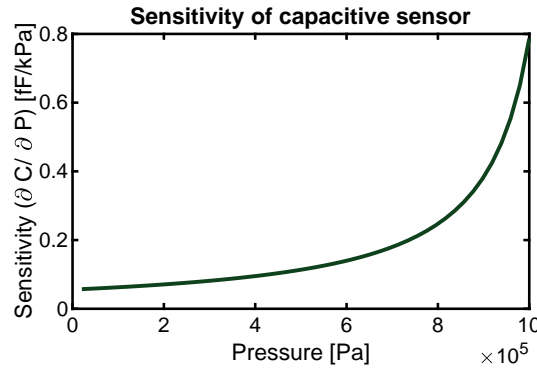


Figure 2.18: Sensitivity function of the sensor using the small-deflection and thick-membrane models.  $R = 200\mu m$ ,  $h = 5\mu m$ ,  $g = 6\mu m$

at  $P = 0$ , the sensitivity is not equal to 0. In addition, when the pressure increases, the sensitivity will reach an asymptote. This happens when the deflection of the membrane is the same as the gap size, so in Equation 2.12, when  $w_0 = g$ , then  $\text{atanh}(1) = \infty$  causes an infinitely high capacitance and sensitivity. In terms of pressure, if the pressure equals  $P = \frac{64Dg}{R^4}$ , then the centre of the membrane will touch.

To get a base sensitivity, this equation can be evaluated at  $P = 0$ . This way, the sensitivity is only based on the physical parameters of the device. When this relation is evaluated at  $P = 0$ , the sensitivity in Equation 2.16 is gained.

$$S|_{P=0} = \frac{\pi\epsilon R^2}{g} \frac{R^4}{3 \cdot 64Dg} = \frac{\pi\epsilon R^6(1-\nu^2)}{16g^2Eh^3} \quad (2.16)$$

From this equation, there are some design parameters that the sensitivity is proportional to, shown in Equation 2.17 [53]. This means that the general sensitivity of the sensor increases with a power of six when the radius is increased, or the sensitivity increases with a power of two when the gap size is decreased.

$$S \propto \frac{R^6}{g^2h^3} \quad (2.17)$$

To conclude, a sensor with a large, thin membrane and a small gap size will maximize the sensitivity.

This conclusion is valid for both the non-touching and touching models since a higher sensitivity at  $0Pa$  will result in a higher overall sensitivity. Therefore, both the touching and non-touching sensors can benefit from these design parameters.

### Design divisions

Using the information from the maximum design parameters and the sensitivity analysis, the sensor can be optimized for sensitivity. Creating a non-touching sensor for the whole pressure range will have to be compromised in radius. When the maximum thickness and gap size are used, the membrane is the most rigid and it takes the longest time to reach the bottom of the gap. Even when using these parameters, a membrane with a radius of  $500\mu m$  will touch the bottom of the gap before the maximum pressure is reached. The only method of creating a non-touching sensor over the whole range is to decrease the radius of the sensor. When using a maximum membrane thickness of  $5\mu m$  and the maximum cavity height of  $14\mu m$ , the maximum membrane radius before touching occurs is  $370\mu m$ . A sensor with these properties will behave as shown in Figure 2.19.

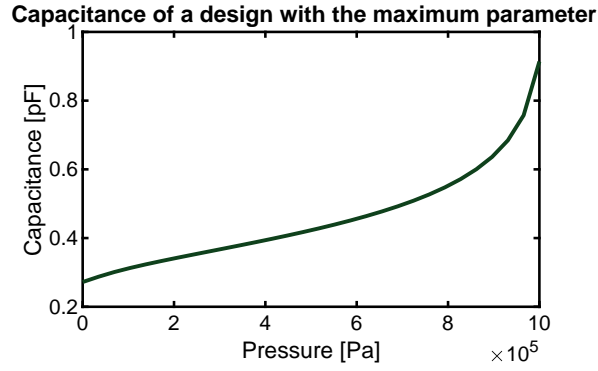


Figure 2.19: Capacitance of a model that has the maximum design parameters.  $R = 370\mu\text{m}$ ,  $h = 5\mu\text{m}$ ,  $g = 14\mu\text{m}$

Compared to the previous designs, the sensitivity is larger. The full range of this sensor moves from  $0.25\text{pF}$  at  $0\text{Pa}$  to  $0.91\text{pF}$  at  $1000\text{kPa}$ . This gives a sensitivity of  $0.066\text{fF}/100\text{Pa}$ . This is an improvement of more than a factor of 10. However, a higher sensitivity is preferred.

If a touch-mode design is used for the full range, the membrane has to touch the bottom of the cavity at pressures below  $80\text{Pa}$ , while being stiff enough to cause a linear touching radius until at least  $1000\text{kPa}$ . Based on the results of the models, this is not feasible.

Since neither design fully works over the whole range, a solution can be constructed by combining different sensors for different pressure ranges.

The pressure range is divided into three parts: a low-pressure part, a mid-pressure part and a high-pressure part. Now, the sensors can be designed specifically for the smaller pressure range. This increases the total sensitivity of the range significantly.

The low-pressure and mid-pressure ranges will be measured by a non-touching sensor, while the high-pressure range will be measured by a touching sensor.

#### 2.4.3 Increasing linearity non-touching membranes

Since a decision has been made on how to divide the sensor into three parts with specific pressure ranges, it is known that the non-touching sensor will be used. Like mentioned, the division of the sensor into specific ranges increases the sensitivity significantly. However, increasing the sensor's sensitivity is only one aspect of improving the quality of the sensor. Another aspect, which is very important for this type of sensor is linearity. As mentioned in [Section 1.3](#) and visible in [Figure 2.5](#) and [Figure 2.19](#), the output of this type of sensor is intrinsically nonlinear. The reason is that for large pressures, the maximum displacement is not linear, seen in the large deflection model of [Figure 2.3](#). In addition, the total capacitance is governed by the distance of the deformed membrane compared to the bottom of the sensor. As the pressure increases, the membrane deforms, which results in a nonlinear overall displacement of the membrane. This is especially pronounced when the membrane gets close to the bottom of the cavity. Since the distance is very small, the capacitance change is high.

While the centre of the membrane causes the biggest displacement and thus the biggest capacitance change, it also is the source of the largest part of the nonlinearity. If the membrane were divided into two parts, the middle part would contribute the most of the capacitance change and be the most nonlinear. This can be seen in [Figure 2.20](#). In this figure, the membrane has been divided into an inner ring and an outer ring. The radius of the inner ring is  $\sqrt{\frac{1}{2}}$  times the outside radius. This ratio ensures that the inner and outer ring areas are the same size. The result is that both rings contribute the same capacitance at  $P_0 = 0[\text{Pa}]$ .

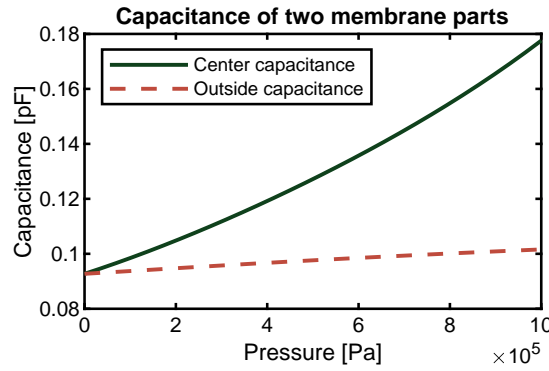


Figure 2.20: Capacitance per pressure of two membrane parts, a centre part and an outside ring.  $R = 200\mu m$ ,  $h = 5\mu m$ ,  $g = 6\mu m$

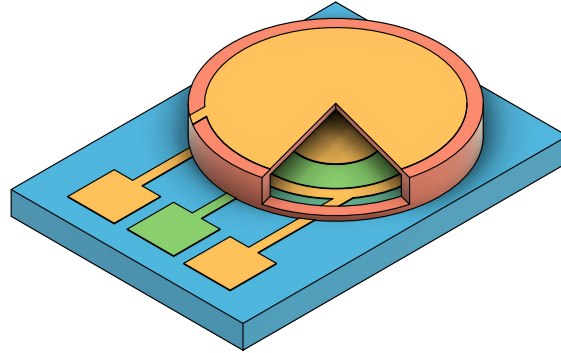


Figure 2.21: An illustrative design showing isolated contacts at the bottom of the sensor, displayed in yellow (inner electrode) and green (outer electrode)

However, at higher pressures, the capacitance increase of the inner part is significantly higher than the outside ring. Also visible in the figure is that the inside part is less linear than the outer ring. In this example, the maximum linearity error of the inside is equal to 3.3%, while the maximum linearity error of the outside ring is equal to 0.3%.

Since the centre of the sensor causes the biggest nonlinearity, it can be used to compensate for the rest of the nonlinear behaviour. This can be done by dividing up the bottom electrode. Then, part of the bottom electrode can be used as reference capacitance, which is subtracted from the measured capacitance. The division will be made concentrically like illustrated in [Figure 2.21](#)

As shown in the previous sections is that the most precise manner of calculating the capacitance of the sensor is done numerically with the help of MATLAB. To minimise the linearity error, the same numerical models will be used. To find an optimum in linearity, the following MATLAB function has been used:

$$q = \text{fmincon}(\text{fun}, x_0, A, b)$$

This function is able to find a minimum of a constrained nonlinear function. By using  $x_0$  as the ratio between the bottom contacts,  $\text{fun}$  returns the linearity for the specific configuration. The function then searches for the minimum over all possible bottom contact configurations.

By adding different amounts of concentric bottom contacts, MATLAB can find the optimum for each situation. By using a baseline of one bottom contact, the increase of linearity can be visualised. The result of the optimum division is shown in [Figure 2.22](#).

Visible is that for a higher amount of electrodes, the linearity is increasing. Using two electrodes has little effect, using three is a lot more linear, four electrodes are a little more linear and five more as well. Unfortunately, there is a trade-off. By

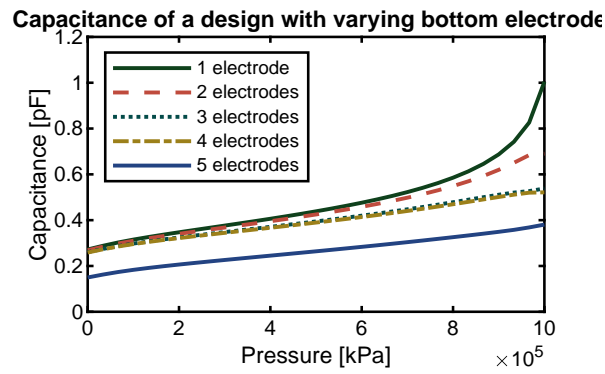


Figure 2.22: The result of Matlab optimization

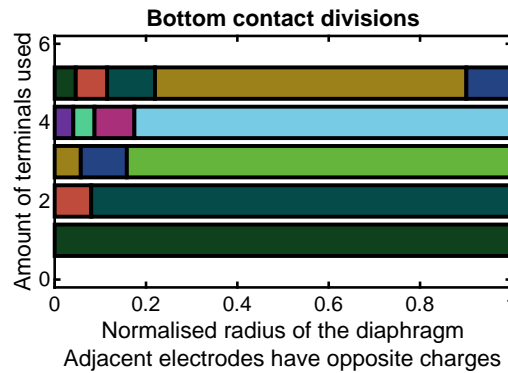


Figure 2.23: Optimum division of bottom electrodes. Neighbouring electrodes have opposite capacitances

increasing the linearity, the sensitivity of the sensor decreases. Even the difference between three and four electrodes decreases the sensitivity slightly. Therefore, the results of up to five electrodes have been analysed. Adding more electrodes will result in too much loss of sensitivity.

The optimum division of the electrode is shown in Figure 2.23. Each electrode adds or subtracts from the total capacitance and next to a 'positive capacitance' electrode will be a 'negative capacitance' electrode. Visible from this figure is that most changes are close to the middle of the membrane. The reason is that the centre of the membrane causes the most nonlinearity.

When optimized using MATLAB, a very linear result can be achieved with reasonably high sensitivity. For a different amount of electrodes on the bottom, a different optimum can be found. Experimentally, it is found that this optimum is valid in most cases even when changing the gap size, membrane thickness or membrane radius.

The optimum values found are listed in Table 2.3

Table 2.3: Optimum normalised division of bottom electrodes

Amount of bottom contacts	Area contact 1	Area contact 2	Area contact 3	Area contact 4	Area contact 5
1	1	-	-	-	-
2	0.08	0.92	-	-	-
3	0.10	0.15	0.75	-	-
4	0.08	0.07	0.12	0.73	-
5	0.08	0.08	0.12	0.57	0.15



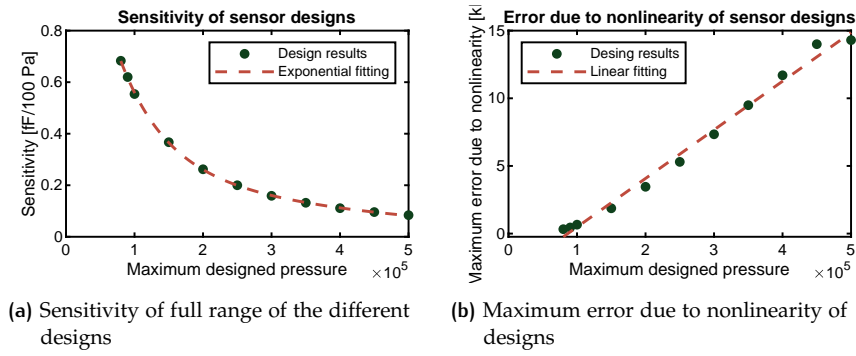


Figure 2.24: Results from different designs that measure from  $80\text{ Pa}$  up to a specified pressure

#### 2.4.4 Design decision

The previous subsections displayed techniques to increase sensitivity and decrease nonlinearity. These techniques can be applied to find how sensors with different parameters behave. Using this data, a decision can be made to find at which pressure range the low, mid and high-range sensors will operate. In addition, the exact parameters of the final designs will be created. Since the low and mid-range sensors will be based on a non-touch membrane, the parameters have to be tuned to the maximum pressure these designs will have to measure. This is because the membrane cannot touch at the maximum pressure, but it should be very close to touching.

Using the mathematical model, multiple sensor designs have been simulated. Each sensor has a different maximum pressure that it has to reach. The design parameters are adjusted for each new simulation. Each simulation has a membrane that is as big as possible, but with a maximum radius of  $500\mu\text{m}$ . On top of that, the gap size or the membrane thickness is adjusted so the membrane almost touches at maximum pressure.

The results for sensitivity and maximum readout error can be seen in Figure 2.24. Visible is that for a higher maximum designed pressure, the sensitivity decreases exponentially and the readout error increases linearly. The results in this image have been generated using three bottom contacts.

The simulated results all have a range from  $80\text{ Pa}$  up to the respective maximum pressure. This means that the figures are valid for the low-pressure sensor that starts at  $80\text{ Pa}$ . The mid-range sensor will be based on a non-touch sensor as well. This means that Figure 2.24a still applies to the sensor design. Figure 2.24b does not apply anymore, since the sensors typically experience some nonlinearity at the lower pressure range. The mid-range sensor is not sensitive to this part of the pressure range. Therefore the error of this sensor will be smaller than displayed in the figure.

The high-pressure sensor will be a touch-mode design. Since the sensitivity of this type of sensor is an order of magnitude higher than for non-touch sensors, the sensitivity is a smaller concern. The requirement for this sensor is that it is tuned to have a linear range over the whole high-pressure range. From simulation results, designs that measure from  $280\text{ kPa}$  and higher can be created to have a linear response up to  $1000\text{ kPa}$ .

Since this gives a clear beginning point for the high-pressure sensor, the division between mid-range and high-range pressure sensors can be decided. The division is, therefore, placed at  $300\text{ kPa}$ . To make sure that the low range is sensitive enough for the small changes, while also being linear enough, the division is placed at  $100\text{ kPa}$ .

## 2.5 CHOSEN DESIGNS

As mentioned before, the sensor will be split up into three parts. After evaluation of the models and verification with COMSOL, a division has been made that balances between sensitivity and linearity. Now, the design parameters have to be constructed so the sensors have the correct behaviour in their corresponding pressure range.

Because the sensors will have to be fabricated on a wafer, some decisions have to be made in favour of fabrication. Using masks for fabrication makes it straightforward to alter designs in a planar direction while altering specific designs in an out-of-plane direction on the same substrate is a challenge. This will require extra processing steps and masks.

For that reason, it has been decided that the membrane thickness of all designs will be  $5\mu\text{m}$ . This facilitates a process with fewer steps. In addition, the designs for high-pressure and low-pressure can have the same gap height with minimal concessions.

Parameters that come with these designs are shown in [Table 2.4](#).

Table 2.4: Chosen parameters for the design

Design	Radius [ $\mu\text{m}$ ]	Membrane thickness [ $\mu\text{m}$ ]	Gap height [ $\mu\text{m}$ ]
Low-range sensor	470	5	8.5
Mid-range sensor	470	5	14
High-range sensor	400	5	8.5

The designs have been simulated in COMSOL using these parameters. The amount of bottom contacts for the low-and mid-range sensors used for this simulation is 3. The reason is to get the highest expected sensitivity from the simulations. [Table 2.5](#) displays the expected performance of the chosen designs based on the simulations done.

Table 2.5: Expected performance of chosen designs

Design	Minimum pressure [Pa]	Maximum pressure [Pa]	Sensitivity [fF/100 Pa]	Max linearity error [kPa]
Low-range sensor	80	101,000	0.30	0.663
Mid-range sensor	100,000	301,000	0.13	1.667
High-range sensor	300,000	1,000,000	5.03	79.930

To make sure that variations in the process or possible errors in calculation will alter the result, a range of designs will be created. The range of the designs that will be made are as follows:

Radius:  $250 - 500\mu\text{m}$  with increments of  $50\mu\text{m}$

Membrane thickness  $5\mu\text{m}$  (can still be changed during the fabrication)

Gap height:  $7\mu\text{m}, 8.5\mu\text{m}, 10\mu\text{m}, 14\mu\text{m}$

[Figure 2.25](#) shows the simulated response from the low-range pressure sensor. [Figure 2.26](#) shows the simulated response from the mid-range pressure sensor and [Figure 2.27](#) shows the simulated response from the high-range pressure sensor.

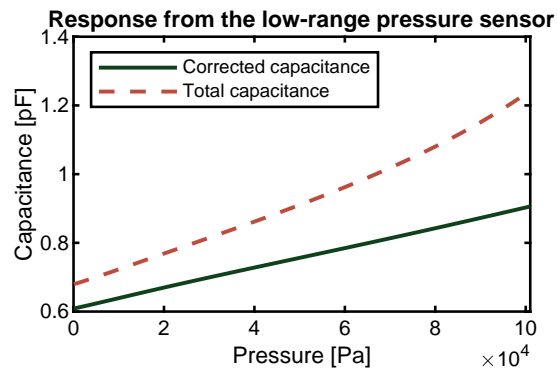


Figure 2.25: Simulated response of the low-pressure sensor design

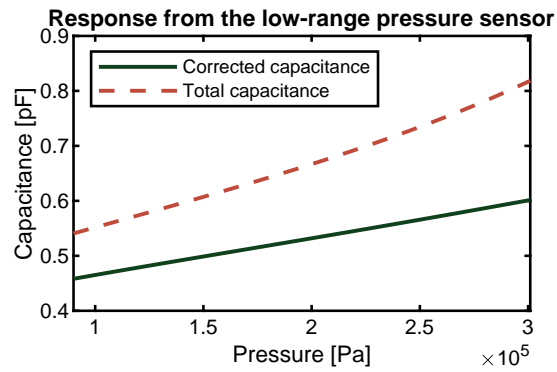


Figure 2.26: Simulated response of the mid-range pressure sensor

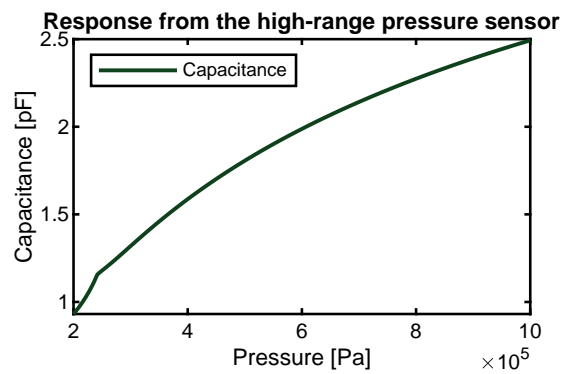


Figure 2.27: Simulated response of the high-range pressure sensor

## 2.6 MASK DESIGN

The theoretical design has been completed in the previous sections. The next part of the design is to convert the simulated layers into a fabricable design by making masks for each layer. Using these masks, the designs created for the sensors can be transferred to the wafer directly. When this design has been transferred, selected areas can be etched or deposited. A mask is, in fact, a transparent material, quartz in this case, and it has opaque areas. When shining a light through this mask, the design can be transferred to a light-sensitive material, photoresist. An example of a mask that is used for this sensor is shown in [Figure 2.28](#). The masks used for this project are on a 1-to-1 scale.

This section focuses on the different masks that are used. However, first, the general mask alignment will be discussed. After that, the key fabrication layers will be defined. A mask is necessary for each of these layers to shape the material as intended. Finally, the mask design will be discussed for each different mask.

Because there is a range of values for each design parameter that will be created, there will be many designs. To divide the designs logically, the decision has been made to place the four different contact arrangements on one die. Therefore, one die will contain a design with one, three, four, and five contacts. The rest of the design inside the die will be the same.

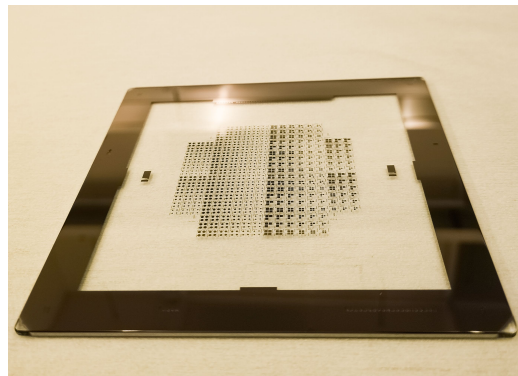


Figure 2.28: A photo of one of the masks used for processing

### 2.6.1 Mask alignment

To create the pressure sensor, multiple masks are necessary. These masks all have to be placed with the same orientation and position to make sure the designs of each layer align. To make sure that the wafer is oriented and positioned correctly when transferring the masks, special alignment markers have been designed. Two alignment markers are placed on the substrate before the processing begins. The first marker is designed by ASML. It is a cross pattern that uses light interference to determine the position and rotation [66]. The design of this mask is shown in [Figure 2.29a](#). The marker size is  $610\mu m$  by  $610\mu m$ . The second alignment marker is a standard marker used in [EKL](#). This ensures that the masks are aligned relative to the alignment marker, even for manual alignment. A part of this marker is shown in [Figure 2.29b](#). The black part of this design is etched before the process starts. Using the different crosses, the new masks can be aligned. In [Figure 2.29b](#), the first mask is placed in blue on top of the black marker. It is visible that the cross fits tightly in the blue design. The next masks will be aligned with the other black crosses. In addition, a mask can be aligned with a previous mask if one of the blue crosses is used.

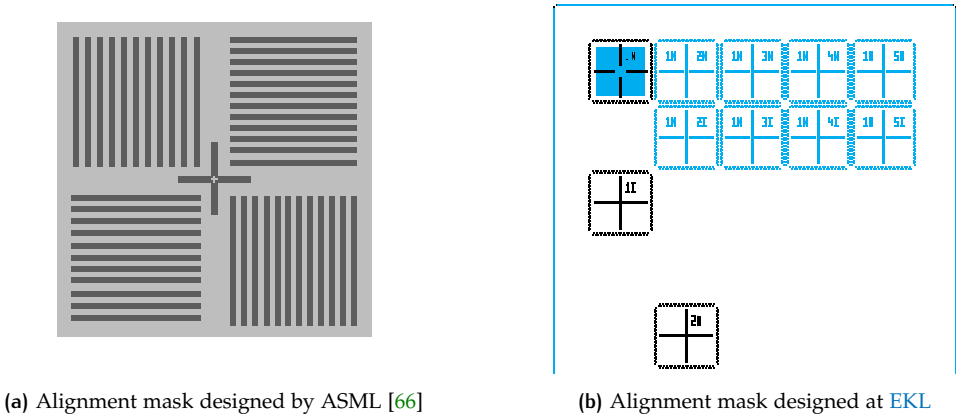


Figure 2.29: The two different alignment marker designs used on the wafer

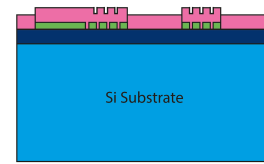
2.6.2 Fabrication layers

The COMSOL and mathematical models are based on ideal physical properties for a pressure sensor. These ideal models should now be converted to a design that can be fabricated. In the cleanroom environment, it is helpful to think of designs in terms of the different layers that must be applied, shaped, or removed. More details about the specific steps are discussed in Section 3.2. The key fabrication layers are explained in Table 2.6.

Table 2.6: Key fabrication layers for the sensor

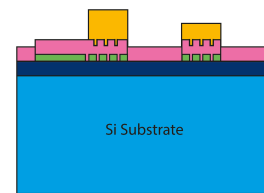
Fabrication layer	Visual impression of the layer
After receiving the wafer, the first step is adding a passivation layer. This passivation layer will protect the previously created structures in the substrate. On top of that, the contacts that will be constructed for the sensor will be isolated from doped regions on the substrate.	The image shows a cross-section of the wafer. The bottom layer is a blue rectangle labeled 'Si Substrate'. Above it is a thin, dark blue layer labeled 'a-SiC passivation'. A legend below the image shows a blue square for 'Si Substrate' and a dark blue square for 'a-SiC passivation'.
The second layer will define the bottom contacts of the structure. Because metals are often considered contaminating for the substrate and machines, a green metal will be used. The green metal will be Molybdenum for its high melting point. For this step, Mask 1 is necessary.	The image shows a cross-section of the wafer. The bottom layer is a blue rectangle labeled 'Si Substrate'. Above it is a thin, dark blue layer labeled 'a-SiC passivation'. On top of the passivation layer are several small, green rectangles labeled 'Molybdenum'. A legend below the image shows a blue square for 'Si Substrate', a dark blue square for 'a-SiC passivation', and a green square for 'Molybdenum'.

After the metal layer is deposited, another layer is created that will act as a dielectric material between the membrane and contact layer. If the membrane touches the bottom of the cavity, the dielectric layer ensures that there will be no short circuit and still a capacitance between the membrane and contacts. This layer will be patterned using **Mask 2**. The pattern that is placed will create small holes in the layer to prevent layer stiction if the membrane is pressed on the dielectric layer.



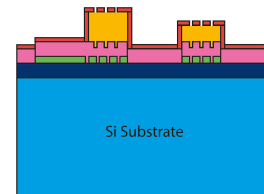
- |              |                      |
|--------------|----------------------|
| Si Substrate | a-SiC passivation    |
| Molybdenum   | PECVD SiN dielectric |

Next, a sacrificial layer is created from Silicon Oxide. This layer has a difference in height depending on the range of the sensor (high, mid or low pressure). To create this layer, **Mask 3** and **Mask 4** are used. As the name implies, this layer will be removed after the membrane is formed around it.



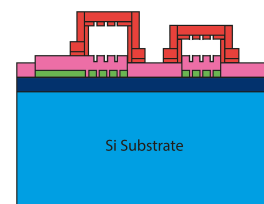
- |                        |                      |
|------------------------|----------------------|
| Si Substrate           | a-SiC passivation    |
| Molybdenum             | PECVD SiN dielectric |
| Sacrificial layer SiO2 |                      |

On top of the Silicon Oxide, a layer of Silicon Carbide is placed. This is the same material as the membrane will be formed from. Initially, only a thin membrane is deposited. **Mask 2** is now reused to create small holes through the membrane. These holes will be used to release the sacrificial layer and create the cavity.

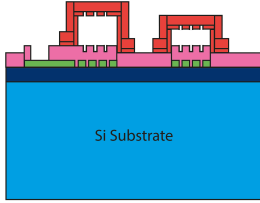
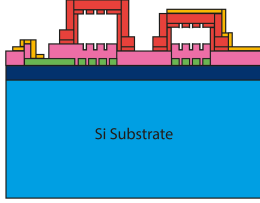


- |                        |                      |
|------------------------|----------------------|
| Si Substrate           | a-SiC passivation    |
| Molybdenum             | PECVD SiN dielectric |
| Sacrificial layer SiO2 | Poly-SiC             |

Next, the sacrificial structure is released by using vapour HF etching. Once the sacrificial material is removed, a thick layer of SiC is deposited on top of the thin membrane, completing the total membrane thickness. This SiC layer is then trimmed to the correct size using **Mask 5**.



- |              |                      |
|--------------|----------------------|
| Si Substrate | a-SiC passivation    |
| Molybdenum   | PECVD SiN dielectric |
| Poly-SiC     |                      |

<p>After the membrane has been formed, the bottom contact can be opened up. <b>Mask 6</b> is used to open up vias to the bottom metal contact.</p>	 <div data-bbox="810 459 1129 562"> <div> <div>Si Substrate</div> <div>Molybdenum</div> <div>Poly-SiC</div> </div> <div> <div>a-SiC passivation</div> <div>PECVD SiN dielectric</div> </div> </div>
<p>Finally, the top contact will be created along with pads to connect to the sensor externally. The overlay metal is created using the lift-off technique with the help of <b>Mask 7</b>.</p>	 <div data-bbox="810 896 1129 999"> <div> <div>Si Substrate</div> <div>Molybdenum</div> <div>Poly-SiC</div> </div> <div> <div>a-SiC passivation</div> <div>PECVD SiN dielectric</div> <div>Cr/Au - 10nm/200nm Overlay</div> </div> </div>

As mentioned in the table, a total of seven masks are necessary to produce the pressure sensor. Each mask is used once on a specific layer, except mask 2, which is used twice

### 2.6.3 Mask 1 - Bottom contact patterns

The first mask that will be used is to create patterns in the bottom contact material. In addition, pads will be created to connect to the bottom contacts. As discussed in [Section 2.5](#), there are a few designs that will be placed on the final design. The following parameters bring a change in the design of the bottom mask:

1. Membrane radius
2. Amount of contacts
3. Contact arrangements
4. Shape of the membrane

As mentioned, each die will consist of four sensors. The design parameters for the sensors on one die will be the same except for the number of contacts. In addition to the designs discussed in [Section 2.5](#), square membranes will also be added. Square membranes behave similarly to circular membranes, but these designs have a higher displacement at the same pressure compared to circular designs of the same size. Therefore, these sensors are more sensitive but have a smaller pressure range they can operate in [53, 59]. The widths of the squares in this design are the same as the diameters of the circular designs. Therefore, the range of widths that will be designed is from  $500\mu m$  to  $1000\mu m$ . [Section 2.4.3](#) discusses the optimal contact arrangement for the size. While the reached values theoretically would result in the most linear characteristic, variations during production could lead to nonidealities.

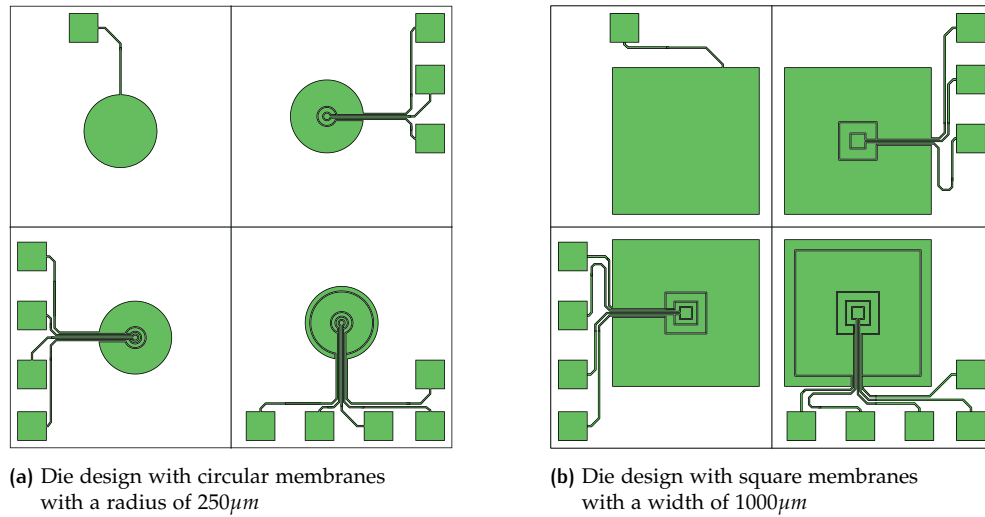


Figure 2.30: Two different die designs for Mask 1

Therefore, two extra arrangements are made. In total, three different arrangements will be produced. The division for each arrangement is shown in Table 2.7

Table 2.7: Designed contact arrangements of bottom electrodes

Contact arrangement	Area contact 1	Area contact 2	Area contact 3	Area contact 4	Area contact 5
1	1	-	-	-	-
3.1	0.10	0.15	0.75	-	-
3.2	0.08	0.13	0.79	-	-
3.3	0.12	0.14	0.74	-	-
4.1	0.08	0.07	0.12	0.73	-
4.2	0.05	0.08	0.13	0.74	-
4.3	0.10	0.11	0.11	0.68	-
5.1	0.08	0.08	0.12	0.57	0.15
5.2	0.06	0.08	0.13	0.60	0.13
5.3	0.1	0.09	0.10	0.48	0.23

In Figure 2.30, two different dies are shown. In Figure 2.30a, the smallest circular design is visible. On the other hand, Figure 2.30b shows the largest design of square membranes. Created in the mask are the pads that connect the wire bonds to the contact planes. These pads have the same location for each die, irrespective of the design.

Figure 2.31 shows a zoomed-in illustration of Figure 2.30a. The separation between the different contacts is visible in this figure. The spacing between each contact is  $2\mu m$ . This causes additional capacitance between the contacts, however, it has been calculated that this is negligible compared to the capacitance change due to the membrane. A photo of this mask is shown in Figure 2.28.

#### 2.6.4 Mask 2 - Membrane hole etch mask

The next mask is a multipurpose mask. First, it will be used to create small structures on the bottom of the cavity. These structures will make sure that once the membrane touches the bottom, the membrane will not stick. These structures are therefore called anti-stiction structures. The second use is when the sacrificial structures have been created and a thin layer of membrane material is added. This mask will etch holes inside the membrane material to release the sacrificial material.





Figure 2.31: Zoomed-in illustration of mask 1 of a circular sensor with 5 bottom contacts. Different colours are used to differentiate between the individual contacts

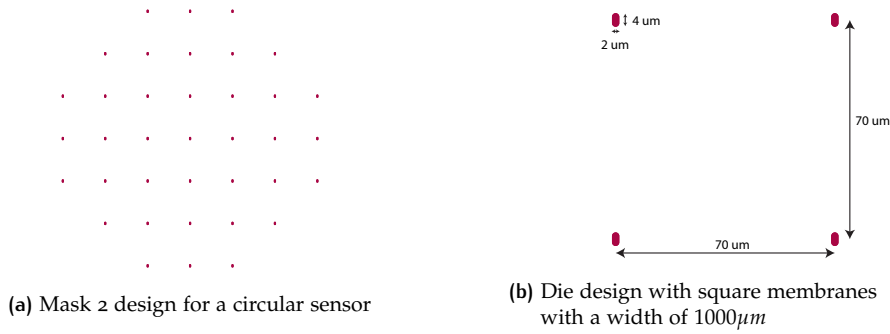


Figure 2.32: Zoomed-in design of Mask 2

The holes created have dimensions of  $2\mu\text{m}$  by  $4\mu\text{m}$ . A close-up of the design can be seen in Figure 2.32b. This size is considered the maximum size for these holes. When the thicker layer of the membrane is deposited after the sacrificial material is released, the holes need to close properly. If the width of these holes is maximally half the thickness of the closing layer, the holes will close properly [17].

The holes are spaced  $70\mu\text{m}$  in the x-and y-direction to ensure that sufficient sacrificial material can be released. The pattern follows the shape of the sensor, so a circular sensor will have holes that have a circular pattern as shown in Figure 2.32a. All holes closer than  $70\mu\text{m}$  to the edge of the membrane are removed.

### 2.6.5 Mask 3 and 4 - Sacrificial layer definition

The next two masks, masks 3 and 4 have similar functionality. They determine the shape of the sacrificial layer. The sacrificial layer will eventually be coated with a thin layer of SiC. Therefore, the shape of the sacrificial layer should be the same as the cavity will be later on. To get the sacrificial layer to the correct shape, wet etching will be used. This process is isotropic, therefore it will etch in all directions. Because of this property, the material will be etched downwards as well as directly under the mask. The result is that the resulting shapes will be smaller than the masks.

To counter this effect, the shapes on the masks have to be designed bigger than the final shapes. The extra width of the masks is dependent on the height of the sacrificial structure and thus the gap height. For the design, four different gap heights will be created. The first two heights  $7\mu\text{m}$  and  $8.5\mu\text{m}$  are used for the low and high-range sensors and the other heights,  $10\mu\text{m}$  and  $14\mu\text{m}$ , are used for the mid-range pressure sensor. To reduce the number of masks necessary, the designs for  $7\mu\text{m}$  and  $8.5\mu\text{m}$  are placed on Mask 4 and the designs for  $10\mu\text{m}$  and  $14\mu\text{m}$  are

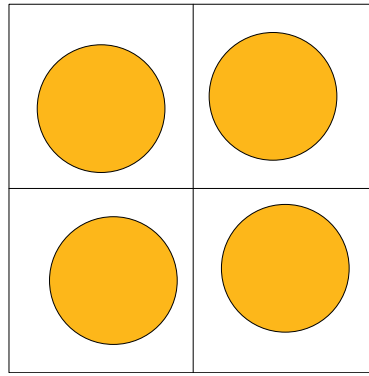


Figure 2.33: Circular design of Mask 3 and Mask 4

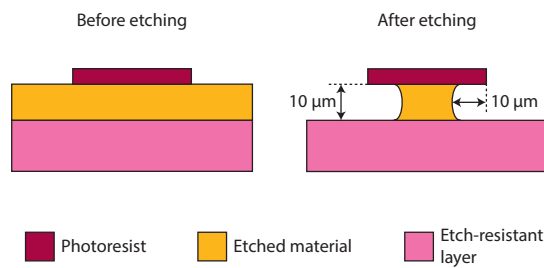


Figure 2.34: An illustration of isotropic etching

placed on Mask 3. The process will be adjusted for either the smaller or bigger gap height. This means that it is not possible to create both gap heights of  $7\mu m$  and  $8.5\mu m$  on the same wafer. However, since both designs can be created, the performance difference can be evaluated. The design of the two masks for one die can be seen in [Figure 2.33](#)

Because the etching is isotropic, the horizontal and vertical etch rate is the same. This means that for a gap height of  $10\mu m$ , the vertical and horizontal etch distance will be  $10\mu m$ . Therefore, to counter the horizontal etch rate, each edge on the mask has to be moved with the same amount. An illustration is shown in [Figure 2.34](#). Therefore for the circular designs, the mask radius is the sum of the membrane radius and the gap height. For the square designs, the width is the sum of the membrane width and two times the gap height.

#### 2.6.6 Mask 5 - Sensor edge definition

After the sacrificial layer has been defined, a thin layer of the membrane is added. Holes are then created using Mask 2 and the sacrificial material is released. Finally, a thick layer of silicon carbide is added. However, this layer is placed over every part of the wafer. Mask 5, therefore, trims the Silicon Carbide layer to a size that is a little bigger than the sensors. A margin of  $20\mu m$  around the sensor edge has been taken. Since this type of etching is anisotropic, the mask size is the same as the desired sensor size. For this reason, the mask design looks similar to [Figure 2.33](#), but the shapes are slightly bigger.

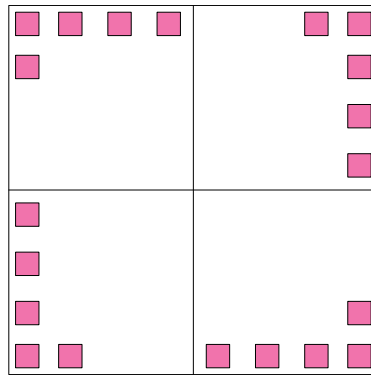


Figure 2.35: The universal die design of Mask 6

### 2.6.7 Mask 6 - Opening Via holes

Now the sensors have been defined correctly, the bottom contacts need to be exposed again. Afterwards, these contacts can be connected with wire bonds to the package around the sensor. The via-hole design is the same for every die to ensure consistency across all designs. [Figure 2.35](#) shows the design for the via holes of each die.

### 2.6.8 Mask 7 - Overlay metal layer

The final mask will shape the metal on the top of the membrane. In addition, it connects to the bottom contacts through the vias. This metal will be used to add wire bonds during the final production steps. As mentioned, a lift-off technique will be used to create the correct structure. In addition to the structure, the pads are all marked with the corresponding function, and each die has an individual identifier that marks what designs are placed on the die. An example of a design is shown in [Figure 2.36](#)

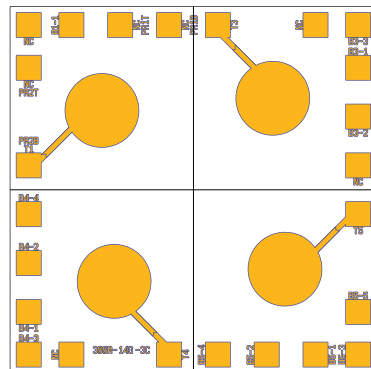


Figure 2.36: A design for Mask 7

# 3 | PROCESS

Up to this point, the pressure sensor has been simulated, masks have been designed, and key fabrication steps have been thought out. Having completed these steps means that the sensor is done, theoretically speaking. However, physically, nothing has been constructed yet. This chapter will discuss fabricating the sensor in the [EKL](#). The first part of this chapter, [Section 3.1](#), discusses the underlying principles of each process and the intricacies of the cleanroom. It shines a light on the concept of contamination, the different techniques used, and the respective machines for these processes. After that, the key points of the flowchart document will be discussed in [Section 3.2](#). The flowchart is a required document for the laboratory. This document is a step-by-step reference to the entire construction process. Not only is this required from a contamination point of view, but the document is also necessary to keep track of the different steps that must be taken. After the flowchart has been discussed, the production will be reflected in [Figure 3.4.2](#).

## 3.1 CLEANROOM PROCESSES

The [EKL](#) supports a large range of processes that can be performed. For this sensor, some of these processes have to be carried out. This section lists and explains the techniques used. Before carrying out the fabrication steps, the project has to be compatible with the contamination rules in the laboratory. Therefore, the contamination principle will be discussed in [Section 3.1.1](#).

### 3.1.1 Contamination

The cleanroom allows for many different processes for different devices. From the production of transistors to MEMS sensors and from nanoparticle-based devices to biocompatible instruments. Even though each process is made on a distinct scale, each requires the laboratory to be clean. Hence, the name cleanroom. Especially for small devices, like the production of transistors, contamination can greatly affect the fabricated products. There are many sources of contamination, which can roughly be divided into four categories: Air molecular contamination, Organics, Particles, and Ionic contamination [\[67\]](#). To prevent contamination via air molecules, instruments have been installed that regulate airflow and suppress floating dust particles. To prevent organics and particles, the wafers must be cleaned if they have not been processed for at least three hours. Finally, to prevent ionic contamination, substrates that contain certain metals like copper or gold cannot be used in equipment used for clean wafers. These metals, called red metals, can alter the conduciveness of the substrate by penetrating the silicon. Therefore, the processing steps are limited to contaminated equipment if these metals are used.

### 3.1.2 Cleaning

As mentioned before, wafers must be cleaned regularly to prevent contamination. In addition to contamination prevention, cleaning steps are also used to remove photoresist layers. The standard cleaning steps for wafers start with a plasma wafer

strip step. The equipment, the *Tepla Plasma 300*, creates a plasma where the substrates are placed. This plasma burns away all organic materials, such as organic dust, photoresist, or other contamination. After this step, the wafers are placed in a nitric acid bath. Finally, after this nitric acid bath, the wafers are washed with demineralized water and dried.

### 3.1.3 Photoresist coating

Once the wafers are cleaned, other processes that are necessary for the design can be performed. One process is particularly important because it transfers the mask designs to the substrates. The masks created in [Section 2.6](#) can be placed directly on the wafers using this technique. This process is done by coating the wafer with a material that is sensitive to light. This material, called photoresist, changes chemical properties after exposure to light. Either the material hardens, making it indissoluble, or it will do the opposite and become dissolvable. When placing a mask between the light source and the coated wafer, specific regions can be exposed to light, while other areas will be shaded. There is a limit on how small the features can be that will be transferred. In [EKL](#), the smallest feature size is about  $1\mu\text{m}$ .

The whole procedure of coating with a photoresist is as follows. First, the substrate is prebaked and coated with vapourised HDMS. The prebake makes sure there is no water left on the wafer, and the HDMS coating will add a monolayer of material to make it more attractive to photoresists [68]. After this preparation, the second step is to spin-coat the photoresist on the substrate. The thickness of the applied layer is predominantly dependent on the rotation speed [69]. The third step is to soft-bake the substrate with the photoresist. This makes sure the photoresist is firmly fixed on the wafer.

After the photoresist coating is completed, the wafer can be exposed. For this process, the *ASML PAS 5500/80 waferstepper* is used to etch the alignment markers for the next masks. These alignment markers are discussed in [Section 2.6.1](#). The rest of the exposing is done on the *SUSS MicroTec MA/BA8 mask aligner*. This machine allows for a manual alignment of a full-wafer mask without magnification.

When the photoresist has been deposited and exposed, the excess has to be removed. This is done in the *EVG 120 Coater-Developer*. This machine develops the photoresist and cleans the excess material by spraying it with deionised water. Once the wafers have been cleaned and dried, the photoresist coating is complete. The mask has been transferred to the substrate, and this photoresist layer can, in turn, serve as a mask for further processing.

### 3.1.4 Deposition

Once the photoresist layer is added to the substrate, the materials on the substrate can be selectively removed. However, before removing materials, layers first have to be deposited. There are many methods of depositing material on substrates. The techniques that are used for this process will be discussed in this subsection.

#### PECVD

The first technique that will be used is [Plasma-enhanced chemical vapor deposition \(PECVD\)](#). This technique uses RF energy to create and sustain the plasma. Once this plasma is in place, precursor gasses enter the reaction chamber. The precursor gasses bump into the highly energetic plasma particles and form a layer of the specified material on the wafer. The byproducts are pumped away after formation [70]. The advantage of this technique is that the substrate does not have to be heated to a very high temperature because the reaction of the gasses is powered by the plasma. In addition, this technique can deposit a large variety of films, and it can deposit these films very uniformly [70]. The machine used for [PECVD](#) depositions

in the [EKL](#) is the *Novellus Concept 1*. The different materials that can be deposited on the substrate are:

- SiO<sub>2</sub> (at 350°C, TEOS)
- SiO<sub>2</sub> (at 400°C)
- SiN<sub>x</sub> (at 400°C)
- SiC<sub>x</sub> (at 400°C)

### ***Sputtering***

Another technique that can be used to deposit materials is sputtering. This technique creates a plasma between a cathode and an anode. The cathode contains the material to be deposited, and the substrate is placed on the anode. Due to the charge difference between the cathode and anode, the plasma ions are accelerated to the cathode, bumping into the source material. This releases enough energy to break chemical bonds between the atoms. Once the chemical bonds are released, the atoms of the source material are flown away and end up on the substrate. A layer of the source material will form as a result of this spraying [71]. The machine used for sputtering in [EKL](#) is the *Trikon Sigma 204*. The different materials that can be deposited on the substrate are:

- Al (Aluminium)
- Mo (Molybdenum)
- Zr (Zirconium)
- Cu (Copper)
- Nb (Niobium)
- Ni (Nickel)

### ***LPCVD***

After the sputtering, a technique that is similar to [PECVD](#) will be used. In contrast to this technique, [LPCVD](#) can deposit materials at low pressure. The process uses temperature to form a layer from precursor gasses. The reaction chamber has very low pressure, enabling a uniform layer deposition on the substrates [72]. The machine for depositing is the *LPCVD Furnace F3*. This machine can deposit layers of:

- SiN<sub>x</sub>
- SiC<sub>x</sub>

### ***Electron Beam Evaporation***

The last deposition technique used is Electron Beam Evaporation. In this technique, the target material is bombarded with electrons that are released from a tungsten filament under a vacuum. The electrons are guided using magnetic fields towards the target. At the impact, the energy causes the target material to be converted to a gaseous state locally. The released gas flies all over the reaction chamber and some of the gas will end up on the substrate and precipitate. This will slowly form a layer on top of the substrate with the target material /citeebbeam. The machine for depositing using the Electron Beam Evaporation technique is the *CHA Solution Std.*. Using this machine, the following materials can be deposited:

- Ti (Titanium)

- Al (Aluminium)
- Ta (Tantalum)
- Cr (Chromium)
- Fe (Iron)
- Au (Gold)
- Pt (Platinum)

### 3.1.5 Etching

In contrast to deposition, the [EKL](#) also has techniques to remove materials. There are two main methods of removing materials. Either by plasma dry etching or by wet etching. Not only is there a difference in selectivity between the various techniques, but the directionality between the methods is also different as well. The dry etching is anisotropic, meaning that the etched direction is perpendicular to the substrate, while the wet etching is isotropic. This means that the etching will go in every possible direction. This has also been discussed in [Section 2.6.5](#), where the sacrificial mask is designed.

#### *Plasma dry etching*

The first method of etching used is plasma dry etching. This type of etching uses a chemically reactive plasma in a vacuum chamber [73]. This plasma is created and stripped of its electrons by an oscillating electric field. The electrons move around and end up on the inside of the chamber and the substrate. The interior of the chamber is grounded, but the substrate picks up the charges. The substrate slowly becomes negatively charged, and the positive ions in the plasma slowly move toward the substrate. The ions react with the top layer of the substrate, removing the layer atom by atom. This technique is highly directional because the plasma moves perpendicular to the surface of the substrate. This means that the etching direction is directly inside the substrate. The machine used for dry etching is the *Trikon Omega 201*. This machine can etch many different materials, but the materials that are relevant for this project are:

- Mo (Molybdenum)
- SiN<sub>x</sub> (Silicon Nitride)
- SiC<sub>x</sub> (Silicon Carbide)

#### *Wet etching*

Wet etching works on the principle of dissolving a material in a certain liquid. This means that the liquid will react with the material on the substrate to form a soluble product in the liquid. Because there is no directionality in the liquid or the reactions, the etching will occur on each unobstructed interface equally fast. For this process, two wet etching solutions will be used predominantly. The first is  $HNO_3$ . This is used to clean the wafer of organic materials during cleaning steps and to remove the leftover photoresists. The second is *BHF*. This Buffered HF solution can etch Silicon Oxide but cannot etch more inert materials, like Silicon Nitride and Silicon Carbide. In addition, the photoresist is barely etched either. Because of this selectivity, BHF is often used to create hard masks.

### 3.2 FLOWCHART

After creating a basic understanding of the different cleanroom processes, the production process can be defined. This process is shown in a flowchart, explaining each operation step by step. Each step includes details like recipes and times used. Once the flowchart is approved by the contamination manager, the production process can start. This section will not display every step in detail but rather give a summary of the different sections in the flowchart. The recipes, time, and materials details will be discussed in [Section 3.3](#). The different steps, starting from the application of the passivation layer, are illustrated in [Figure 3.1](#).

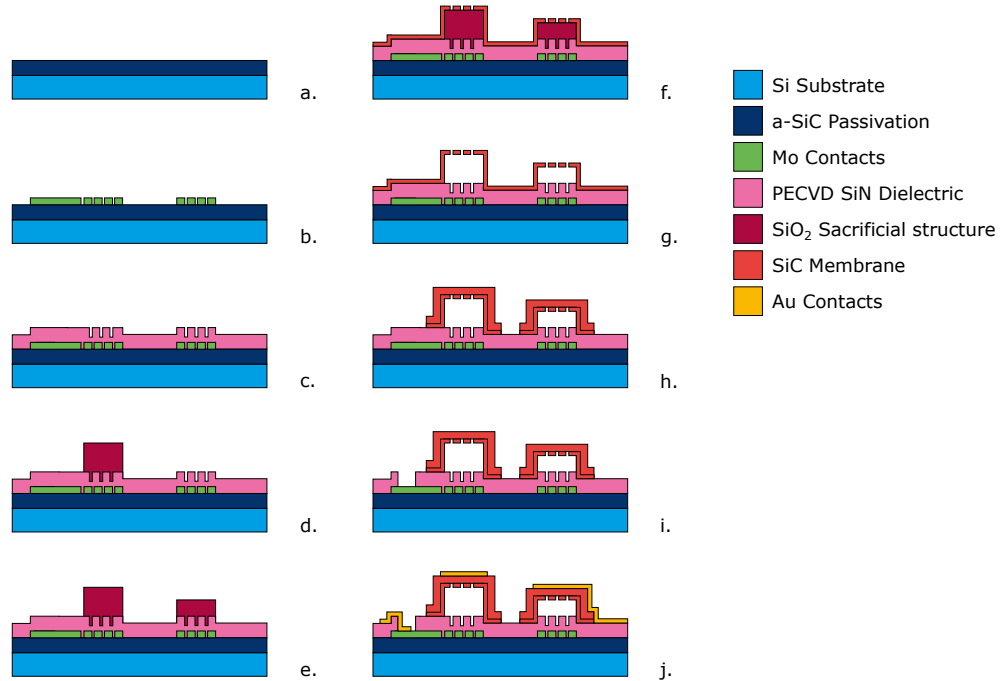


Figure 3.1: The stages of the process as described in the flowchart

#### Preparation of the substrate

Upon unpacking new wafers, the substrates are clean and do not have to be cleaned. The first step, therefore, is to create a patterned layer with a photoresist. This patterned layer contains the alignment marker so the rest of the masks can be aligned properly. This patterned layer is etched into the wafer, and the layer is cleaned.

#### Application of passivation layer

After preparing the substrates, the first stage is adding a passivation layer to the wafers. This passivation layer will protect the circuits that can be present in the substrate. In addition, the passivation layer makes sure that the bottom contacts cannot electrically short with the silicon below. The result is shown in [Figure 3.1\(a\)](#).

#### Construction of bottom-contacts

Now the substrate is properly protected from the structure of the sensor, the bottom contacts can be created. The material for the bottom contacts is Molybdenum. The reason for this material is that molybdenum is considered a green metal, as discussed in [Section 3.1.1](#). This means that even though metal is placed on the wafer, most of the machines and processes in EKL can still be used. The layer is first sputtered on the wafer. Afterwards, the metal is patterned so the contacts are placed correctly. Patterning is done by using a photoresist layer and mask 1.

After these steps, the substrate should correspond with the schematic figure as shown in [Figure 3.1\(b\)](#).



### Application of dielectric layer including anti-stiction structures

After the bottom contacts are formed, a dielectric layer is added to prevent short circuits when the membrane reaches touch mode. Even for sensors that will not reach touch mode in the full range, the dielectric layer is added as protection against pressures higher than the intended range.

The material is first deposited on top of the wafer, and afterwards, a pattern of small holes will be etched. This ensures that the membrane does not permanently stick to the bottom of the cavity and rip open when the pressure decreases. An important detail is that these holes should not be the full thickness of the dielectric layer. Otherwise, a short circuit might still occur through the hole.

After these steps, the substrates should correspond with [Figure 3.1\(c.\)](#).

### Construction of sacrificial structures

The final sensor has a free-floating membrane. However, such a membrane cannot be formed in free air. To solve this, a sacrificial structure will be created that takes the shape of the space inside the membrane. This structure will be removed once the membrane is placed. The material of this sacrificial material is Silicon Oxide. Therefore, this material will be deposited first. The chosen designs of the sensor allow for different gap heights. Therefore, two masks are made for these sacrificial structures. One mask for low structures and one mask for high structures. First, the sacrificial material will be deposited and etched to conform to the highest gap. Afterwards, another layer of sacrificial material will be deposited and etched at the same height as the lowest gap. This will result in two distinct heights.

The substrate should now correspond with [Figure 3.1\(d.\)](#) after the first structures have been created and [Figure 3.1\(e.\)](#) after the rest of the structures have been formed.

### Construction of the first (thin) SiC layer with release holes

The deposition of the sacrificial material finalised the shape of the sensors. On top of the structures of the sacrificial material, the membrane material can be deposited. This will result in cylindrical and cuboid-shaped sealed sensors. In this layer, release holes are created to enable the sacrificial material to be removed. The wafers should correspond to [Figure 3.1\(f.\)](#).

**Removing of the sacrificial structures** The thin Silicon Carbide membrane now has holes through the layer. The sacrificial layer that is present under the membrane can be removed using vapour HF etching. This is done in the *HF Vapor Etcher Primaxx uEtch HF SPTS*. Visually, progress can be followed under the microscope. When all of the sacrificial layer material is removed, the vapour HF treatment is finished. Now, the substrates should resemble [Figure 3.1\(g.\)](#).

**Construction of the thick SiC membrane** At this moment, the thin membranes are floating with a little support of Silicon Carbide. The wafers get an additional coat of silicon carbide to make the structures more rigid and gain the correct membrane thickness. In addition, the release holes will be sealed so the sensors will be functional. The excess silicon carbide around the sensors will be removed. After this step, the wafers should now correspond to [Figure 3.1\(h.\)](#).

**Construction of via's to contact bottom-contacts** With the previous steps finished, the membrane is defined completely. Now, the contacts from the bottom have to be retrieved. At the start of the process, the bottom contacts have been covered with a passivation layer. Now, this passivation layer has to be removed again. Coating the structures in photoresist and dry-etching will reveal the contacts again. With the bottom contacts revealed, the substrates resemble [Figure 3.1\(i.\)](#).

### 3.2.1 Creation of overlay layer

The last steps are to create a second metal layer. This metal layer serves as the top electrode and an overlay material that can be used to create wire-bonded connections. Finally, this layer adds some text to identify the different dies that are made. The wafers should now look like [Figure 3.1\(j.\)](#).

## 3.3 CLEANROOM PRODUCTION

After preparing the masks and an approved flowchart, the cleanroom process can begin. First, new wafers are received, and the flowchart is followed step by step.

The cleanroom production and final sensors have not been achieved in one go. The initial ideas did not always work as expected. Therefore, some adaptations have been made to the original process. This section shows the attempts, the problems encountered, and the steps used eventually. For an overview of the successful steps, a marking like this paragraph features has been placed next to the ultimately used steps.

### 3.3.1 Etch rates and deposition rates

In addition to the processing, tests were performed to find different materials' etch rate and deposition rate using wet etching, dry etching, [LPCVD](#) or other techniques. [Table 3.1](#) shows the result of the tests. The deposition rate has been determined using the *Woollam ellipsometer*. Etch rates have been determined using this same method but also using the *Dektak*.

#### *Determining the etch rates and deposition rates using the Woollam ellipsometer*

The *Woollam ellipsometer* uses ellipsometry to determine film thicknesses on samples. When a wafer is placed in the machine, measured data is compared to optical models of the materials on top of the silicon [74]. To use this approach, the exact stack of layers on top of the silicon has to be known. Therefore, it is advised to analyse the wafer before depositing a layer. After an analysis, a layer can be deposited and using the models and an estimation of how thick the layer is, the software can determine the exact thickness of the layer.

For etching, the process is similar. Before etching, the thickness of the material is determined. Then the material is etched, and the result is placed in the *woollam* again. The difference in layer thickness is the amount that has been etched.

#### *Determining the etch rates using the Dektak*

The *Dektak 8* is a tool that uses a sharp needle to determine the profile on top of a sample. By measuring the vertical movement of the needle, the profile of a line is determined. This tool is especially useful if structures have to be created and the height of the structures has to be measured.

To obtain etch rates using this tool, the process is as follows. First, a layer of photoresist or any other masking material is applied and patterned. Then, the *Dektak* is used to determine the height of the photoresist layer. Now, the wafer is etched, and the step height is determined again. Finally, the photoresist is removed, and the step is measured one last time. The etched amount of the material and the photoresist can be obtained using these different step measurements. This also means that the selectivity can be found between the masking material and the etched material. An illustration of this process is shown in [Figure 3.2](#)

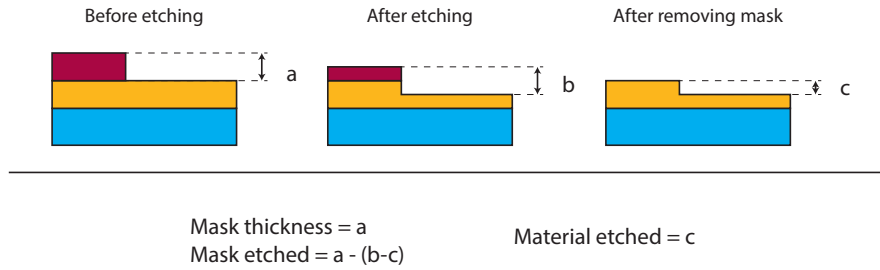


Figure 3.2: Illustration of using step heights to determine the amount etched from a mask and the material

### Established etch rates and deposition rates

In Table 3.1, the different etch rates and deposition rates have been displayed. In addition, the technique, recipe and time are added.

Table 3.1: The etch rates of the different layers using the etch techniques necessary

Material	Technique	Recipe - time	Total etched - etch rate
Molybdenum	Dry etching	Mo_50NM 2:00 min	140 nm 1.10 nm/s
Photoresist	Dry etching	Mo_50NM 2:00 min	990 nm 8.25 nm/s
Silicon Oxide	Dry etching	Mo_50NM 4:00 min	434 nm 1.81 nm/s
Silicon Nitride	Dry etching	Mo_50NM 0:30 min	133 nm 4.43 nm/s
Silicon Oxide	Wet etching	BHF 2:00 min	511 nm 4.26 nm/s
Silicon Oxide (TEOS)	Wet etching	BHF 2:00 min	314 nm 2.62 nm/s

### 3.3.2 New wafers

The cleanroom production starts with new wafers. Even though the process is meant for Silicon Carbide wafers, the process is first tested on Silicon wafers. These wafers are less expensive, and because the silicon itself will not impact the functionalities of the sensor, this material can be used. The properties of the wafers that are used in processing are shown in Table 3.2

Table 3.2: The properties of the Silicon wafers used for processing

Part no:	BW14057	Lot. No:	316995
Diameter:	100 ± 0.3mm	Surface finish:	Single Side Polished
Grade:	Prime	Flats:	2, SEMI-Std.
Growth:	CZ	TTV:	< 5μm
Orientation:	< 100 > ±0.5%	Bow:	< 30μm
Resistivity:	1 – 5Ω – cm	Warp:	< 30μm
Thickness:	525 ± 15μm	Particles:	< 10@0.3μm
Type/Dopant:	N/Ph	Lasermark:	Frontside next to primary Flat

### 3.3.3 Preparation of the substrate

The first part of preparing the substrate, as indicated in the flowchart, is to cover the wafers in photoresist so alignment markers can be placed. However, because the HDMS station of the *EVG120 Spincoater and Developer* was not working at the time of processing, a manual HDMS coating has to be done before applying photoresist. The substrates are placed in a chamber where HDMS is vapourised for 10 minutes. Afterwards, a layer of HDMS is present on the substrates. The quality of this layer is less than it would be if the devices were coated in the *EVG120 Spincoater and Developer*, because this process is not done at elevated temperatures [68]. However, for this process, manual HDMS is sufficient.

After manually applying the HDMS, the wafers are coated with a layer of  $1.4\mu\text{m}$  photoresist. This is done using the recipe **SpeCo\_3012\_1.4um\_noHDMS\_noEBR** on the *EVG120 Spincoater and Developer*. Next to placing the photoresist, this recipe also applies a soft bake at  $95^\circ\text{C}$  for 90 seconds. Next, the wafers are placed in the *ASML PAS 5500/80* automatic wafer stepper. This machine exposes the alignment markers using the **COMURK** mask and the **Zefwam** recipe. Unfortunately, because of an error made in the first batch of wafers, the exposing energy is only  $105\text{mJ}/\text{cm}^2$  instead of the intended  $120\text{mJ}/\text{cm}^2$ . After visual inspection under the microscope, this lower energy suffices. The next wafers have the correct exposing energy.

After exposing, the wafers are developed in the *EVG120 Spincoater and Developer*. The recipe **Dev\_SP** is used. This recipe first uses a post-exposure bake at  $115^\circ\text{C}$  for 90 seconds. Afterwards, development is done with Shipley MF322. A single-puddle process is used, meaning the wafers are developed with the liquid only once. Finally, a hard bake is performed at  $100^\circ\text{C}$  for 90 seconds.

A visual inspection confirms the placement of the photoresist and if it is exposed and developed correctly. Afterwards, the wafers are etched using dry-etching. This is done in the *Trikon Omega 201*, using the sequence **urk.ndp** with a platen temperature of  $20^\circ\text{C}$ . This will etch  $120\text{nm}$  deep structures in the silicon.

Now the structures are etched in the silicon, the photoresist can be removed. To remove this, the wafers are placed in the *Tepla Plasma 300*, using **Program 1**. This uses an oxygen plasma to clean most of the photoresist. Afterwards, the wafer is washed in  $\text{HNO}_3$  baths to remove the remains. The cleaning procedure for these baths is: bathing for 10 minutes in 100%  $\text{HNO}_3$  at room temperature and cleaning in deionised water until the resistivity of the bath exceeds  $5\text{M}\Omega$ . Afterwards, the wafers are placed in 69.5%  $\text{HNO}_3$  at elevated temperature for 10 minutes. The wafers are rinsed again in a deionised water bath until the resistivity exceeds  $5\text{M}\Omega$ . Finally, the wafers are dried manually or in the *Avenger Ultra - Pure6*.

Unfortunately, an error was made during the ordering of the mask. Therefore the polarity of the masks is reversed. The result is that the masks are the mirror image as they have been designed. For the process, this does not matter, but for the alignment marker, this is a problem, since they do not have line symmetry. The mismatch that occurs makes it difficult to align masks to the markers. The result is shown in [Figure 3.3](#). The solution that is used is to align the masks to the outline of the alignment marker. Because this is line-symmetric, it can be used, even though there are fewer details to align to, as shown in [Figure 3.3b](#).

### 3.3.4 Application of the passivation layer

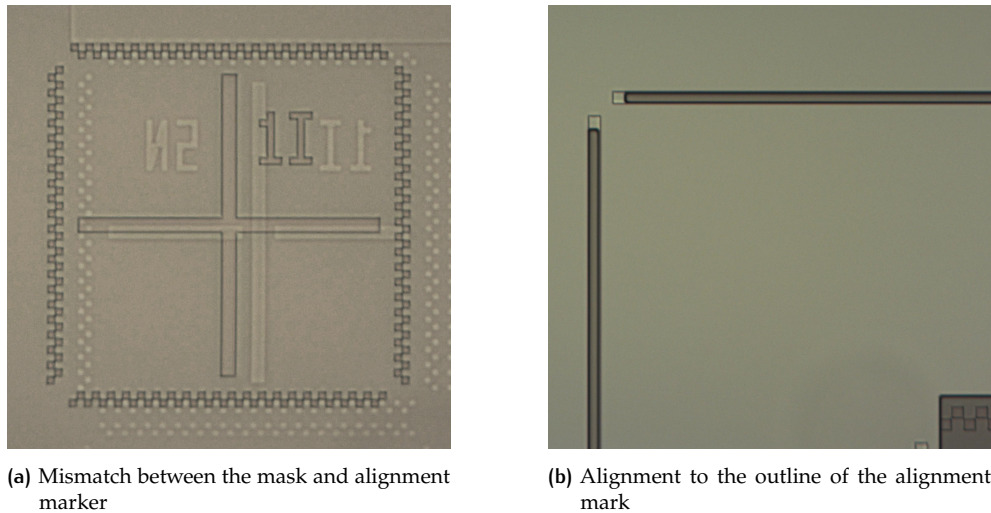


Figure 3.3: Alignment of the alignment mark with mask 1

The passivation layer is now deposited using the *Novellus Concept 1*. The recipe used is **LS800nm\_2** for 55 seconds. The result is a passivation layer of 500nm. This suffices for the process. A four-probe measurement is done to test for the conductivity, and a Gain Set Error is returned. This indicates that the wafer is passivated successfully.

### 3.3.5 Construction of bottom-contacts

The first step in constructing the contacts is to deposit the contact material. The chosen material is molybdenum. This metal has a high melting point of 2623°C. In addition, it is a green metal in the cleanroom, meaning that most processes are possible even if this material is deposited.

The deposition is done in the *Trikon Sigma 201*. A layer of 200nm is deposited with the recipe **Mo\_200nm\_340C\_5kW**. This layer is visually inspected, and a 4-point probe is used to determine the material's conductivity. The average sheet resistivity is 0.8Ω/□.

Next, this metal has to be patterned and etched, so the contacts are formed. The first attempt that was performed used dry etching. First, a photoresist layer is added and patterned with the mask for the bottom contacts. The same procedure for photoresist coating is used as described in [Section 3.3.3](#), except for the photoresist layer thickness. A layer of 3.1μm is used for this with the recipe **SpeCo\_3027-3.1um\_noHDMS\_noEBR**. After exposing using the design of Mask 1 for 75 seconds on the *SUSS MicroTec MA/BA8 mask aligner* and developing, the photoresist is applied. Next, dry etching is used to remove the excess material. The *Trikon Omega 201* is used with the recipe **Mo\_50nm**. The platen temperature is set to 25°C, and the etching is repeated until the metal is fully removed. This was tested with resistivity measurements. Finally, the photoresist is removed, and the wafer is cleaned. Instead of using HNO<sub>3</sub>, cleaning is done with a treatment of acetone, followed by a treatment of [Isopropyl alcohol \(IPA\)](#). The reason is that molybdenum is etched by HNO<sub>3</sub> and cannot be cleaned with this material. Eventually, a result similar to [Figure 3.4](#) is obtained.

During a lab meeting after performing these steps, a worry arose that the metal layer could not be cleaned perfectly. As a result, the layer on top of the molybdenum may detach from the metal. If instead of a photoresist mask, a hard mask of [Silicon dioxide \(SiO<sub>2</sub>\)](#) is placed directly on top of the Molybdenum, the surface of the metal stays much cleaner, and the next layer has a higher chance of sticking to the surface.



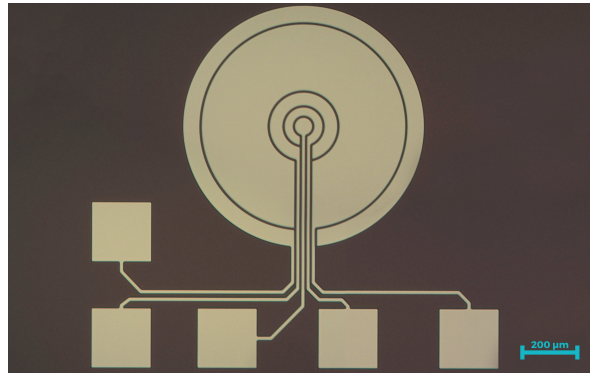


**Figure 3.4:** Etched Molybdenum contacts using dry-etching. A combination of four microscope photos are stitched together for this result

Therefore, the process that has been used eventually has a layer of  $\text{SiO}_2$  that is deposited directly after the molybdenum is placed. Because the etch rates for molybdenum and silicon oxide are very similar, only  $330\text{nm}$  of the oxide was required to etch the molybdenum. To add a little buffer,  $500\text{nm}$  of  $\text{SiO}_2$  is deposited. This is done in the *Novellus Concept 1* using recipe **xxxnmteos**. Afterwards, a photoresist layer of  $3.1\mu\text{m}$  can be applied, exposed and developed

To get the patterns in the molybdenum, two methods were attempted. The first method uses wet etching. The  $\text{SiO}_2$  is etched readily by **Buffered hydrofluoric acid (BHF)**, while this solution barely etches silicon, photoresist and molybdenum. Therefore, the wafer is placed in this acid to etch away the  $500\text{nm}$  of  $\text{SiO}_2$ . Afterwards, the photoresist can be stripped, resulting in an oxide mask with the same pattern as the photoresist. Now, dry etching can be used to pattern the metal underneath. This workflow is shown in **Figure 3.5a**.

This method was attempted, but after wet-etching the oxide, the isotropic nature of this etch is visible. **Figure 3.5b** shows the result of this attempt. By reducing the etch time, the result improved. However, the oxide is not etched away fully. Another compromise is to leave the photoresist on until after the dry etching. This improved the result as well, but it was still not perfect.

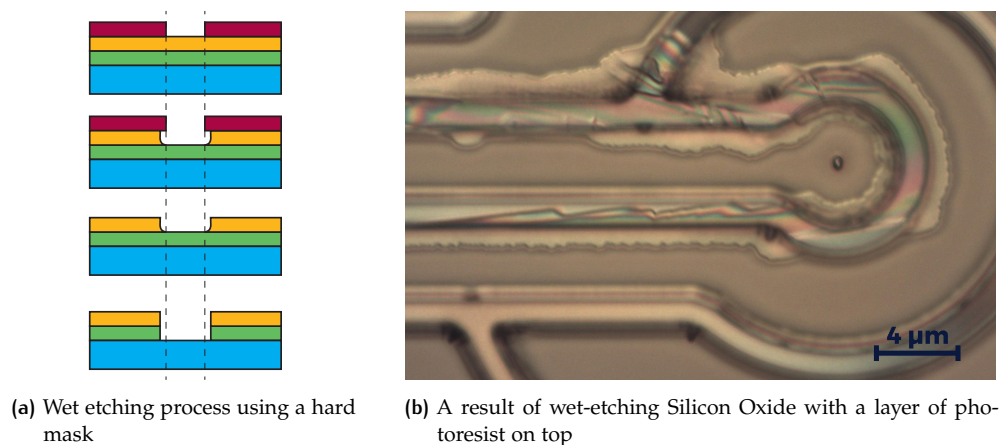


**Figure 3.5:** Wet etching using a hard mask

The second method attempted was to dry-etch the oxide only using the *Drytek Triode 384T*. This machine has a high selectivity for  $\text{SiO}_2$ . Therefore, it only etches the oxide. Recipe **stdoxide** was used for 1.5 minute. After the oxide was etched, the photoresist was removed in the *Tepla Plasma 300*. Finally, the

molybdenum was etched in the *Novellus Concept 1*, using the recipe **Mo\_50nm** for 7 minutes. The resulting surface was tested for conductivity, and when this was not the case, the  $\text{SiO}_2$  was removed in **BHF**. This method displays a result in [Figure 3.4](#). This is similar to before, but the metal surface is kept cleaner. Therefore, this technique is used in the final production of the sensor.

### 3.3.6 Application dielectric layer including anti-stiction structures

A passivation layer is added to the design to protect the metal layer from short-circuiting. Theoretically, this layer is not strictly necessary because the **SiC** membrane is not conductive in an undoped state. However, the layer also protects the metal traces outside of the membrane area. Due to some problems with the passivation material, the final designs do not feature a passivation layer at all. Before making this decision, there were a few attempts to create a passivation layer.

The first attempt at creating the layer was to use a **PECVD**-based  $\text{Si}_3\text{N}_4$  layer. This nitride layer was not conductive and was deposited using the *Novellus Concept 1*. Next, a layer of  $500\text{nm}$  was placed using the recipe **xxnm\_std\_sin** for 20.5 seconds.

After adding photoresist with a thickness of  $3.1\mu\text{m}$ , exposing Mask 2 and developing the layer, the substrates are placed in the *Trikon Omega 201* to etch small dimples. These holes should prevent stiction once the membrane touches the bottom of the cavity. The etch rate for dry etching silicon nitride using the recipe **Mo\_50NM** are shown in [Table 3.1](#). For the holes, a 30 seconds etching time is used. This results in holes with a depth of  $130\text{nm}$ , which is shallow enough to leave a layer of silicon nitride on top of the metal. Finally, the photoresist is removed. The result is shown in [Figure 3.6](#). The green hue in the picture is due to the thin layer of silicon nitride. And even inside the holes, the same green hue is visible, indicating that the metal is covered correctly.

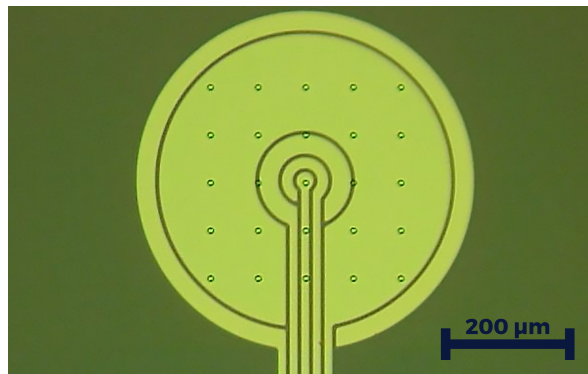


Figure 3.6: A circular sensor after etching the anti-stiction holes

Unfortunately, this layer proved to be problematic later in the process. Some steps later in the process, a layer of **SiC** was added as a membrane using **LPCVD**. This technique requires a high temperature of  $860^\circ\text{C}$  to deposit the necessary poly-SiC, and the layers ended up delaminated. The wafers ended as shown in [Figure 3.7c](#). Upon closer inspection using the microscope, it was visible that the layers delaminated specifically on top of the metal, as can be seen in [Figure 3.7a](#) and [Figure 3.7b](#). The regions where no metal is present did not suffer from any effects, even though the same layer stack is present.

There could be some reason for this delamination. The first reason could be that an unwanted reaction occurs during the **PECVD** process. **PECVD** uses gasses that react locally to create the deposition material. These gasses could react with the molybdenum instead of creating the intended product. The precursor gasses for  $\text{Si}_3\text{N}_4$  are  $\text{SiH}_4$  and  $\text{NH}_3$ . A possibility is that the molybdenum reacted with the  $\text{SiH}_4$ , forming  $\text{MoS}_2$ [75]. This could cause additional stresses that could not be re-

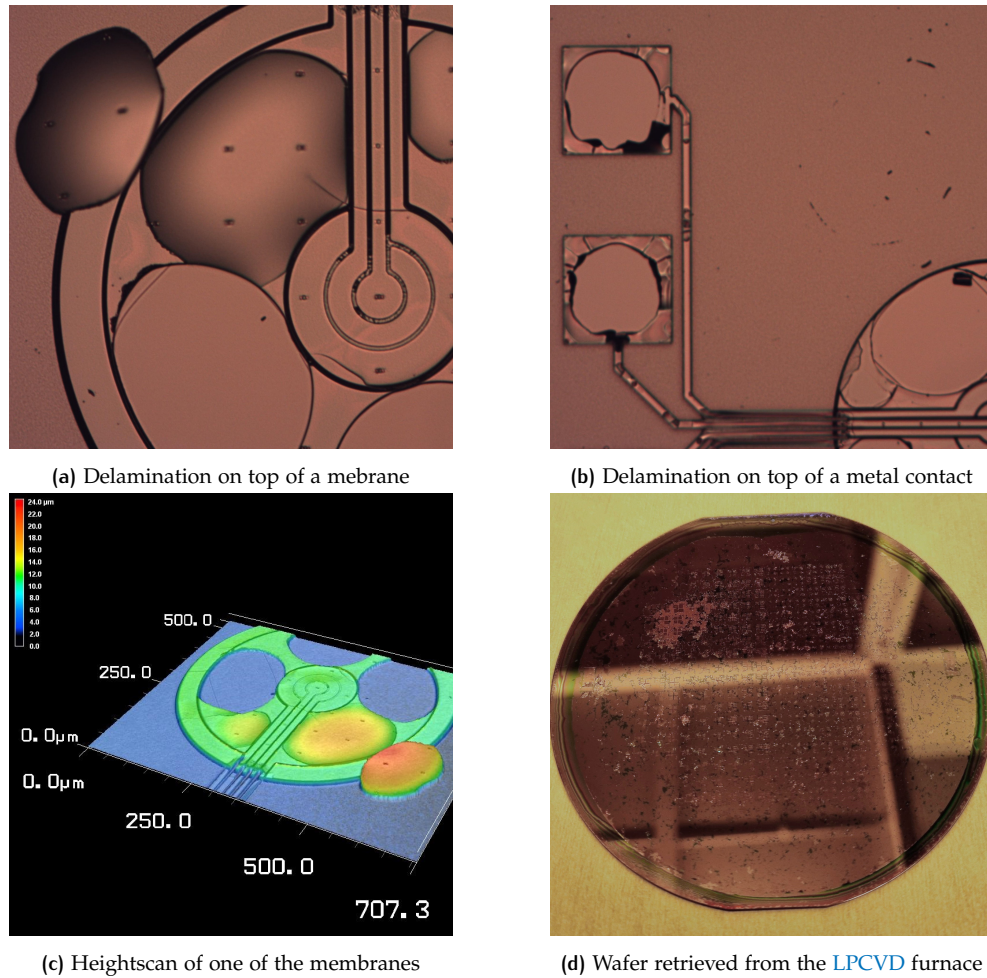


Figure 3.7: Delamination after LPCVD SiC deposition

leased at high temperatures. Another reason could be that the high temperature has an annealing effect, causing the nitride to change stress levels. A change in stress of PECVD nitrides has been seen in literature. The reason for it is the release of encapsulated hydrogen. During the deposition, hydrogen from the  $\text{NH}_3$  is encapsulated inside the nitride, and at high temperatures, the level of hydrogen is decreased compared to before annealing [76].

A solution to this delamination problem was necessary. Therefore, some tests were performed using different metal contact materials. First, aluminium was used as contact material. Even though the melting point of aluminium is low,  $660^\circ\text{C}$ , encapsulating the metal inside of a passivation layer should prevent it from moving. Next to that, Titanium was used as a contact material. This metal has a higher melting point of  $1668^\circ\text{C}$ . After placing a passivation layer on top of these metals and placing them in the LPCVD furnace, a similar delamination effect happened.

After these tests, a different passivation layer material was tried as well. Instead of PECVD  $\text{Si}_3\text{N}_4$ , PECVD SiC was used as a passivation layer. Even though this improved the results, the delamination was not completely gone, regardless of the metal used. Finally, instead of using LPCVD SiC as a membrane material, PECVD SiC was tested. Although this did not cause any delaminations, the physical properties of PECVD SiC are lacking in comparison to LPCVD SiC. The Young's modulus of the PECVD material is  $\frac{1}{3}$  of the LPCVD variant [77]. Even though this would still make a pressure sensor, the design cannot hold up to the pressures designed for. In addition, because this sensor needs to work at extreme temperatures, the PECVD solution was not pursued.



After all tests, the decision was made to skip the passivation layer completely. As mentioned, the layer should not be necessary for short-circuit protection because the membrane does not conduct. On the other hand, the anti-stiction holes will not be present in this layer. As an alternative, the release holes used in the membrane to remove the sacrificial layer will not seal up perfectly, creating dimples in the bottom of the membrane. These dimples will have an anti-stiction effect. When not adding the passivation layer, the delamination during LPCVD does not occur.

### 3.3.7 Construction of sacrificial structures

After deciding on not placing a passivation layer, the sacrificial structures have to be placed, and they have to be formed. This will be a two-part process because the different sensors require different membrane heights. First, sacrificial structures with the height of  $8.5\mu\text{m}$  and  $14\mu\text{m}$  will be placed. Then, the *Novellus Concept 1* is used to deposit the sacrificial material. This material will be silicon oxide, made using Tetraethyl orthosilicate (TEOS). The reason for using this precursor is that this type of  $\text{SiO}_2$  is more stable under high temperatures, decreasing the risk of delamination during LPCVD.

First, the highest structures are formed. Therefore, a layer of  $14\mu\text{m}$  of  $\text{SiO}_2$  is placed. The deposition is done in steps of  $3 - 4\mu\text{m}$  at the time. The recipe used for silicon deposition is `xxnm.teos`, with a time of 41.1 seconds for a  $3\mu\text{m}$  deposition. For a deposition of  $4\mu\text{m}$ , a time of 54.3 seconds is taken.

Because of the thickness of this layer, the stress inside the substrates is monitored. After depositing  $10\mu\text{m}$ , the stress is equal to  $-16.55\text{MPa}$ , and the bow over the entire wafer is  $14\mu\text{m}$  compared to without the added silicon oxide. With the additional  $4\mu\text{m}$ , the stress is  $-14.67\text{MPa}$ , and the bow is  $19\mu\text{m}$ . The intermediate steps are shown in Table 3.3.

Table 3.3: The stress and bow after each deposition of silicon oxide

Total layer thickness	Stress	Bow
$3.038\mu\text{m}$	$-22.43\text{MPa}$	$5.96\mu\text{m}$
$7.029\mu\text{m}$	$-18.33\text{MPa}$	$11.79\mu\text{m}$
$10.02\mu\text{m}$	$-16.55\text{MPa}$	$13.55\mu\text{m}$
$14.04\mu\text{m}$	$-14.67\text{MPa}$	$19.14\mu\text{m}$

Because tools like the spin coater use a vacuum to fixate the substrates, the bow is important to monitor. If the bow is too large, the vacuum cannot be sealed properly anymore. However, after consulting with experienced lab users, this level of stress and bow will not impose a problem in future stages of the fabrication.

After the deposit, a photoresist coating is added. The same procedure as before is used, with a photoresist thickness of  $3.1\mu\text{m}$ . Mask 3 is used for exposure, and a visual inspection verifies the photoresist layer. Finally, the development is done with a Single Puddle.

Now, the excess material can be removed, and this time wet etching is used because of the speed of Silicon Dioxide. The substrates are placed in BHF. The etch rate is approximately  $157\text{nm}/\text{min}$ , as seen in Table 3.1. This means that to etch the  $14\mu\text{m}$ , about 90 minutes of etching is necessary. This is done in steps of around 20 minutes to keep track of the progress and etch rate. The Dektak 8 is used to keep track of the etching progress.

A benefit of having no passivation layer is that the molybdenum contacts are bare after the sacrificial structure etch. Therefore, the conductivity of the

contacts can be used to determine if all of the  $\text{SiO}_2$  is removed properly. However, when removing the photoresist, the wafers cannot be cleaned in  $\text{HNO}_3$  anymore. Therefore, an acetone bath of  $40^\circ\text{C}$  is used.

The next step is to create shorter sacrificial structures. The deposition in the *Novellus Concept 1* is repeated, only this time, a layer of  $7\mu\text{m}$  is deposited. Afterwards, the wafer is coated with photoresist. Even though high structures are present, the photoresist layer thickness is still set to  $3.1\mu\text{m}$ . This is because the tall structures should not be coated with photoresist, and the coating of the low structures is sufficient at this thickness.

The excess material can be etched using  $\text{BHF}$  again. This time, the wafers should be etched for about 45 minutes. The molybdenum contacts will be bare again once the etching is done. Therefore testing for conductivity confirms that all  $\text{SiO}_2$  is etched properly.

After removing the photoresist in the same manner, an annealing step is performed. This step will decrease the chances of delamination at high temperatures. The downside is that the oxide will be harder to remove again.

Unfortunately, after the  $\text{SiO}_2$  was placed and photoresist was developed for the lower structures, some remains stayed on the wafer. These remains were situated mostly on and around the high structures. Therefore, the high designs were not etched gradually while etching for the lower structures. The result is that the edges of the tall structures are more irregular compared to the low structures. This is visible in [Figure 3.8](#). Especially the square membranes suffered from this effect.

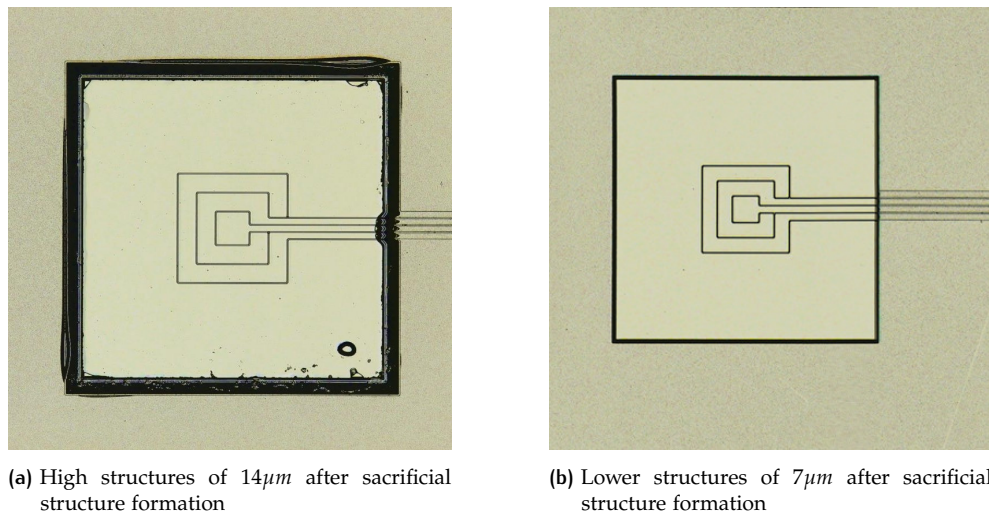


Figure 3.8: Result of sacrificial structure formation

A phenomenon observed after etching the oxide is that around the place where contacts left the membrane. An example of this is shown in [Figure 3.9](#). A possible explanation of this effect is that the pattern of the contacts is present in the layers above as well. The photoresist on top of the oxide also has this pattern, although in a lesser amount. While etching, the bottom of the photoresist will start to feature small channels parallel to the contacts on the bottom. Then, due to capillary action, the  $\text{BHF}$  acid is pulled in more fiercely than the rest of the membrane. With capillary action comes the effect that the smaller a hollow tube or channel is, the easier it is for a liquid to enter, explaining the locally higher etch rate [78].

### 3.3.8 Construction of the first (thin) $\text{SiC}$ layer with release holes

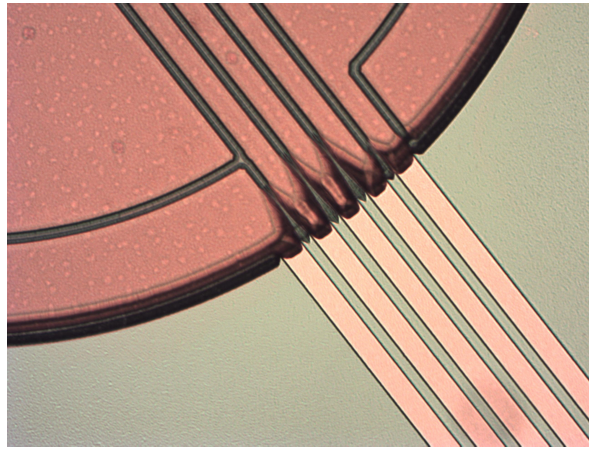


Figure 3.9: Uneven etching of the sacrificial oxide around the contact area

The first step in depositing the membrane material, poly-SiC, is to use an LPCVD furnace to deposit layers of poly Silicon Carbide. This is done in furnace  $F_3$ . Because of the large height of the membranes, the first deposition is a layer of  $2000\text{nm}$ . The recipe used for this is **SIC\_DOPE**, using 123 sccm  $\text{SiH}_2\text{Cl}_2$  and 377 sccm  $\text{C}_2\text{H}_2$  5% in  $\text{H}_2$ , without dopant. The growth rate is around  $11.1\text{nm}/\text{min}$ . After this deposition, the thickness is checked with the Woollam ellipsometer.

The next step is to create release holes to remove the sacrificial oxide. Ideally, these release holes should be as small as possible. This will allow for easy sealing later on. However, the width of the holes determines how much material should be deposited until the holes are sealed. Therefore, the thickness of the new layer should be at least twice the thickness compared to the width of the hole [56].

The first attempt to create holes was to use a  $12\mu\text{m}$  layer of MicroChemicals 10XT-20PL10 photoresist. This height ensures that even the high membranes are covered sufficiently. The downside of a thick photoresist layer is that a long exposure time of 300 seconds is necessary to expose the whole layer correctly. Using a long exposure time will reduce details in the layer. Therefore, the holes that are exposed and developed end up too large. Reducing the exposure time was impossible because a layer of photoresist would still be present. The holes are etched using the Trikon Omega 201, using the recipe **sic.3mu** for a duration of 11 : 40. While the holes are present, the result is almost circular holes with a diameter of around  $6\mu\text{m}$ . This approach was used for the first batch of wafers.

Even though the previous method was used, it was not perfect because the large holes required a thick SiC layer to seal the membrane. Therefore, a second batch was produced, and a different approach was taken. First, the membranes were coated with a layer of  $850\text{nm}$  TEOS oxide. This serves as a hard mask during etching. Next, a layer of  $4\mu\text{m}$  AZ ECI3027 photoresist is used instead of the thick photoresist layer. Even though the membranes are much higher, the step coverage is still satisfactory, as visible in Figure 3.10a. In addition to measuring, the step coverage can be confirmed visually under a microscope. Figure 3.11 shows a corner of a square membrane. The photoresist does get thinner when moving to the corner, as indicated by the striped pattern. However, the layer covers the whole corner nonetheless. During etching, the corner must be observed because this is the part covered with the smallest layer. If the step coverage did not suffice, the measured result would look more like Figure 3.10b. The mask is exposed for 40 seconds and developed

using the recipe *Dev – DP2*, which uses a longer development time than the regular developing recipe.

After placing photoresist, the wafers are wet-etched in *BHF* to etch holes in the oxide hard mask. 6 minutes is sufficient to etch through the layer. Next, the wafers are placed inside the *Trikon Omega 201*, and the same recipe as mentioned before is used. Because of the more precise holes in the photoresist layer and hard mask, the eventual holes are significantly smaller than in the previous attempt. In this case, the holes have a maximum width of  $3\mu\text{m}$ .

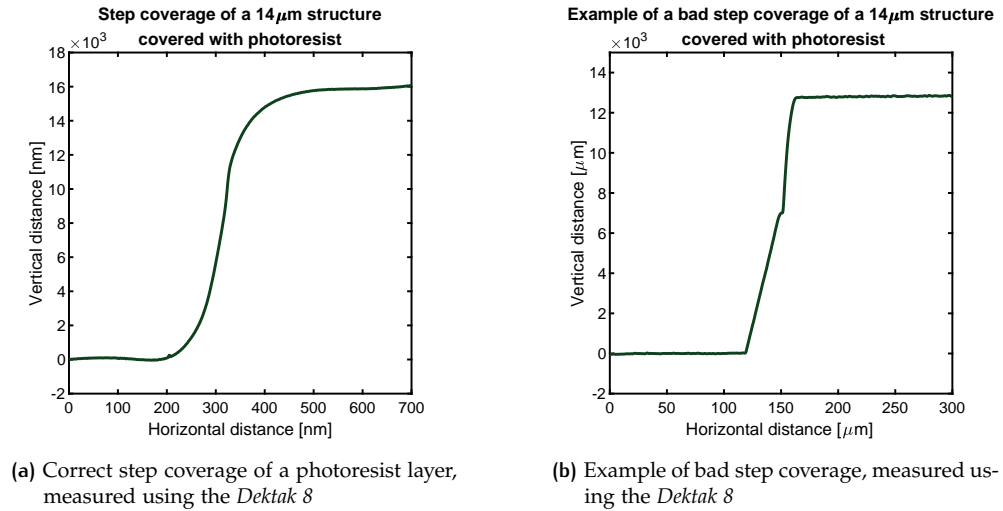


Figure 3.10: Step coverage of a photoresist layer at the edge of a  $14\mu\text{m}$  square membrane

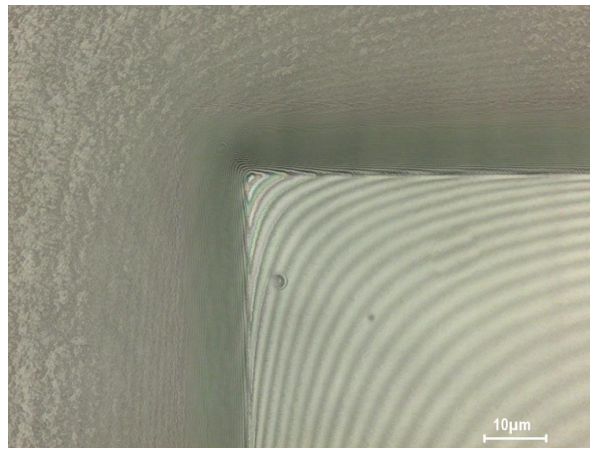


Figure 3.11: Visual confirmation of the step coverage using the *Keyence VK-X250*

In both cases, the photoresist layer on top of the wafer is stripped using the *Tepla Plasma 300*, and the wafers are cleaned. The silicon oxide is left on the wafers, as this layer is removed at the next step.

### 3.3.9 Removing of the sacrificial structures

With the holes in the membranes, the sacrificial structures inside of the membranes can be released. This is done using the *HF Vapor Etcher Primaxx uEtch HF SPTS*. This machine uses an HF gas to etch layers like silicon oxide. Because gas is used, no stresses are applied to the membrane. In addition, the inside of the membrane will not get any humidity inside, unlike when using wet etching.



The wafers are placed inside the Vapor HF machine, and **Recipe 5** is used. This recipe has the highest gas flow of HF and, therefore, the highest etch rate. Because the oxide is annealed, etching the membranes takes a long time. The 10 minute during recipe is repeated 20 times before the membranes are fully released. The result of removing the oxide after 100 minutes of etching is shown in [Figure 3.12](#). After the process is fully finished, the membranes are free to move. The membranes can be moved using a small needle to see if the whole membrane is released correctly. This is shown in [Figure 3.13](#)

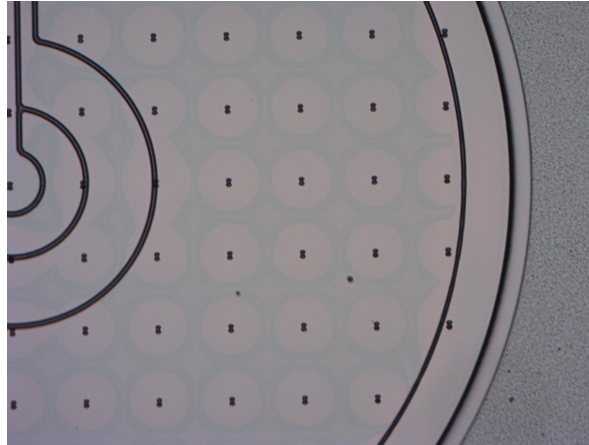


Figure 3.12: The result of etching the sacrificial layer halfway during the process

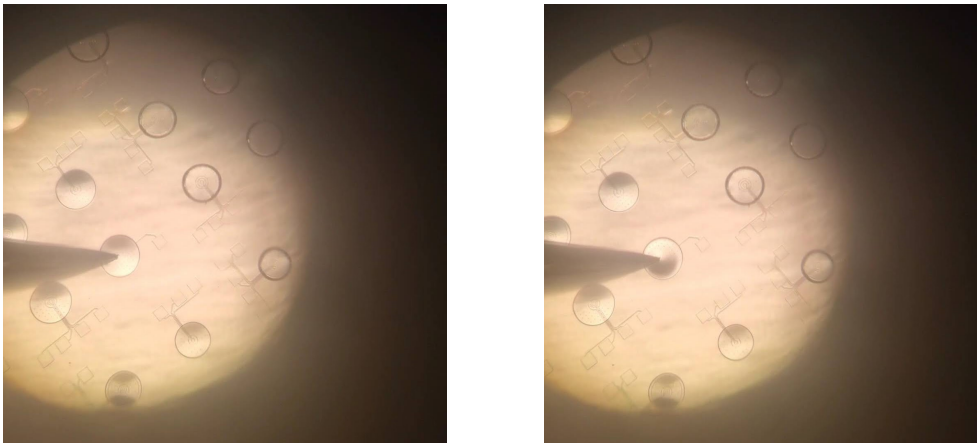


Figure 3.13: Carefully pressing on a released membrane to see if it is released correctly

#### 3.3.10 Construction of the thick SiC membrane

After the membranes are released fully, the wafers are placed back into the LPCVD furnace to increase the Silicon Carbide layer. Not only does this strengthen the membrane for the pressures it has to handle, but it also seals the openings that were made before. Furnace *F3* is used again to deposit the remaining layer. A thickness of at least 2 times the width of the holes is necessary to seal the holes fully [56]. For the batch with big release holes, it means that a layer of  $8\mu\text{m}$  is necessary. For the second batch with smaller release holes, a layer of  $5\mu\text{m}$  suffices. This means that the total membrane thickness is thicker than the simulated  $5\mu\text{m}$ . The result is that the membranes will be stiffer

and move less under pressure. A bigger membrane design can be chosen to compensate for the additional stiffness. For the deposition of the SiC, the same recipe is used as the recipe for the first layer.

The electron microscope is used to verify if the holes are indeed closed. The extremely high resolution of this type of microscope helps to increase the certainty that all holes are truly closed. For example, Figure 3.14 shows one of the holes that is sealed properly.

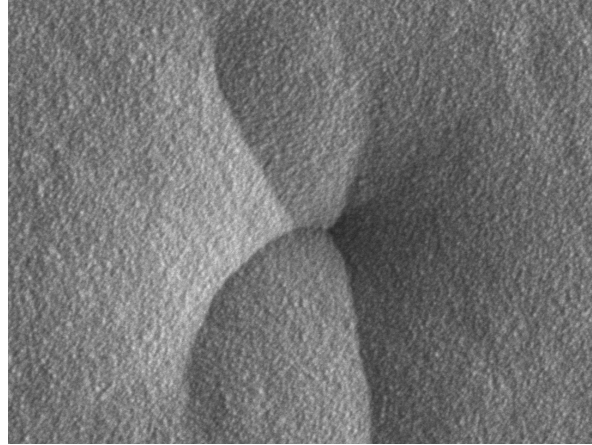


Figure 3.14: An image of a sealed release hole, taken by the electron microscope

In the flowchart, the SiC layer was supposed to be removed where there is no sensor nearby. This step is omitted from the process. Because of a lack of a passivation layer, the silicon carbide can protect the metal.

### 3.3.11 Construction of via's to contact bottom-contacts

Even though the removal of the Silicon Carbide is skipped, the bottom contact metals have to be uncovered again. Because the *Novellus Concept 1* was not operational during the execution of this step, using a Silicon Oxide hard mask was not possible. As an alternative, the wafers are repeatedly coated with a photoresist layer, followed by an etching step. Afterwards, the remains of the photoresist are cleaned, and the process is repeated. Because only a limited layer of Silicon Carbide can be etched before the photoresist layer seizes to have a correct step coverage, this process has to be repeated 13 times. During etching, conductivity measurements are performed to determine if the bottom contacts are fully uncovered. During this repetitive process of etching deep holes with high structures near the holes, imperfections appeared. These imperfections increased every cycle until many of the via holes eventually had an uneven surface. Examples of these imperfections can be seen in Figure 3.15. The reason for these imperfections is that not all photoresist can be washed away properly because some of it hardens after etching. Therefore, during the next etch, a part of the hole stays protected from etching and an uneven pattern forms.

During the production of the second batch, the *Novellus Concept 1* was available. A  $3\mu\text{m}$  layer of silicon oxide is placed as a hard mask. On top of that, a  $4\mu\text{m}$  layer of photoresist is used to pattern the hard mask. Mask 6 is used for this pattern. After exposing and developing the photoresist, the wafers are placed inside BHF for 10 minutes. This etches  $2\mu\text{m}$  of the oxide. Finally, the last  $1\mu\text{m}$  oxide is etched using the *Drytek Triode 384T*. Using dry etching for this last part ensures that the via holes are not too large due to the isotropic nature of wet etching.

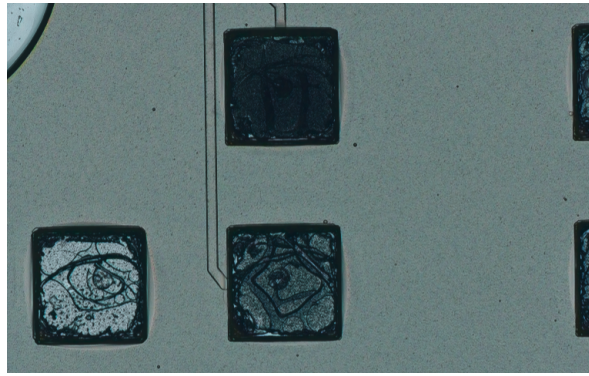


Figure 3.15: Irregularities of the via holes due to hardened photoresist

With the hard mask in place, the wafers can be placed in the *Trikon Omega 201*. The recipe **Mo\_50nm** is used repeatedly until the contacts are uncovered. When the contacts are uncovered, the hard mask is removed in the *Drytek Triode 384T*.

### 3.3.12 Creation of overlay layer

The last steps are to create an overlay material that can be used to create wire-bonded connections. The material used is a chromium layer followed by a layer of gold. After depositing these materials, the wafers are highly contaminated because chromium and gold are red metals. Therefore, further processing after deposition is limited. The process of covering with this overlay material is a lift-off process. This means that a layer of photoresist is placed first. Afterwards, the overlay material is deposited on the surface of the whole wafer. Finally, the photoresist is dissolved in an ultrasonic bath of **1-methyl-2-pyrrolidone (NMP)**. The overlay material on top of the photoresist is pulled off with the photoresist. The overlay material, therefore, only stays in the places where no photoresist was present.

The process starts with a manual coating of NLOF photoresist 2020. This coating should be thick enough to encompass the high structures. As seen before, a layer of  $4\mu\text{m}$  photoresist sufficiently covers the tall structures. Because this height is not available using this type of photoresist,  $3.5\mu\text{m}$  is used. Even if the step coverage is imperfect after coating, this layer will still suffice. The reason is that the top surfaces of the membranes should be covered with overlay material. Therefore, during development, the photoresist layer is removed from the surfaces on top of the membranes. After the layer is exposed and developed, the overlay can be added.

The deposition of the overlay layer is done in the *CHA Solution PLC-S7*. First, a layer of  $15\text{nm}$  chromium is deposited, followed by a layer of  $150\text{nm}$  of gold.

At this stage, the wafers are fully coated with a layer of gold. To remove the layer at the correct places, an ultrasonic bath with **NMP** is prepared. The bath is heated to  $70^\circ\text{C}$ . After waiting for at least 10 minutes, the photoresist layer is dissolved, and the gold layer has also been pulled off. Finally, the wafers are washed with **IPA** and deionised water.

After a visual inspection, the production process is completed. An image of one of the completed wafers is shown in [Figure 3.16](#). In this image, some imperfections are visible that occur in the overlay layer. The flaws are the triangle-shaped gold streaks. The reason for forming is that a few membranes broke during the process. When covering the wafer with the NLOF photoresist, a part of the photoresist got

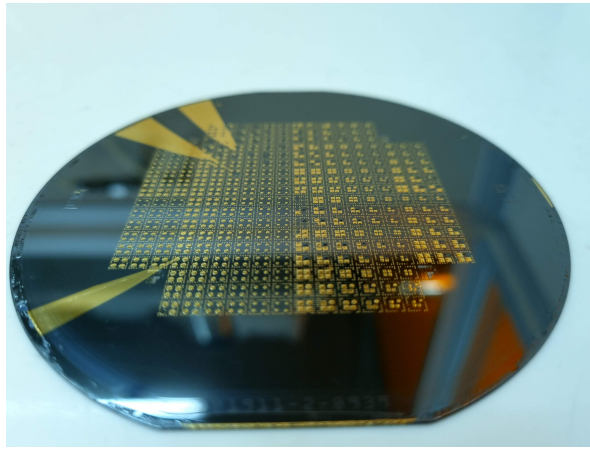


Figure 3.16: The resulting wafer after processing is finished

stuck in the broken membranes, limiting the spread of the photoresist. When the wafer started spinning, these areas were not covered correctly. Even though this gold streak breaks a few sensors, most of the membranes are not influenced by the stripe.

### 3.4 POSTPROCESSING THE WAFERS

Even though the production process of the wafers is completed, the sensors cannot be used yet. Therefore, a few extra steps are necessary to prepare for different measurement techniques. The first measurements at ambient pressure can be done on a wafer scale, so no postprocessing is required. Next, however, the wafer must be cut into dies for measurements from a vacuum to ambient pressure. Finally, to measure ambient pressure to  $1\text{MPa}$ , the dies need to be wire-bonded and placed into a package.

#### 3.4.1 Wafer dicing

Wafer dicing is done using a specialised machine that utilises a thin circular saw to make cuts around the dies. As a first step, the wafer is placed on an adhesive foil. This ensures that the dies stay in place even after the wafer has been cut in pieces. Each die in this design consists of four sensors. The die is  $3000\mu\text{m}$  or  $3\text{mm}$  in width and height, with a small space around it for extra margin. The total pitch of the dies is equal to  $3325\mu\text{m}$ . The dicer is configured using this pitch and aligned to the features on the wafer. Afterwards, the machine saws through the wafer slice by slice. Figure 3.17 shows the machine in the process of cutting through the substrate.

#### 3.4.2 Wire-bonding

After the wafer has been divided into dies, the most promising dies can be wire-bonded. This process involves glueing a die on an electrical housing. Then gold wires are connected from the bond pads on the die to the connection points on the electrical housing. Once the die is wire bonded in the housing, the sensors can be verified at the PCB level. Unfortunately, a problem with the overlay layer became clear during wire bonding. The metals of the overlay do not stick to the silicon carbide sufficiently. The reason is unknown as of yet, because the chromium-gold layer should have no problem adhering to the silicon carbide, and the wafers have been properly cleaned before depositing the metals. This means that the wire-



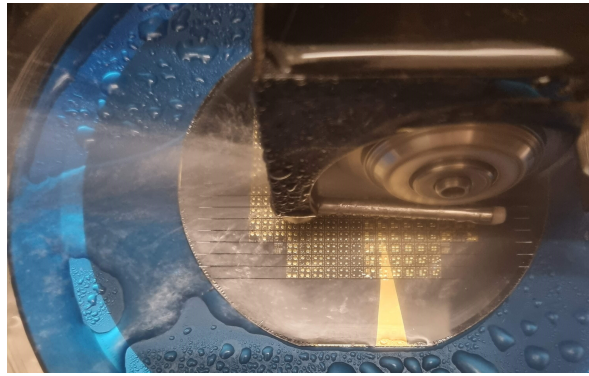


Figure 3.17: Dicing machine in the process of cutting through the substrate

bonding failed most of the time. Very rarely a wire connected properly. Nothing can be done about this problem anymore because it would mean that the whole process would have to be restarted again. Therefore, as a quick alternative, soldering the pads is attempted. Soldering a pad of  $0.2 \times 0.2\text{mm}$  is hard, so the results are not perfect. But a few working samples have been produced. Figure 3.18 shows a die that is both wire-bonded and soldered.

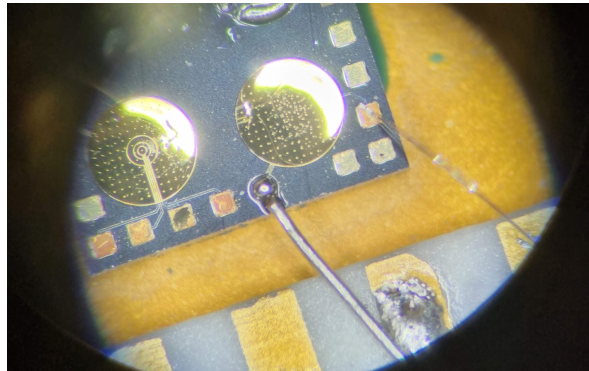
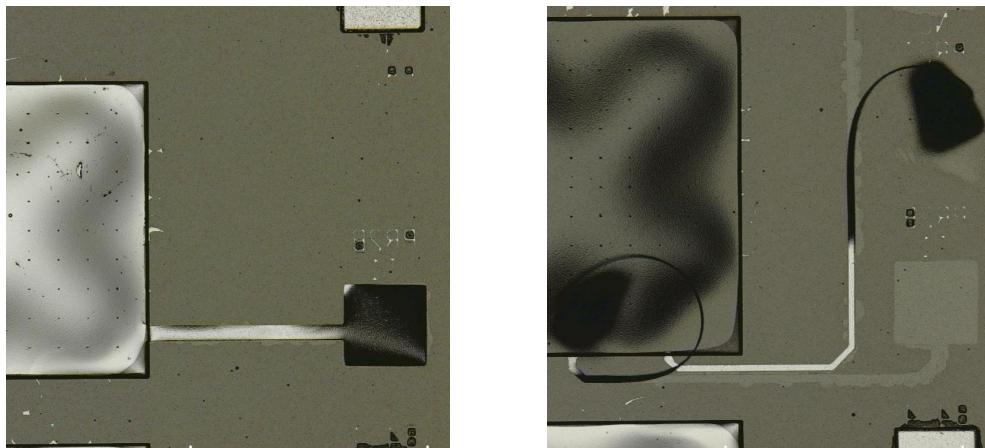


Figure 3.18: Two connections to the die, a soldering connection on the left side and a wire-bonded connection on the right side

#### ***Adding aluminium overlay for better adhesion***

Because all wafers had been produced before the adhesion problem became apparent, the process could not be adjusted anymore. An attempt has been made to promote the adhesion of the metal layers. On top of the gold overlay, a layer of aluminium-silicon is added. This layer of  $200\text{nm}$  thick is deposited with the *Trikon Sigma 204*. Afterwards, a photoresist coating of  $4\mu\text{m}$  positive photoresist is added and patterned with the overlay mask. Afterwards, the aluminium is removed using wet-etching with a phosphoric acid-based chemical with high selectivity for aluminium. Finally, the photoresist is removed using acetone and IPA. Unfortunately, this attempt was unsuccessful because after the photoresist was removed, many of the contacts loosened from underneath the SiC layer. Figure 3.19 shows two examples of the delamination of the contacts. Surprisingly, the contact material that was placed over the irregular vias, as shown in Figure 3.15 has better adhesion than the chromium-gold layer that is placed directly on top of the SiC layer. The wafer has been cleaned properly before applying the metal overlay layer.



**Figure 3.19:** Delamination of contacts after aluminium-silicon was deposited on top of the chromium-gold layer

# 4

## CHARACTERISATION SETUPS

The production of the sensors has finished. In total, 5 wafers have been produced in two distinct batches. The sensors on these wafers have to be tested because, during production, testing is impossible. Realistically, not all sensors will behave as intended, but since many sensors are on one wafer, the chance of success increases. This chapter will walk through the setups used to characterise the sensors. There are three setups used to get all readings. The first two are done inside the measurement lab of the [EKL](#). In this lab, temperatures up to 600°C can be measured, and pressures from vacuum up to ambient pressure. The third setup uses a custom PCB to measure pressures higher than ambient pressures.

### 4.1 CHARACTERISATION SETUPS INSIDE EKL LAB

The measurement lab of the [EKL](#) provides multiple options for characterising the produced sensors. A few different setups are used to determine a part of the characterisation. The first setup used inside the measurement room is a probe station. This probe station measures the capacitance of sensors at ambient pressure and temperatures from room temperature to 200°C. The second set-up is with a micro-station that measures individual dies. The pressure range of this micro-station is from vacuum to ambient pressure, and the temperature range is room temperature to 600°C.

#### 4.1.1 Atmospheric pressure with probestation

The first set-up is a full-wafer measurement system. The wafer is loaded into the Cascade 33 probe station. The probe station is controlled using a computer. The sensors' pads are carefully connected to a precision LCR meter using the probe station's needles. An image of the needle connection is shown in [Figure 4.1](#).

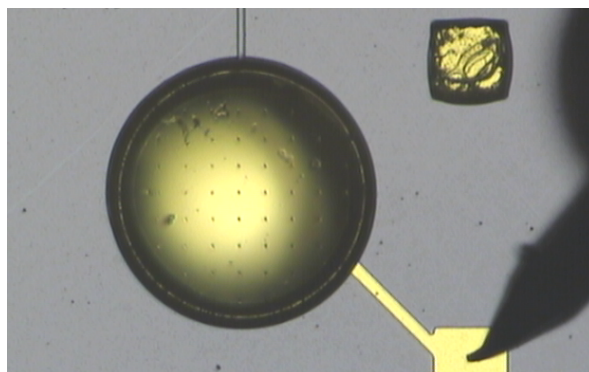


Figure 4.1: Probe station connection with a sensor using one of the needles

The precision LCR meter, the *HP 4284A*, uses a 4-point setup for accurate measurements. Two wires generate a current through the [Device Under Test \(DUT\)](#), and the other two measure the voltage drop over the device. This eliminates the

measurements of stray impedances in the setup. A computer can access the measurement data and save the measured values.

In addition to the LCR meter, the chuck of the Cascade 33 probe station can also be heated. This is controlled via the computer, and a temperature of up to 200°C can be reached using this setup. This measurement setup is illustrated in [Figure 4.2](#).

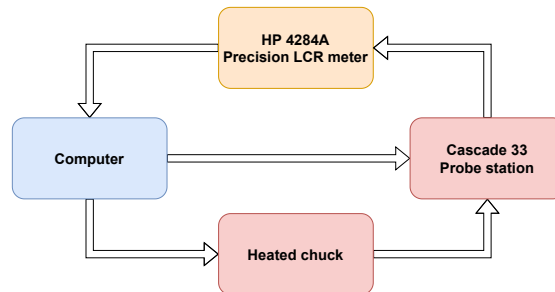


Figure 4.2: Measurement setup of Cascade 33 probe station

#### 4.1.2 Vacuum to atmospheric pressure with vacuum probe station

The second setup in the measurement lab uses a Nextron vacuum probe station. This small device accepts a single die. Using the manual placement of needles, connections can be made to outside the station. A connected die can be seen in [Figure 4.3](#).

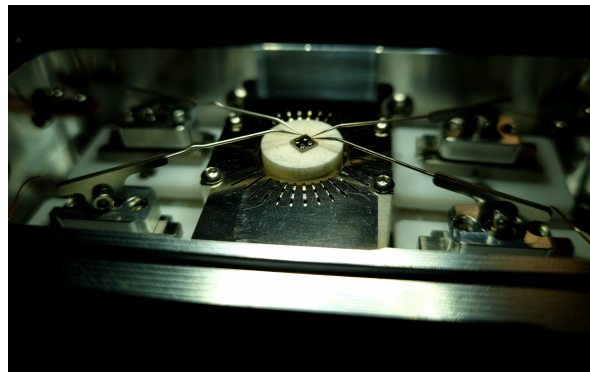


Figure 4.3: Probe station connection with a die using the Nextron vacuum probe station

Again, the probe station is connected to the precision LCR meter. Because this setup requires a 4-point measurement as well, two needles are placed per connection pad. This probe also allows for increased temperatures. This time, the temperature can reach the required 600°C. The temperature can be controlled using a computer. In addition to elevated temperature, the system can also be pulled in a vacuum. the vacuum level used for measurements is  $4.65\text{mPa}$ , which is well below the required  $80\text{Pa}$ . However, the vacuum pump cannot be controlled using a computer. It can only pull a full vacuum or be released at atmospheric pressure. Therefore, dynamic measurements were done while the system was pulling a vacuum. The whole setup is shown in [Figure 4.4](#).

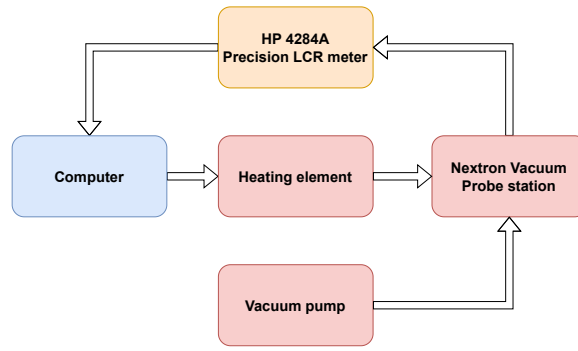


Figure 4.4: Measurement setup of Nextron Vacuum probe station

## 4.2 CHARACTERISATION SETUP FOR ELEVATED PRESSURES

There are several measuring methods available in EKL. The Nextron probe station covers the pressure range from vacuum to atmospheric pressure. In addition, elevated temperatures can be measured using the same setup. However, the high-pressure range from atmospheric pressure to  $1\text{MPa}$  cannot be measured inside the laboratory. Therefore, a different solution must be found to get the required measurements. The first idea is to use PVC drain pipes and a bicycle pump to get the required pressure. However, this setup is not capable of handling high pressures. The next set-up uses a paint pressure system. This system can handle pressures up to  $80\text{PSI}$ , which is equal to  $0.5\text{MPa}$ . While it does not cover the whole measurement range, this system was chosen to conduct the measurements because a solution that handles higher pressures was unavailable.

The next section describes the production of the PCB, but for the sake of a complete measurement setup, a description is made using the finalised PCB. As mentioned, the pressure chamber comprises a paint pressure system. Specifically, the *Airpress Heavy-duty 2½-Gallon PAINT TANK* is used. As a method to pressurise the system, a bicycle pump is used that can reach  $1\text{MPa}$  of pressure, along with a mini-air compressor to reach higher pressures.

The PCB is placed inside the paint pressure chamber. The PCB is battery-powered. However, the battery of the PCB is connected from outside of the pressure chamber. Conducting parts of the chamber are used to pass along the power to the inside. The reason for placing the battery outside the chamber is as a safety precaution. Even though there is no maximum operating pressure on the datasheet of the battery, large pressure differences between the internals of the battery versus the ambient pressure might cause dangerous situations.

A commercial pressure sensor by EPCOS is added on a die to get a reference pressure reading. This C32 industrial pressure sensor is based on piezoresistive readout and uses a Wheatstone bridge to create a readable voltage signal. This sensor is added to two pins on the PCB that can read analogue voltages.

The total setup is shown in Figure 4.5

## 4.3 CUSTOM MEASUREMENT PCB

To use this setup, however, the measurements must be self-contained. Once the system is under pressure, there can be no wires from inside the setup to the outside. Therefore, a system has to be designed to power the sensor and take measurements simultaneously.

All software and hardware designs have been published to a GitHub repository. This depository can be found in <https://github.com/tomsalden/PCAPo4>

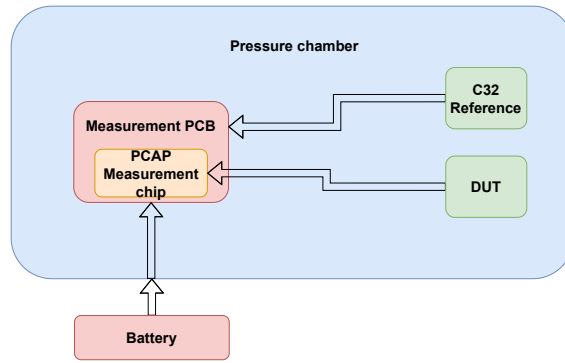


Figure 4.5: The setup for pressure measurements using the custom PCB

#### 4.3.1 Measurement board list of requirements

The system to be designed has a few requirements that should be covered before the system can fulfil its function. First, there are requirements for the capacitance measurement.

##### Measurements

- A measurement resolution of smaller than  $0.1fF$
- Ability to measure 13 capacitances at the same time or in sequence
- Ability to measure two piezoresistive sensors for reference

##### Data processing

- Data should be captured automatically
- Data should be saved and retrieved afterwards

##### System functionalities

- Battery powered including battery protection
- Temperature sensor to keep track of system temperature
- Power light indicator
- RGB light indicator for predefined situations
- Button for predefined actions

Due to the nature of this system, a [Printed Circuit Board \(PCB\)](#) is chosen as a solution. On this [PCB](#), the corresponding circuitry can be added to fulfil the requirements.

#### 4.3.2 Component decisions

For this [PCB](#), specific components are chosen that can achieve the requirements. The component decisions and the reasoning are explained below:

##### Measurements

This PCB should measure 13 capacitances in quick succession with a resolution of  $0.1fF$  or better. The reason for this resolution is the sensitivity of the sensor. From the simulation models, the sensitivity of the sensors is at worst  $0.13fF/100Pa$ , as stated in [Table 2.5](#). From the sensor's specifications, the lowest capacitance that should be measured is  $80Pa$ . Since this should be measured, the sensor's sensitivity can be rewritten as  $0.10fF/80Pa$ , and thus the measurement should have a resolution of  $0.1fF$  or better. Different [CDC](#) chips are evaluated for consistent measurements. The specifications of the selected [CDC](#) chips are shown in [Table 4.1](#).



Table 4.1: An overview of the most promising CDC chips

Name	Bits	Resolution [fF]	Accuracy [fF]	Channels	Notes and datasheet
AD7745	24	0.004	4	2	- [79]
FDC1004	16	0.5	6	4	- [80]
AD7150	12	1	-	2	- [81]
FDC2x1x	28	0.9	-	4	- [82]
PCAP04	20	0.008	-	6	Compared to one reference [83]
AD7147	16	0.122	-	13	Touch screen sensor [84]
AD7142	16	0.031	-	13	Touch screen sensor [85]

When comparing the different options by their resolution, the FDC1004, AD7150, FDC2x1x and ADD7147 cannot reach the specified  $0.1\text{fF}$ , so they are unsuited for this system. The AD7142 specialises in touch-screen applications, and the datasheet does not show if it can read out a sensor precisely. Therefore this option is also not considered. Finally, because of the current stock and the comparatively few channels, the AD7745 is also not used. Because the PCAP04 has six channels that the same internal reference capacitance evaluates, and it has a resolution that is better than the requirements, this chip is chosen. With six individual channels per CDC, the pressure sensor contacts can be divided among three CDC chips. It is beneficial for precision if one CDC reads all contacts from one sensor. A division as made in Figure 4.6 allows for this. Each top contact is considered ground, and the bottom contacts are labelled C1-1 to C5-5. Capacitance is measured between the ground and one of the labelled contacts.

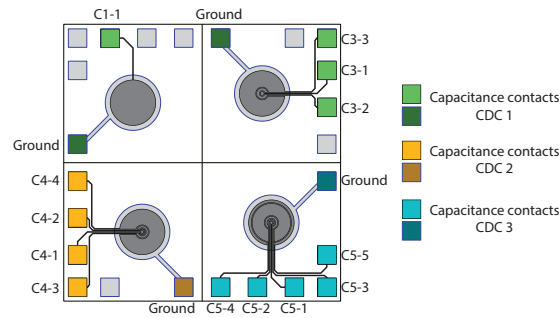


Figure 4.6: The distribution of different contacts to three six-channel CDC chips

The operation principle of this CDC is that it charges the capacitance connected to the output port to  $V_{DD}$ . After a charging time and a full-charge time, the chip connects the capacitance to the ground via a resistor. This causes the capacitor to discharge back to  $0\text{V}$ . The time it takes to discharge a capacitor depends on the circuit's time constant. This constant is defined by the capacitance and resistance in a circuit like shown in Equation 4.1.

$$\tau = RC \quad (4.1)$$

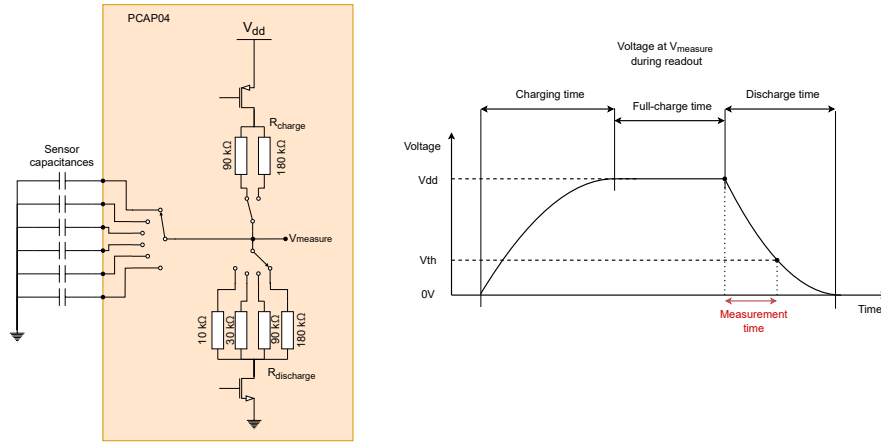


Figure 4.7: The working principle of the PCAP04 CDC chips

This time constant signifies the time it takes for a capacitor to discharge to 63% of its charge. A higher resistor or capacitor value increases this time. Therefore, if the resistor value and the time constant are known, the capacitance can be calculated. This CDC works using this principle. From the moment the discharge is engaged, a timer starts. This timer continues counting until a certain threshold voltage is reached. The time constant can be calculated from the time passed until the threshold is reached. With a known discharge resistor, the capacitance is calculated. In addition, a known internal capacitor can be used as a reference for measurements. The working principle is displayed using a diagram in Figure 4.7. The sensors are connected to the input of the chip. The chip then sequentially selects each sensor. Once connected, the PCAP04 charges the capacitance to  $V_{DD}$ , which is 3.3V. A resistor,  $R_{charge}$  is added in series to limit the charge rate. This resistor can be selected to either 90kΩ or 180kΩ. Once the capacitor is fully charged, the chip discharges the capacitor using the selected discharge resistor  $R_{discharge}$ . This resistor can be: 10kΩ, 30kΩ, 90kΩ or 180kΩ [83].

### Data processing

The chosen chips should be operated correctly so the data can be read. In addition, the data should be processed and saved for evaluation after the experiment. For flexibility reasons, a microcontroller is used that can be programmed using the Arduino environment. Because of its WiFi implementation, which makes it easier to access the chip during the experiment, the ESP32 is chosen as a chip. Finally, because of its many GPIO pins and the current availability, the ESP32-WROOM-32 Devkit V1 is used as the brain of the system [86].

In addition to the WiFi connection where the data can be visualised, an SD-card slot will be added to save the measurements on an SD card. This will be connected to the ESP32 microcontroller.

### System functionalities

Finally, for system functionalities, the PCB should be battery-powered, including battery protection. For a battery, Lithium Ion technology was advised. This type of battery needs protection from over-voltage, under-voltage, short circuits and too-high temperatures. To ensure the battery stays within the limits of the datasheet, a Li-Ion battery charge and protection circuit is added based on the HW-775 chip[87]. This will allow safe charging of the battery without surpassing the maximum voltage and ensure the battery is not drained below the minimum voltage. In addition, it disconnects the battery in case of a short circuit, and it disconnects the battery if the temperature reaches more than 45°C while charging and 60°C while discharging.

An MCP9701 is included in the design to keep track of the PCB's temperature while the measurements are active. This thermistor can measure temperatures up



to 125°C [88]. Finally, generic buttons and a red LED are used for the buttons and power light. A WS2812 LED is used as an indication LED since it can display all colours and requires only one data connection.

#### 4.3.3 Design of the schematic

After choosing the main components, the schematic can be constructed. Detailed images of the schematics are shown in [Appendix A](#). The first part of the schematic is the power design. This design can be seen in [Figure A.1](#). First of all, the battery connections are made, connector J1. This battery is then connected to the Li-Ion battery charge and protection circuit, shown as J6 in the schematic. An additional connector is included to be able to charge the battery without taking it out. This is connector J7. Finally, a buck converter is added because the PCAPo4 chips and ESP32 devices work on 3.3V. The AMS1117-3.3 is used because it can handle a large current of 1A and the implementation is straightforward. An output capacitor of 22 $\mu$ F is added as called for in the datasheet.

The next part of the schematic is the implementation of the PCAPo4 chips. The top-level design can be seen in [Figure A.2a](#). In [Figure A.2b](#), the insides of PCAP-IC\_1 to PCAP-IC\_3 are shown. The schematic design follows the datasheet and the design on the PCAP-EVA-BOARD. In addition, a reference capacitance of 2pF with a low tolerance is added to each chip to make sure the measurements are compared to a fixed value.

To control the chips and to process the data they generate, the ESP32-WROOM-32 Devkit is placed in [Figure A.3](#). In addition, IC4 is added as a temperature sensor, and two resistor dividers are included for piezoresistive readout.

To save the data, the SD card holder is placed in [Figure A.4](#). In addition, the power LED is powered directly from the 3.3V line, and the WS2812 LED receives its data from the microcontroller. Two buttons are added for auxiliary functions, and a switch that connects or disconnects the battery is placed as S1.

In addition to these components, some connectors will attach to the pressure sensor. Finally, there are some holes for mounting the PCB on elevated supports. The total overview of the PCB is shown in [Figure A.5](#).

#### 4.3.4 Design of the PCB

The schematics are the base of a PCB. The next step is to design a physical representation of the electrical schematics. Because of a steep increase in price for boards above 100x100mm, this is set to be the size constraint for the PCB. First, the components have to be placed in an orderly fashion. When the placement is finished, the connections defined in the schematics must be manually drawn on the board. Eventually, the board is completed with components on the top and bottom of the PCB. The total size is 85x85mm. The connections, or traces, joining the components have different widths depending on their function. The power traces have a thickness of 1mm, the data communication signals, like I<sup>2</sup>C and SPI, have a thickness of 0.5mm and the other traces have a thickness of 0.25mm. The final board layout is visualized on the 3D renders shown in [Figure 4.8](#)

#### 4.3.5 Software development for the measurement board

With the PCB created, software development for the ESP32 is the next step to control how the system should behave. As mentioned, all software can be found in the GitHub repository, found on <https://github.com/tomsalden/PCAPo4>. A brief overview of the software will be given here.

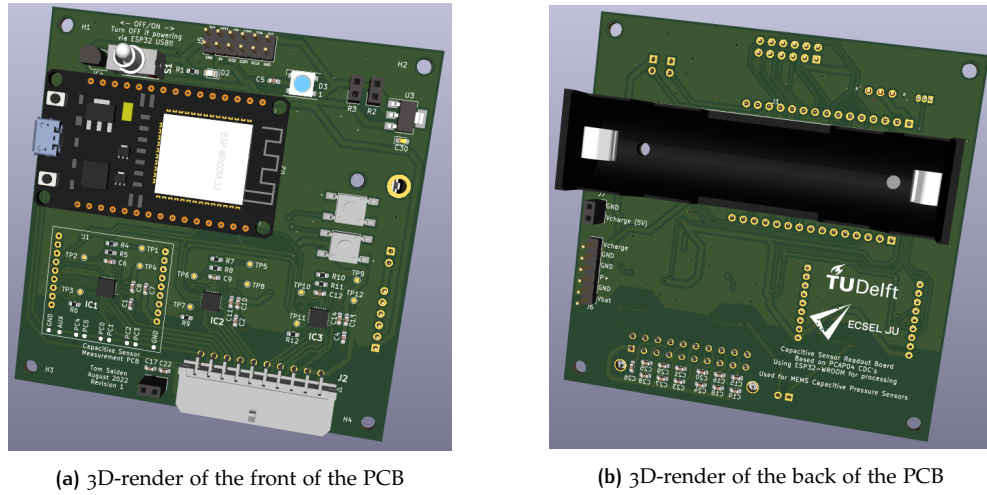


Figure 4.8: PCAPo4 integration schematics

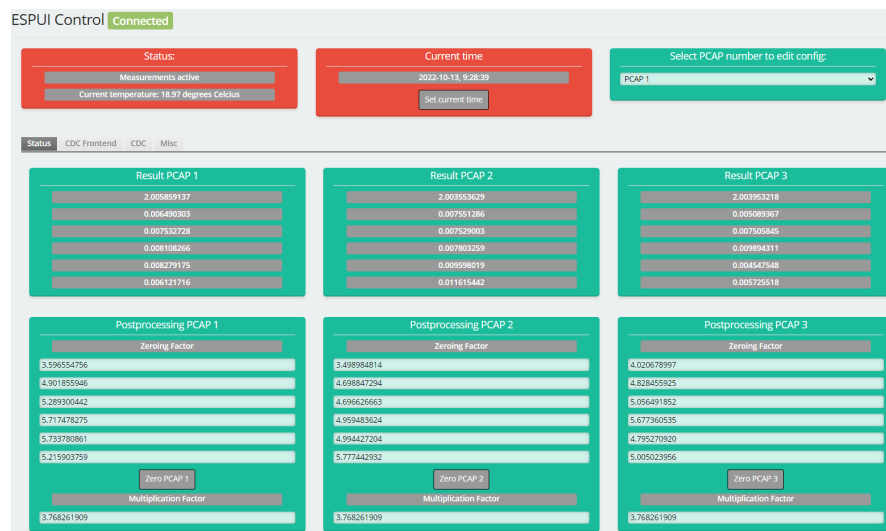


Figure 4.9: The main screen of the webserver hosted by the ESP32 device

The program written is heavily based on an existing library of PCAPo4 chips for Arduino implementation [89]. In addition, the library ESPUI and its required libraries are used to create a web interface [90].

When the PCB is powered on, the ESP32-WROOM-32 immediately starts functioning. At startup, the first task is to connect to an SD card. The microcontroller tries to find configuration files for the network and the PCAPo4 chip settings on this SD card. If they are not present, a new configuration file is created. Next, the ESP32 tries to connect to a WiFi network that is described in the configuration. If there is no configuration, the SSID: "GenericWiFi-SSID" is tried with the password "GenericWiFi-PWD". If there is no network, the ESP32 creates its own network and acts as an access point. The webserver to view and change configurations can now be accessed using the local IP address of the device.

The next step is to try and connect to the PCAPo4 chips and initialize them. When each chip is initialized, the correct configuration is loaded. Afterwards, the webserver updates with the correct configuration values. Then, the ESP32 starts the PCAPo4 chip measurements.

With each new measurement, the updated results are printed on a unique file on the SD card. In addition, the results can be viewed in the serial port and on the webserver.

The main webserver layout screen is shown in [Figure 4.9](#). This main screen shows the measurement status and the temperature measured with the temperature sensor. In addition, the current time can be set, so the ESP32 is synchronized with the connected device. This time is included in the measurements on the SD, so measurements can be referred to using the time they are taken. Finally, an overview of the current measurement values and the offset values are given. There are a few tabs present to adjust the settings of each PCAPo4 chip individually. The settings can be found in the datasheet registers [83].

#### 4.3.6 Validation of the PCB

After the PCB's production and the software is written, the system should be tested and verified. First of all, the different functionalities of the PCB have to be checked. If all functionalities are functioning correctly, the results that the system gives have to be verified. Because the traces on the PCB and wires connecting the PCB will add capacitance to the measurement, a calibration to filter out these additional capacitances will be necessary.

##### *Functionality test*

The first part of the PCB to be tested is the power. Before connecting the ESP32 microcontroller and the PCAPo4 chips, the 5V and 3.3V lines must be checked to see if the correct voltage level is present. Testing both voltages can be done by connecting a power supply with a voltage of 4.2V to the battery terminals. This simulates a full Li-Ion battery. This voltage is first boosted to 5V by the battery charge circuit. Afterwards, this 5V is converted back to 3.3V, which is used by most electronic components on the board.

Next, the input voltage can be swept to higher than 4.2V to test the overvoltage protection of the charge circuit and to lower than 2.8V to test the under-voltage protection. These two voltages are the maximum and minimum voltage a lithium-ion battery should be used at [91]. Finally, the charging capabilities of the system can be tested by applying 5V to the input pins.

After verifying these voltages with a multimeter, the ESP32 and PCAPo4 chips can be placed. First, the indicator LED and SD card holder are tested. The SD card uses the SPI protocol to communicate with the microcontroller. The signals of this protocol are checked with a logic analyzer.

Once these parts have been verified, the PCAPo4 chips are tested with the written software. These chips work using the I<sup>2</sup>C protocol, and the communication channels can also be tested with a logic analyzer. This proved to be successful.

##### *Readout verification*

Finally, the whole system is functional. However, the measurements have to be verified. When a capacitor is connected to each port, the measured value should increase corresponding to the added capacitance. Due to the capacitive characteristics of the traces and wires that connect this capacitor to the measurement chip, the result will not be the exact value of the added capacitor. Therefore, the system has to be calibrated. This is done with a series of known capacitances. Two capacitors are measured with an LCR meter. The difference between the two is noted. Afterwards, the same capacitances are measured with the PCB. A factor must compensate for the mismatch between the two measurements. Afterwards, the offset that the PCB adds to the measurement can be determined by reading the capacitance difference between the LCR and PCB measurements. Finally, the compensated capacitance is calculated using [Equation 4.2](#).

$$C_{\text{compensated}} = C_{\text{measured}} \cdot \text{multiplicationFactor} - \text{offsetFactor} \quad (4.2)$$

After measurements, the multiplication factors for the three PCAP chips are equal to 3.768, The offset factor is slightly different for each input, but on average, it is equal to 4.194. This factor corresponds slightly to the trace length from the chip to the connection. These factors are true for measurements without extra cables. For the eventual setup, a new calibration has to be performed.

# 5

## MEASUREMENTS AND CHARACTERISATION OF SENSORS

The discussed measurement setups will now be used to get readings from the sensors. First, this chapter will review the results collected during the sensors' production. Next, the operation of the sensors is verified, and the results are characterised. Finally, the results will be compared to simulations.

### 5.1 SENSOR PRODUCTION RESULTS

During the production of the sensors, nonidealities were introduced. These nonidealities ended up changing the design parameters. An example is that the release holes turned out too large when fabricated. The result of these larger holes is that the Silicon Carbide layer on top must be thicker to seal the membrane correctly. This decision will change the behaviour of the sensor. In addition, stresses in the different material layers make the membranes balloon and show different buckling modes. The extent of this behaviour was not expected and has not been visualised in simulations.

#### 5.1.1 Produced design values

During the production of the sensors, some choices have been made that differ from the design created in the first place. The result of these differences will show in the results, which will not be the exact values as simulated in previous chapters. A list of the actually produced values is given in [Table 5.1](#).

Table 5.1: The produced wafer parameters

Sensor identifier	Membrane radius/width	Membrane thickness	Gap height
<b>Simulated sensors</b>			
Low-range sensor	470 $\mu m$	5 $\mu m$	8.5 $\mu m$
Mid-range sensor	470 $\mu m$	5 $\mu m$	14 $\mu m$
High-range sensor	400 $\mu m$	5 $\mu m$	8.5 $\mu m$
<b>Production batch 1</b>			
Wafer number 0939	250 $\mu m$ to 500 $\mu m$	10.8 $\mu m$	12.74 $\mu m$ and 6.75 $\mu m$
Wafer number 0941	250 $\mu m$ to 500 $\mu m$	10.8 $\mu m$	12.74 $\mu m$ and 6.75 $\mu m$
<b>Production batch 2</b>			
Wafer number 4091	250 $\mu m$ to 500 $\mu m$	7 $\mu m$	4.641 $\mu m$
Wafer number 4087	250 $\mu m$ to 500 $\mu m$	7 $\mu m$	4.641 $\mu m$
Wafer number 4142	250 $\mu m$ to 500 $\mu m$	7 $\mu m$	4.641 $\mu m$

### 5.1.2 Compressive stress and buckling of membranes

Next to production parameters that have been changed in comparison to the simulated values, the membranes also exhibit more stresses than originally anticipated. During the deposition of the Silicon Carbide layers, a mismatch of thermal expansion between the silicon, silicon carbide, molybdenum and TEOS oxide all contribute to the internal stresses. The stress difference before and after the silicon carbide has been recorded using the *Flexus 2320-S* stress meter. The stress difference between before and after depositing is: These internal stresses can also be seen visually. The compressive stress makes the membranes balloon up, even after sealing. This effect, called buckling, exists in different modes. In addition to ballooning up, some membranes exhibit a folding behaviour. Even though all membranes' production conditions are identical, some membranes balloon up, and some membranes fold in on themselves. The folding behaviour occurs more frequently for small membranes.

The shapes created by buckling are present in literature. Figure 5.1 shows a comparison between a  $\text{Si}_3\text{N}_4$  membrane in the literature compared to a membrane made by this design.

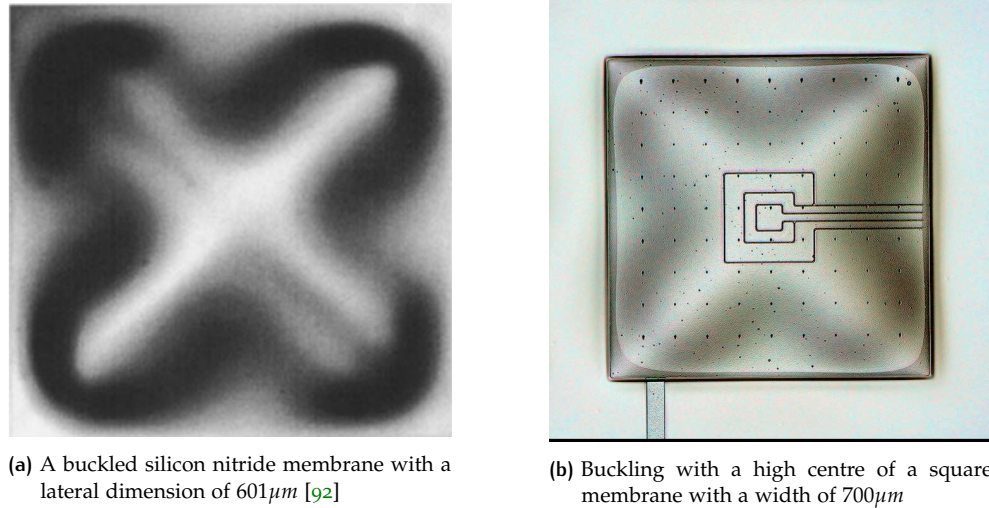


Figure 5.1: Buckling mode in the literature compared to this work

This buckling effect will change the characteristics of the sensors. The base capacitance will be different, to begin with. Especially for devices with the high centre buckling mode, the base capacitance will be lower than originally designed. The extent of this difference depends on how high the centre is due to the buckling effect. Using the Keyence microscope, height profile images have been made to determine the centre height of the membrane compared to the edge. It was found that there is a correlation between buckling height and membrane size. In addition, higher membranes have a different buckling height than lower membranes.

A factor has been found to connect membrane radius to buckling height. When the membrane radius or width is multiplied with this buckling factor, the buckling height is gained. Table 5.2 shows the buckling factor for each situation.

Table 5.2: Buckling factors for each sensor type

Sensor type	Membrane height	Buckling factor
Low membrane	$6.75\mu\text{m}$	0.060
High membrane	$12.74\mu\text{m}$	0.014

Examples of the height differences throughout the membrane are shown in Figure 5.2. Figure 5.2a and Figure 5.2b show the two modes present in circular membranes and Figure 5.2c and Figure 5.2d shows the two modes present in square



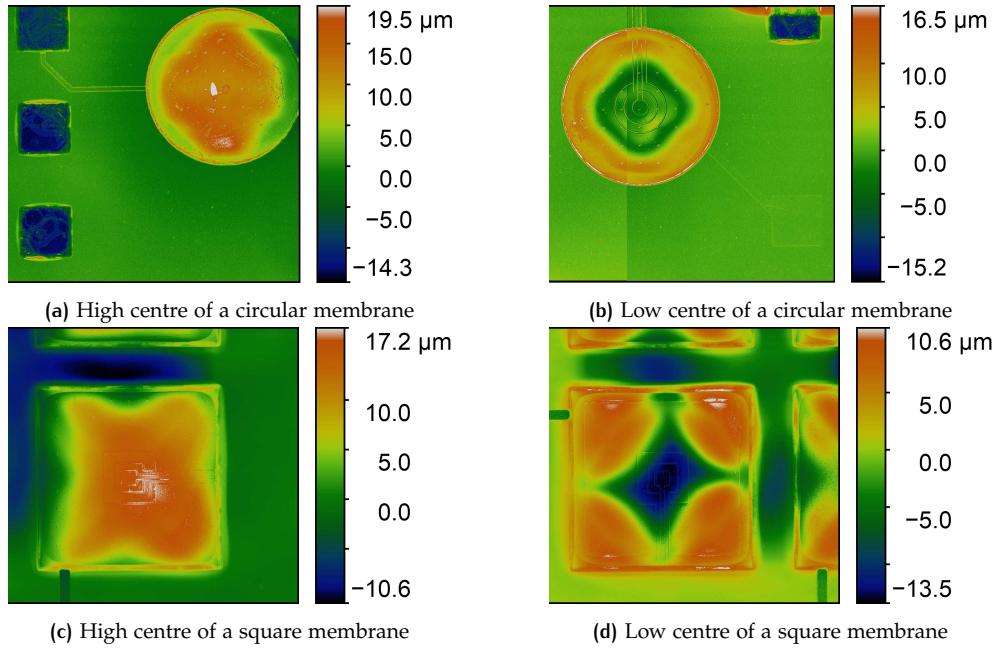


Figure 5.2: Different modes of buckling in produced membranes

membranes. Visible is that either the centre of the membrane bellows up or the centre almost touches the bottom of the cavity.

## 5.2 CHARACTERISATION RESULTS

Using the described setup possibilities, the sensors have been characterised using several different methods. After these characterisations, the effect of changing membrane size is verified for both sensors  $6.75\mu\text{m}$  and  $12.74\mu\text{m}$  high. In addition, the impact of increasing temperature is studied. Finally, the behaviour of the sensors from atmospheric pressure to vacuum is investigated.

### 5.2.1 Atmospheric pressure at room temperature

#### *Circular sensors*

The measurements for circular sensors can be divided into different categories. First, the sensors are divided into sensors with heights of  $6.75\mu\text{m}$  and  $12.74\mu\text{m}$ .

##### **Circular sensors with $6.75\mu\text{m}$ membrane height**

First, the buckling sensors with a low centre are measured in this category. An example of this type of sensor is shown in Figure 5.3. Because the sensors are more rippled than the sensor illustrated in Figure 4.1, the base capacitance is expected to be higher.

Unfortunately, there are not many samples of this buckling sensor type. For instance, there are no data points at radius  $500\mu\text{m}$ . Even though there are not many data points, a clear trend can be seen. As the radius of the sensor increases, the base capacitance also increases. This is expected from simulations and calculations. The results of these measurements can be seen in Figure 5.4

The next measurements are done with buckling membranes with a high centre, like in Figure 4.1. The centre of these membranes is further compared to the previously measured sensors, which lowers the base-capacitance value. Even though this data has some outliers, a general trend of increased capacitance is seen when

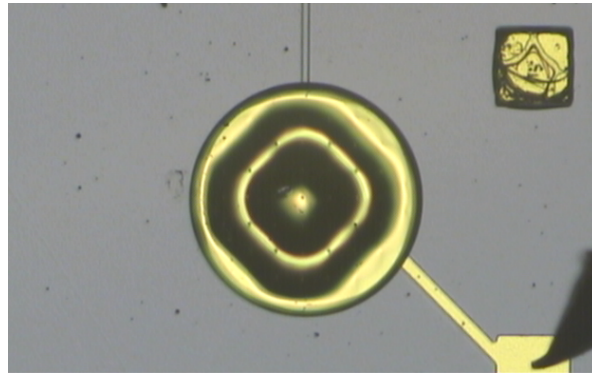


Figure 5.3: Example of a circular buckling sensor with a low centre

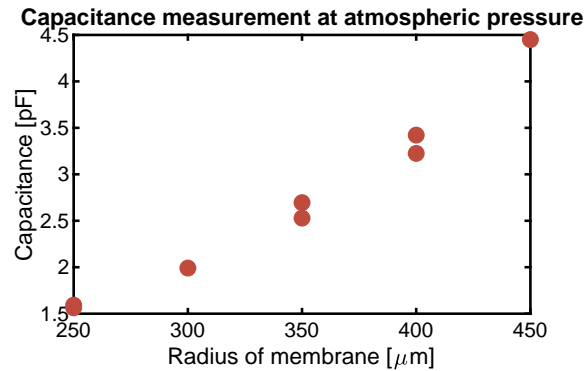


Figure 5.4: Measurements of circular sensors with a buckling membrane, with a membrane height of  $6.75\mu\text{m}$  at room temperature and atmospheric pressure

increasing the membrane radius. The result of these measurements is shown in Figure 5.5.

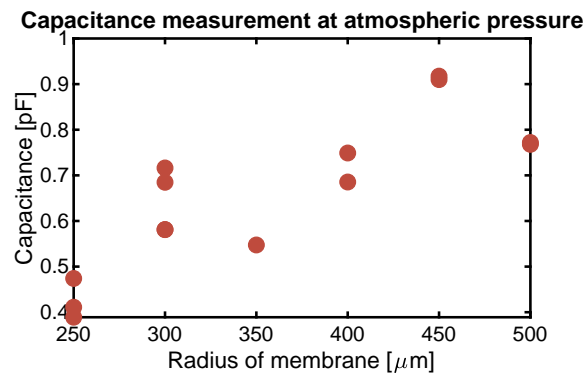


Figure 5.5: Measurements of circular sensors with a membrane height of  $6.75\mu\text{m}$  at room temperature and atmospheric pressure

#### Circular sensors with $12.74\mu\text{m}$ membrane height

Unlike the lower sensors, the high sensors do not feature many buckling membranes with a low centre. Therefore, no measurements could be made of this mode. Only measurements of fully inflated sensors have been made. The result of these measurements are shown in Figure 5.6

#### Square sensors

In addition to the circular sensors, the square sensors also have been evaluated. This sensor has the same two heights that have been measured.



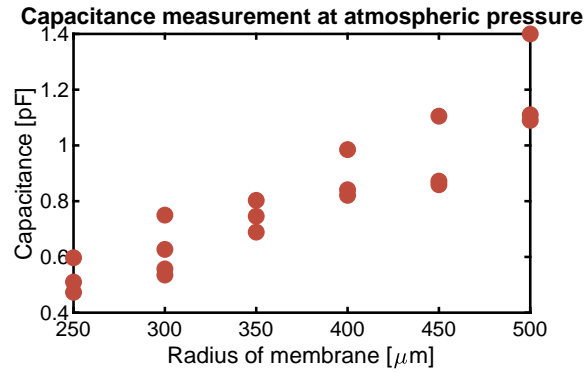


Figure 5.6: Measurements of circular sensors with a membrane height of  $12.74\mu\text{m}$  at room temperature and atmospheric pressure

#### Square sensors with $6.75\mu\text{m}$ membrane height

The low square sensors have the same behaviour as the circular sensors. However, the base capacitances of these sensors are higher than their circular counterpart. The results are shown in [Figure 5.7](#)

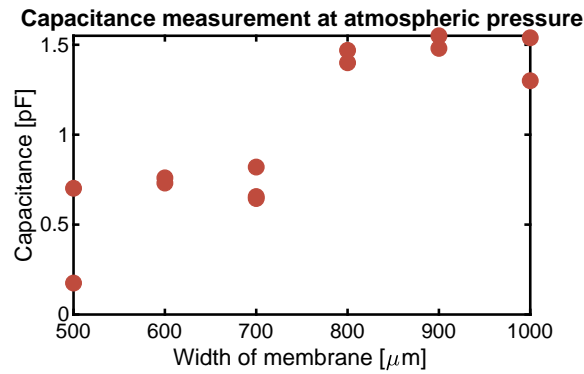


Figure 5.7: Measurements of square sensors with a membrane height of  $6.75\mu\text{m}$  at room temperature and atmospheric pressure

#### Square sensors with $12.74\mu\text{m}$ membrane height

Finally, the high square sensors are measured. Because the higher sensors are more fragile than the lower ones, fewer square sensors survived the production process, resulting in fewer samples than the other measurements. The result of these measurements is shown in [Figure 5.8](#).

#### 5.2.2 Contact division confirmation

During the design of the sensors, a decision was made to suppress the intrinsic nonlinearity of the devices. Part of this decision was to enable the sensors to operate in touch mode, but the other decision was to divide the bottom electrode into a few distinct electrodes. The summation and subtraction of these electrodes can obtain a more linear result. The capacitance per electrode should be evaluated to verify if the contacts will work correctly. If the correct division is found, then the electrodes should be able to make the sensor respond more linearly. [Section 2.6.3](#) shows how the contacts have been designed on the mask. In this section, [Table 2.7](#) gives an overview of the area of each contact.

The measured results deviate somewhat from the designed values. Especially the outer electrode value is bigger than the intended value. A possible reason for this effect is the buckling effect. Due to this effect, the centres of the membranes are further away from the bottom electrode than the edges of the membrane. And

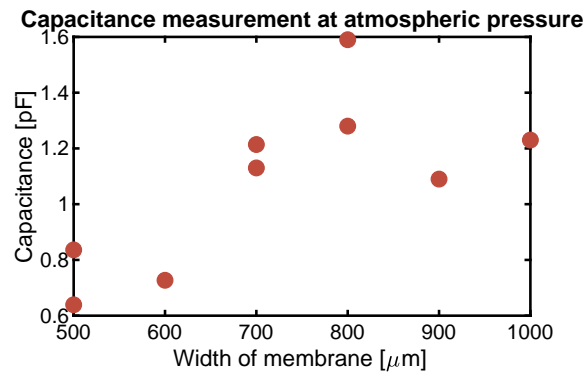


Figure 5.8: Measurements of square sensors with a membrane height of  $12.74\mu\text{m}$  at room temperature and atmospheric pressure

because a bigger distance corresponds to a larger capacitance, a point in the centre has a lower capacitance relative to the edge. A future solution to this is to either design the contact arrangements with a membrane in its buckled state, or to prevent the buckling altogether.

Table 5.3: Designed and measured contact arrangements of bottom electrodes

Contact arrangement	Area contact 1	Area contact 2	Area contact 3	Area contact 4	Area contact 5
1	1	-	-	-	-
3 - designed	0.10	0.15	0.75	-	-
3 - measured	0.08	0.13	0.80	-	-
4 - designed	0.08	0.07	0.12	0.73	-
4 - measured	0.05	0.05	0.12	0.78	-
5 - designed	0.08	0.08	0.12	0.57	0.15
5 - measured	0.05	0.05	0.10	0.43	0.37

### 5.2.3 Atmospheric pressure at elevated temperatures to $200^\circ\text{C}$

The next measurements are a sweep of elevated temperatures at atmospheric pressure. By changing the temperature in selected steps and measuring each sensor at the corresponding temperature, a characteristic of the behaviour due to temperature can be obtained. The expected behaviour of the sensors is that the membrane will expand due to temperature. During previous simulation, this expansion caused the membrane to sink towards the bottom contact, increasing the capacitance as the temperature decreased.

First, the low circular sensors are evaluated. These sensors have a height of  $6.75\mu\text{m}$ . In this case, the membranes are buckled with the centre of the membrane down. The results of varying temperatures are shown in Figure 5.9. Unlike earlier simulations, the capacitance value increases as temperature increases. The reason for this is that at lower temperatures, the membrane moves up rather than down to relieve the thermal stresses it experiences. From the data, the capacitance value has an exponential relation with the temperature.

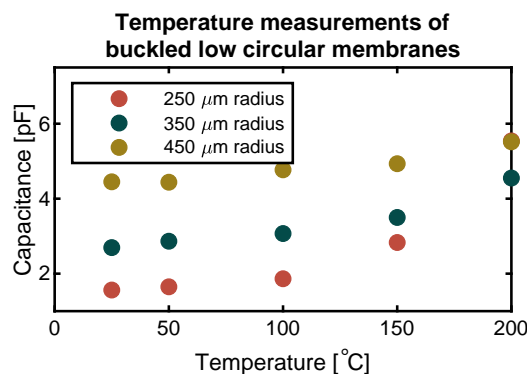


Figure 5.9: Temperature measurements of circular membranes with a height of  $6.75\mu\text{m}$  and a buckled membrane

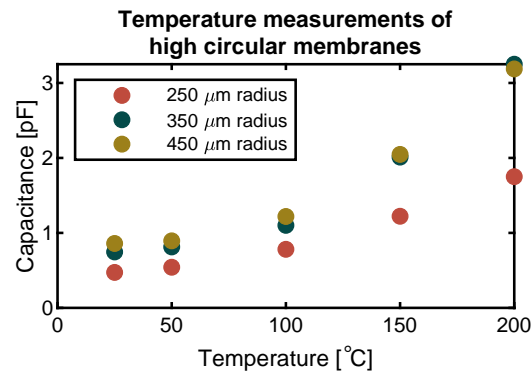


Figure 5.10: Temperature measurements of circular membranes with a height of  $12.74\mu\text{m}$

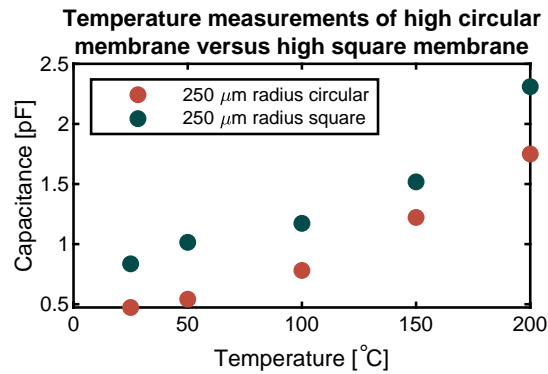


Figure 5.11: Temperature measurements of a circular membrane compared to a square membrane, both with a height of  $12.74\mu\text{m}$

#### 5.2.4 Elevated temperatures up to $600^{\circ}\text{C}$

In addition to an elevated temperature of  $200^{\circ}\text{C}$ , the full temperature range can also be tested. These measurements are done using the Nextron Vacuum probe station, as displayed in Figure 4.4. Even though the same precision LCR meter is used, the base capacitance readings are higher compared to the first set-up. There could be several reasons for these higher capacitance values. The first reason is the measuring method. For accurate capacitance readings, a 4-point measurement setup is used. The Cascade 33 probe station has two probes connected to one needle at a set distance. The Nextron probe station does not have this feature, so to do a proper measurement, two pairs of needles were placed as close to each other as possible. As this is not perfect, a measurement error is possible. The measurement setup is shown in Figure 5.12a.

In addition to this, the precision LCR meter needs to be calibrated. Calibration can be done in the Cascade 33 probe station by lifting the needles and measuring calibrating using open circuit measurements. The Nextron has springloaded needles that drop down as soon as they are released. To calibrate the LCR meter, the two pairs of needles are placed on small parts of the wafer covered with the gold overlay. This way, the two pairs still are electrically connected while the open circuit measurement can be performed. The calibration setup is shown in Figure 5.12b.

The temperature measurements are carried out in steps of  $50^{\circ}\text{C}$  or  $100^{\circ}\text{C}$ . After each measurement, the die is swapped for the next and placed on the probe station for some time to equalise the temperature across the device. Once the capacitance value stabilises, the measurement is taken. The result of the high temperature measurements are visible in Figure 5.13

Just as in the low-temperature tests to  $200^{\circ}\text{C}$ , a rising capacitance is detected when the temperature increases. As mentioned, the capacitance value is much

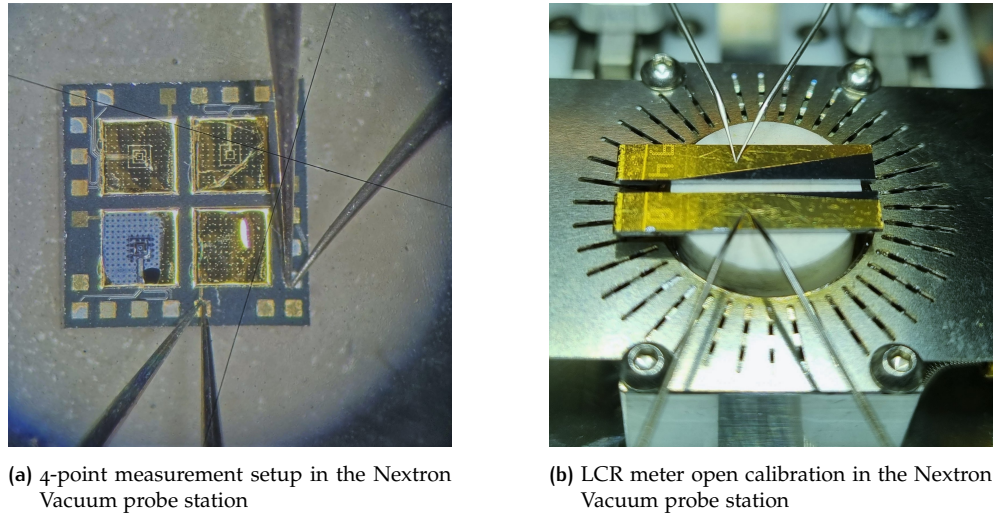


Figure 5.12: Measurement and calibration setup in the Nextron Vacuum probe station

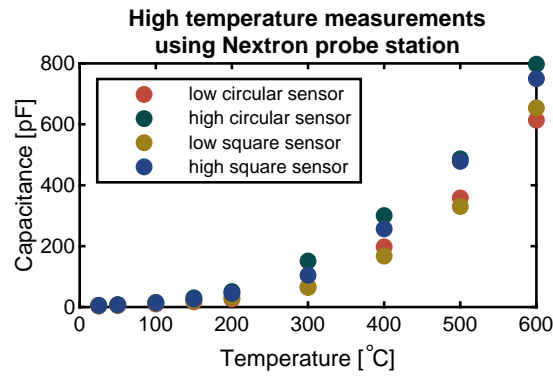


Figure 5.13: High-temperature measurements of circular and square sensors with both  $6.75\mu\text{m}$  and  $12.74\mu\text{m}$  height

higher using this measurement setup compared to the previous setup. The capacitance value at  $200^\circ\text{C}$  with this setup varies between  $26\text{pF}$  and  $50\text{pF}$ , while during the low-temperature measurements, the capacitance value varies between  $1.8\text{pF}$  and  $5\text{pF}$ . Comparing both datasets reveals a relation between the two different setups. This relation is shown in [Equation 5.1](#)

$$C_{\text{Nextron}} = 7.5 \cdot (C_{\text{Cascade33}})^{1.6} \quad (5.1)$$

If this relation is used on the high-temperature dataset, the capacitance value at  $600^\circ\text{C}$  is between  $16\text{pF}$  and  $18\text{pF}$ . Because this relationship between the measurement setups is not a single factor, the deviation is not just caused by an additional parasitic capacitance in series or parallel of the DUT but by a more complex behaviour in the setup.

#### 5.2.5 Vacuum to atmospheric pressure at room temperature

In addition to changing the temperature, the pressure should also be varied. Since this is a pressure sensor, this parameter defines if the devices work as expected. This test is performed using a vacuum machine that can handle pressures that are much lower than the required  $80\text{Pa}$ . However, from a performance point of view, these low pressures are also tested.

The results of the full pressure range are shown in [Figure 5.14](#). The x-axis of this figure uses a logarithmic scale because of the large measurement range. The results

of these tests are repeatable and consistent. However, the results were not as expected compared to the design of the sensors. The capacitance value of the sensors increases as the pressure decreases. This is the opposite effect as the sensors were designed for, and the behaviour occurs regardless of sensor size and shape. The expected behaviour is that due to a decrease in pressure, the membrane would move up, increasing the distance to the bottom electrode and decreasing the capacitance value.

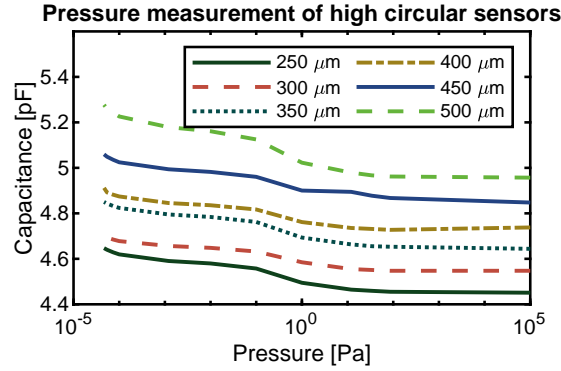


Figure 5.14: Pressure measurements of high circular sensors

Because the tests are repeatable and consistent, the membranes are sealed correctly and react to a pressure change. In addition, if the chamber is left in a vacuum, the capacitance value stays the same. Therefore, this unexpected result is not due to bad membranes. A reason for these values could be because of the buckling of the membranes. Due to the internal stresses in the material, the membrane could move down with a decreasing pressure instead of moving up.

In addition to capacitance values that go up with decreasing pressure, the change in capacitance is significantly smaller than designed. The low-pressure sensor design should measure the pressure range from  $80\text{ Pa}$  to  $100\text{ kPa}$ . These measurements include this range. The low-pressure sensor was designed to have a radius of  $470\mu\text{m}$  and a height of  $8.5\mu\text{m}$ . If a sensor with a height of  $6.75\mu\text{m}$  and a radius of  $500\mu\text{m}$  is measured, the capacitance change between  $80\text{ Pa}$  and  $100\text{ kPa}$  is  $5\text{ fF}$  to  $8\text{ fF}$ . This is much lower than the  $200\text{ fF}$  that was concluded from simulations. The results from designs for the low-pressure sensor are shown in Figure 5.15. Here, the designs have a height of  $6.75\mu\text{m}$ . The results from the design with a  $500\mu\text{m}$  radius is shown using the left y-axis, and the result from the design with a  $400\mu\text{m}$  radius is shown using the right y-axis.

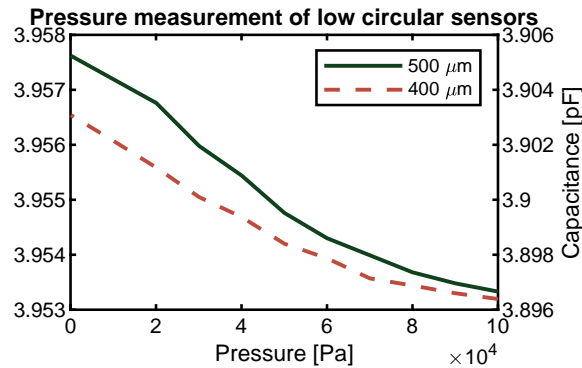


Figure 5.15: Pressure measurements of low circular sensors, from  $80\text{ Pa}$  to  $100\text{ kPa}$ . Two sensors are displayed, one with a radius of  $500\mu\text{m}$  (left y-axis) and one with a radius of  $400\mu\text{m}$  (right y-axis)

### 5.2.6 Measurements at elevated pressures

After the unexpected results for pressures lower than ambient pressure, the next tests are done at elevated pressures. Because of difficulties with wire bonding, only a few sensors could be tested using this manner. The characteristics of the produced sensors are revealed by comparing the capacitance reading with the reference pressure sensor. The commercial pressure sensor is relatively noisy. However, because the measurement rate is around four measurements per second, averaging of the result is possible. An example of the unfiltered data is shown in Figure 5.16. Even though the data is scattered, there is a clear trend between the pressure and capacitance.

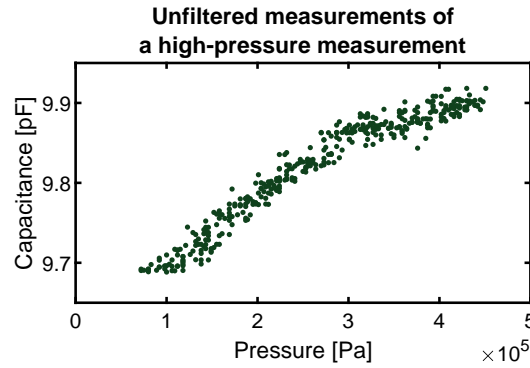


Figure 5.16: Unfiltered high-pressure measurement of a low circular membrane with radius of  $400\mu\text{m}$

After filtering using a moving mean filter, the trend becomes clearer. Three measurements of high-pressure measurements using this setup is shown in Figure 5.17. The exact capacitance value is not correct yet, since the sensor should be calibrated using this setup, as discussed in Section 4.3.6.

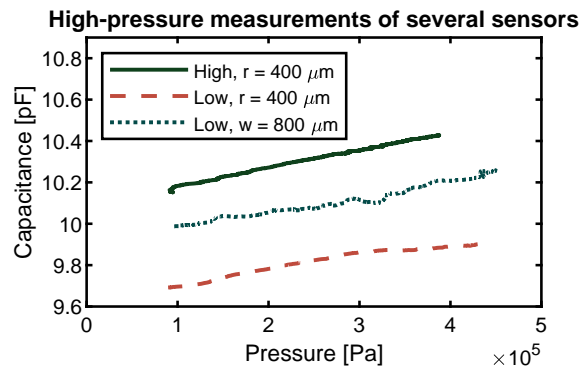


Figure 5.17: Measurement results of two circular and one square sensor

After calibration, the following results are gained. In Figure 5.18a, the low circular membranes are displayed. Figure 5.18b shows one working high circular membrane and Figure 5.18c shows square membrane measurements.

## 5.3 VERIFICATION OF SIMULATION

While the sensors have been designed with specific parameters in mind, some deviation from these parameters still occurred during production. An example is the thickness of the membrane. The produced devices have a thickness of  $10.8\mu\text{m}$  instead of the designed  $5\mu\text{m}$ . In addition, the buckling effect occurs, while this

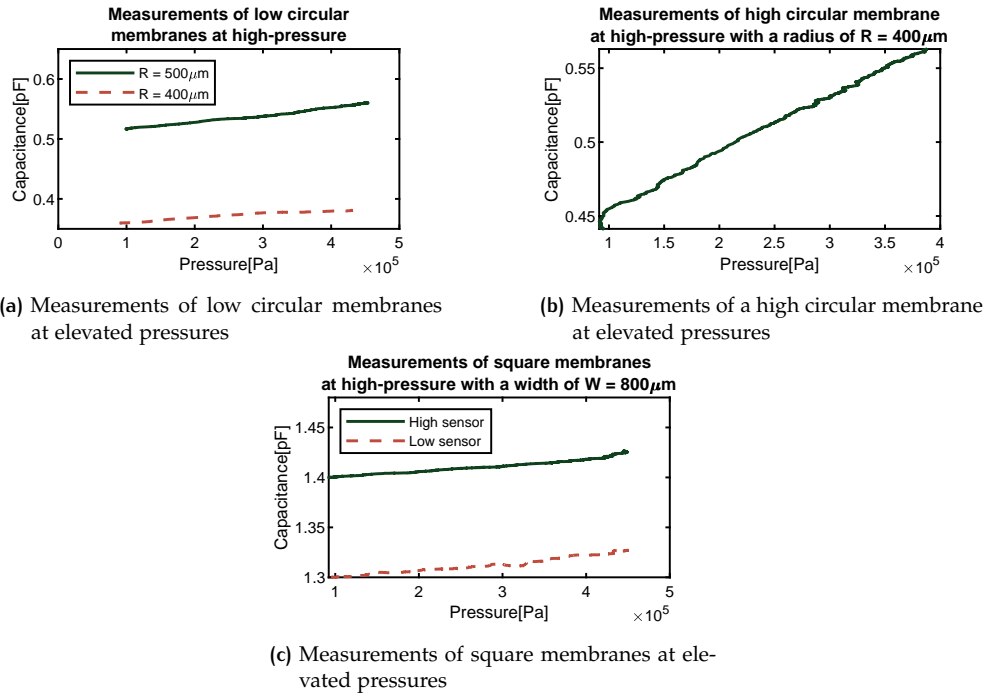


Figure 5.18: Measurements of sensors at elevated pressures

was not simulated. The result is that the sensors behave differently. This is also confirmed during measurements, where base capacitance values are different than expected, and the reaction to a changing pressure has an opposite effect as to what is expected.

To explain these behaviours, the simulations are adjusted with the parameters that the sensors are actually produced with. The measurements can then be compared to the new simulations, giving insight into why the changes are present.

### 5.3.1 Sensors at atmospheric pressure

The first measurements that will be confirmed are those performed at atmospheric pressure. These measurements get the base capacitance of the sensors at atmospheric pressure for different sensor sizes. For this simulation, the COMSOL model will be adjusted to the features of the produced sensors. First of all, the buckling mode with the high centre is simulated by changing the membrane shape. Another option would have been to simulate the model with internal stresses. However, due to the unpredictable nature of the buckling, a good simulation with internal stresses was not feasible. Therefore, the buckling is imitated using an altered membrane shape only. The thickness of the membrane and the cavity's height is also adjusted. Figure 5.19 shows the adjusted model.

While processing the measurements, an offset was discovered compared to the simulations. The measured values from the *Cascade 33* setup all had an offset of  $0.34 \text{ pF}$ . This offset is likely caused by parasitic capacitances. The simulation assumes that the capacitance measurement is done from the top and bottom terminal directly. In reality, the measurements are taken from the connection pads that are at a distance from the terminals. This introduces parasitic capacitances to the measurements. Because this value is relatively constant, the parasitic capacitance does not influence the measurements.

If the parasitic capacitance value is subtracted from the measurements, the acquired data can be compared to the simulation. Figure 5.20a shows the comparison between these two datasets.



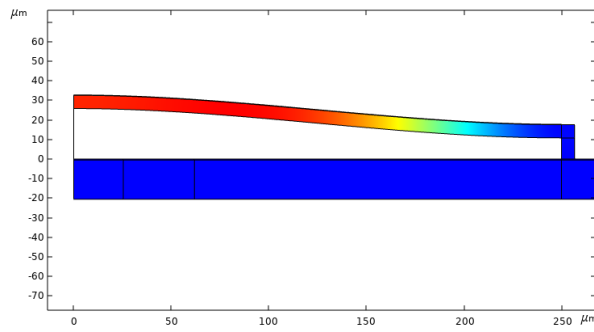


Figure 5.19: Adjusted simulation including a high-centre buckling effect

Next to the low circular sensors, the high circular sensor measurements are also compared to the simulation. Using the same offset, the parasitics in the measured values are compensated. The result of this comparison is shown in Figure 5.20b. Finally, square membranes have also been simulated. The values of the low square membranes are comparable to the measurements. However, the high square simulations could not converge correctly due to the buckling effect. Therefore, these results are not included.

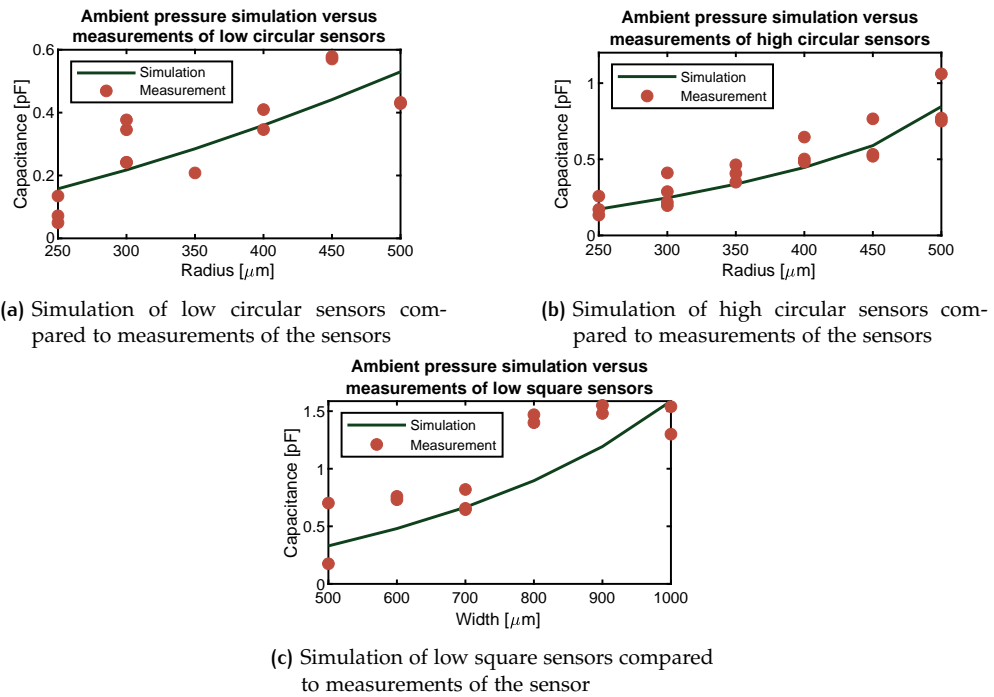


Figure 5.20: Measurements compared to the simulation of membranes at ambient pressure

### 5.3.2 Sensors at elevated temperatures

The next measurements were taken at ambient pressures and elevated temperatures. From the measurements, increasing the temperature increases the capacitance output. This contrasts the earlier simulation, where the capacitance lowers with a higher temperature.

Even though the simulation has been adjusted for the production parameters and a form of buckling is included, the simulation still chooses the membrane to move up with a higher temperature. The simulation results show that the capacitance goes down with a higher temperature. The result of this simulation is seen in Figure 5.21a, and it can be compared to the measurement results at Figure 5.21b.

Switching to a different shape or size does not change the simulation's behaviour. The capacitance values between the simulation and measurement do not match due to the high readouts of the Nextron setup.

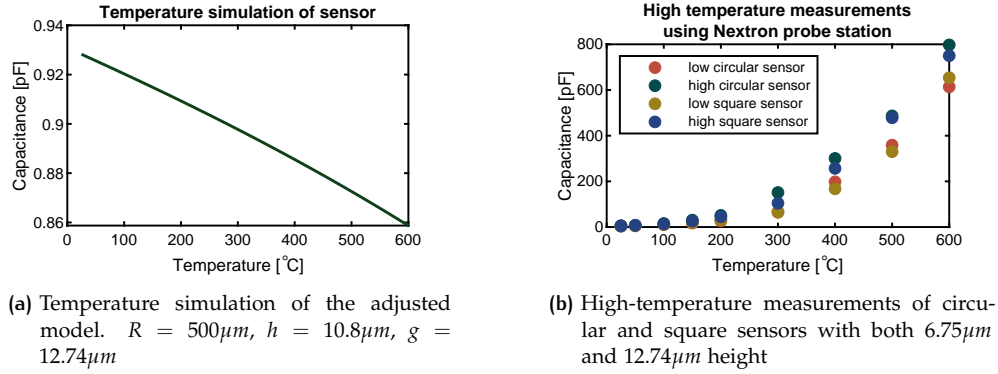


Figure 5.21: Measurements compared to the simulation of circular membranes at elevated temperatures

### 5.3.3 Sensors at vacuum

Finally, measurements under a vacuum are performed. These results do not match the previously simulated designs like the temperature measurements. Instead of reading a lower capacitance as the pressure decreases, the capacitance value increases with decreasing pressure. Again, this behaviour could result from the buckled membranes that behave differently than intended. This behaviour could not be replicated using the simulation. Therefore, only a comparison between the updated simulation and the measured results can be given. These are shown in Figure 5.22. The capacitance values between the simulation and measurement do not match due to the high readouts of the Nextron setup.

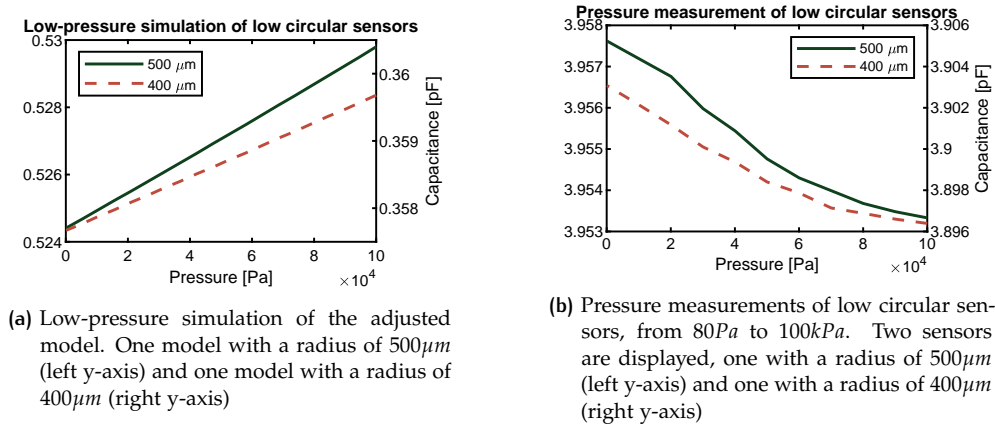


Figure 5.22: Measurements compared to simulation of circular membranes at low pressures

### 5.3.4 Sensors at elevated pressures

The last measurements include sensors at elevated pressures. These measurements show a characteristic that is expected. As the pressure increases, the capacitance will also increase. With adjusted simulations for the buckling effect, these measurements are evaluated.

First, the low circular membranes are evaluated. The result of the updated simulation versus the measurements is shown in Figure 5.23. Two different sizes are

measured. The membranes with a radius of  $500\mu m$  use the left y-axis, and the membranes with a radius of  $400\mu m$  use the right y-axis. Even though the results do not match exactly, the measured data is relatively close to the simulated data, especially the increased capacitance per pascal.

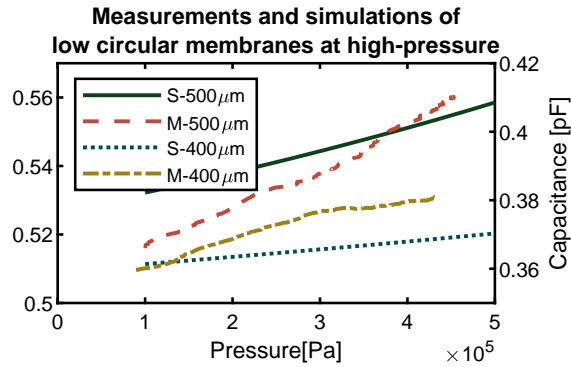


Figure 5.23: Simulations and measurements of low circular membranes at high-pressure. Membranes with  $500\mu m$  radius use the left y-axis and membranes with  $400\mu m$  radius use the right y-axis

Next, the high circular membrane is evaluated. This is shown in Figure 5.24. This result deviates more from the low circular membranes. The membrane in the simulation is more bent and closer to the bottom of the cavity. Therefore, the exponential behaviour is visible. The measured membrane on the other hand, is farther away from the bottom of the cavity. Therefore, this exponential behaviour is not present.

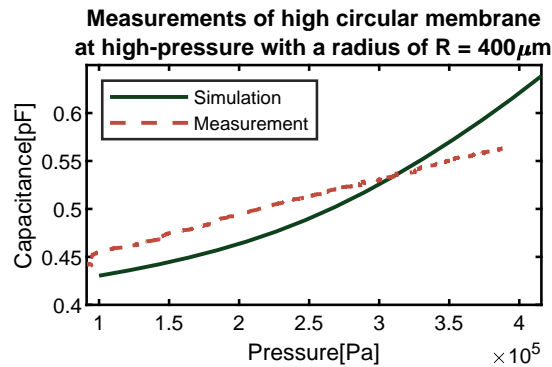


Figure 5.24: Simulation and measurement of a high circular membrane at high pressure

## 5.4 CONCLUSION

After different types of measurements, it can be concluded that the sensors are receptive to pressure changes. Therefore, the sensors can be used to determine the absolute pressure in an environment. It has been confirmed that larger sensor membranes lead to higher capacitive output values. In addition, the bottom contact division is also relatively accurate. During production, the sensor membranes experienced buckling. This buckling effect has had some impact on the characteristics of the produced sensors. One effect that this buckling effect may cause is the effect on temperature. The sensors react opposite to what the simulation shows. In addition, the capacitance of the sensors increases when a vacuum is created. This effect is also opposite to what the simulation shows. When increasing the pressure up to  $400kPa$ , the sensors behave as expected. However, due to alterations during production, the

sensors are not exactly as designed. Therefore, the readings are different from the original design. The advantage is that the sensors do not need compensation to get a linear output. The disadvantage is that the sensitivity of the sensors is lower than the designs. The sensitivity of the best device is  $0.025 fF/100 Pa$  instead of the designed  $0.3 fF/100 Pa$ .

# 6

## CONCLUSION AND FUTURE WORK

During the course of this work, pressure sensors have been designed, created and measured. After the process, it has been confirmed that the sensors are reacting to a change in pressure. Especially pressures higher than the environmental pressure have the intended effect. Due to problems during production, the membrane of the sensors is thicker than intended. As discovered during the theoretical approach, having a thicker membrane causes the sensors to have a milder reaction to pressure changes. This is visible because the best sensor has a sensitivity of  $0.025 fF/100 Pa$  compared to the designed  $0.3 fF/100 Pa$ . Another unwanted effect is that the membranes experience a buckling effect. This likely causes behaviour that is not intended. The reaction to temperature is opposite to the expected reaction and the behaviour to pressures lower than environmental pressures is opposite as well. Even though these measurements are not as intended, they are repeatable and consistent. Therefore, these characteristics can still be used in pressure sensing.

During the production, some interesting problems were encountered. One of the problems is that the PECVD SiN layer delaminated after depositing LPCVD SiC. This delamination effect only occurred on the molybdenum metal, and not anywhere else. An explanation for this is that the molybdenum reacted with precursor gasses of the PECVD SiN, or that the stresses due to the high temperature were enough to delaminate the layer. Because of this delamination, the decision has been made to omit the passivation layer.

The problems with the production of the sensor have mostly been resolved on the go. However, the buckling effect was not fixed. If these sensors are produced again, then the design should be reconsidered to minimise the chances of buckling.

### 6.1 FUTURE WORK

If this project is to be continued, there are a few improvements possible for future work. A few have been mentioned above or in the other chapters, but a list is given in this section.

#### 6.1.1 Sensor design improvements

The first part of the improvement list is about the sensor design. This should reduce the risk of buckling membranes, while still producing the same sensors. The proposed improvement is to build the sensor inside the wafer instead of on top. First, holes have to be created to fit the sensors inside. Afterwards, these holes are filled with sacrificial material. When the holes are fully filled, a membrane can be placed that is straight and level with the wafer. This approach omits the high structures and difficulties dealing with them. In addition, the stresses due to thermal expansion will be less prominent because the membrane is not elevated.

#### 6.1.2 Mask design improvements

During production, a few possible improvements were listed. These improvements are based on experiences during the construction of the sensors. The first improve-

ment is to make sure the most important designs are placed around the centre of the wafer. Due to the photoresist spincoating on top of the wafer, the designs at the edges are most vulnerable to inconsistencies in this layer.

The next improvement is to make sure texts and other details are on a layer that will take small details. In this case, the overlay metal layer did not transfer small details like text. If the texts were placed on the bottom contact marks layer, they would have been visible.

Finally, an improvement would be to create or use a mirror-symmetrical alignment mask. The alignment will not be influenced even if the masks are ordered backwards.

### 6.1.3 Process improvements

Next to changes in the masks, some general improvements in the process are possible. The first improvement is to redesign the sacrificial structures. Adding material on already existing sacrificial structures and removing it afterwards degrades the quality, as seen with the  $14\mu m$  variants.

Next, an improvement would be to increase the bottom metal layer thickness. It makes it easier to land on the material when creating vias. And finally, due to problems with the gold overlay, the wire bonding did not succeed easily. The parameters should be reviewed to improve the gold overlay adhesion.

### 6.1.4 Measurement improvements

Finally, some notes about the measurements can be made. The first suggestion is to validate why the Nextron probe station has extremely high values. Even though the same LCR meter is used, the results from this probe station are too high compared to other measurements. This makes it difficult to use these values.

And the last suggestion is about the custom PCB. It was difficult to calibrate it correctly. A better solution should be implemented in either the hardware or the software of the measurement PCB.

## BIBLIOGRAPHY

- [1] PowerElectronicsUK and Catapult, "Opportunities and Challenges of Wide Band Gap Power Devices," 3 2020.
- [2] J.-S. Park and Y. B. Gianchandani, "A Servo-Controlled Capacitive Pressure Sensor with a Three-Mask Fabrication Sequence," *Transducers '01 Eurosensors XV*, pp. 506–509, 2001.
- [3] Z. Liu, Y. Pan, P. Wu, L. Du, Z. Zhao, and Z. Fang, "A novel capacitive pressure sensor based on non-coplanar comb electrodes," *Sensors and Actuators A: Physical*, vol. 297, p. 111525, 10 2019. [Online]. Available: <https://linkinghub.elsevier.com/retrieve/pii/S0924424719310520>
- [4] H. Lv, H. Yu, and G. Hu, "A SiC high-temperature Pressure Sensor Operating in Severe Condition," *TELKOMNIKA Indonesian Journal of Electrical Engineering*, vol. 10, no. 8, 12 2012. [Online]. Available: <http://www.iaesjournal.com/online/index.php/TELKOMNIKA/article/view/1692>
- [5] "What are high temperature electronics? - TWI." [Online]. Available: <https://www.twi-global.com/technical-knowledge/faqs/faq-what-are-high-temperature-electronics>
- [6] D. B. Thomas, J. D. Cressler, J. Papapolymerou, and G. D. Durgin, "SILICON-GERMANIUM DEVICES AND CIRCUITS FOR HIGH TEMPERATURE APPLICATIONS," 2010.
- [7] "Conduction in Semiconductors — PVEducation." [Online]. Available: <https://www.pveducation.org/pvcdrom/conduction-in-semiconductors>
- [8] P. G. Neudeck, R. S. Okojie, and L. Y. Chen, "High-temperature electronics - A role for wide bandgap semiconductors?" *Proceedings of the IEEE*, vol. 90, no. 6, pp. 1065–1076, 2002. [Online]. Available: <https://www.researchgate.net/publication/4708649-High-Temperature-Electronics-A-Role-for-Wide-Bandgap-Semiconductors>
- [9] H. Jin, L. Qin, L. Zhang, X. Zeng, and R. Yang, "Review of wide band-gap semiconductors technology." [Online]. Available: <http://www.matec-conferences.org>
- [10] "Advantages of Wide Bandgap Semiconductors." [Online]. Available: <https://www.astrodynetdi.com/blog/what-is-the-future-for-gan-and-sic-in-the-semiconductor-industry>
- [11] F. Kyle, R. K. C. Goetz, M. N. Ericson, D. C. Sweeney, and N. D. Bull Ezell, "Wide Bandgap Semiconductors for Extreme Temperature and Radiation Environments," 2022. [Online]. Available: <http://www.osti.gov/contact.html>
- [12] M. F. Kaplan and N. Structural, "UNIVERSITY OF CAPE TOWN RONOEBOSCH. CAPE TOWN. SOUTH AFRICA NUCLEAR RADIATION AND THE PROPERTIES OF CONCRETE UCT-NLSMRV)-TR-\*S~," 1983.
- [13] "IC Materials For Extreme Conditions." [Online]. Available: <https://semiengineering.com/ic-materials-for-extreme-conditions/>
- [14] N. G. Wright and A. B. Horsfall, "SiC sensors: a review," *Journal of Physics D: Applied Physics*, vol. 40, no. 20, pp. 6345–6354, 10 2007.



- [15] BIPM, "The International System of Units (9th edition of the SI Brochure)," 2019. [Online]. Available: [http://www.bipm.org/en/si/si\\_brochure/](http://www.bipm.org/en/si/si_brochure/)
- [16] Y. V. Polezhaev, "THERMAL CONDUCTIVITY," 2011. [Online]. Available: <http://www.thermopedia.com/content/1186/>
- [17] L. M. Middelburg, H. W. van Zeijl, S. Vollebregt, B. Morana, and G. Zhang, "Toward a Self-Sensing Piezoresistive Pressure Sensor for All-SiC Monolithic Integration," *IEEE Sensors Journal*, vol. 20, no. 19, pp. 11 265–11 274, 10 2020. [Online]. Available: <https://ieeexplore.ieee.org/document/9104676/>
- [18] J. Sun, D. Hu, Z. Liu, L. M. Middelburg, S. Vollebregt, P. M. Sarro, and G. Zhang, "Low power AlGaIn/GaN MEMS pressure sensor for high vacuum application," *Sensors and Actuators A: Physical*, vol. 314, p. 112217, 10 2020. [Online]. Available: <https://doi.org/10.1016/j.sna.2020.112217>
- [19] X. Fang, C. Wu, X. Guo, L. Zhao, Y. Zhao, and Z. Jiang, "Development of a 4H-SiC Piezoresistive Pressure Sensor for High Temperature Applications," in *2019 IEEE 14th International Conference on Nano/Micro Engineered and Molecular Systems (NEMS)*, vol. 0. IEEE, 4 2019, pp. 105–109. [Online]. Available: <https://ieeexplore.ieee.org/document/8915652/>
- [20] L. Wang, Y. Zhao, Y. Zhao, Y. Yang, B. Li, and T. Gong, "Mass fabrication of 4H-SiC high temperature pressure sensors by femtosecond laser etching," in *2021 IEEE 16th International Conference on Nano/Micro Engineered and Molecular Systems (NEMS)*, no. d. IEEE, 4 2021, pp. 1478–1481. [Online]. Available: <https://ieeexplore.ieee.org/document/9451358/>
- [21] Y. Li, T. Liang, C. Lei, Q. Li, Z. Li, A. Ghaffar, and J. Xiong, "Study on the Stability of the Electrical Connection of High-Temperature Pressure Sensor Based on the Piezoresistive Effect of P-Type SiC," *Micromachines*, vol. 12, no. 2, p. 216, 2 2021. [Online]. Available: <https://www.mdpi.com/2072-666X/12/2/216>
- [22] U. Erdem, "Pressure measurement." *Vacuum Deposition Onto Webs, Films and Foils*, pp. 57–65, 1 1984. [Online]. Available: <https://linkinghub.elsevier.com/retrieve/pii/B9780323296441000037>
- [23] Electronics-Cooling, "The thermal conductivity of gases," 1998. [Online]. Available: <https://www.electronics-cooling.com/1998/09/the-thermal-conductivity-of-gases/>
- [24] J. Mo, L. M. Middelburg, B. Morana, H. W. Van Zeijl, S. Vollebregt, and G. Zhang, "Surface-Micromachined Silicon Carbide Pirani Gauges for Harsh Environments," *IEEE Sensors Journal*, vol. 21, no. 2, pp. 1350–1358, 1 2021. [Online]. Available: <https://ieeexplore.ieee.org/document/9178352/>
- [25] Z. Huang, Y. Zhu, F. Shen, and A. Wang, "Sapphire-fiber-based white-light interferometric sensor for high-temperature measurements," *Optics Letters*, Vol. 30, Issue 7, pp. 711–713, vol. 30, no. 7, pp. 711–713, 4 2005. [Online]. Available: <https://opg.optica.org/viewmedia.cfm?uri=ol-30-7-711&seq=0&html=truehttps://opg.optica.org/abstract.cfm?uri=ol-30-7-711https://opg.optica.org/ol/abstract.cfm?uri=ol-30-7-711>
- [26] K. S. Rao, W. Samyuktha, D. V. Vardhan, B. G. Naidu, P. A. Kumar, K. G. Sravani, and K. Guha, "Design and sensitivity analysis of capacitive MEMS pressure sensor for blood pressure measurement," *Microsystem Technologies* 2020 26:8, vol. 26, no. 8, pp. 2371–2379, 3 2020. [Online]. Available: <https://link.springer.com/article/10.1007/s00542-020-04777-x>

- [27] Yuelin Wang and M. Esashi, "A novel electrostatic servo capacitive vacuum sensor," in *Proceedings of International Solid State Sensors and Actuators Conference (Transducers '97)*, vol. 2. IEEE, 1997, pp. 1457–1460. [Online]. Available: <http://ieeexplore.ieee.org/document/635739/>
- [28] W. H. Ko and Q. Wang, "Touch mode capacitive pressure sensors," *Sensors and Actuators A: Physical*, vol. 75, no. 3, pp. 242–251, 6 1999.
- [29] H.-P. Phan, D. V. Dao, K. Nakamura, S. Dimitrijević, and N.-T. Nguyen, "The Piezoresistive Effect of SiC for MEMS Sensors at High Temperatures: A Review," *Journal of Microelectromechanical Systems*, vol. 24, no. 6, pp. 1663–1677, 12 2015. [Online]. Available: <http://ieeexplore.ieee.org/document/7243309/>
- [30] M. A. Fraga, H. Furlan, M. Massi, I. C. Oliveira, and L. L. Koberstein, "Fabrication and characterization of a SiC/SiO<sub>2</sub>/Si piezoresistive pressure sensor," *Procedia Engineering*, vol. 5, pp. 609–612, 2010.
- [31] H. P. Phan, K. M. Dowling, T. K. Nguyen, T. Dinh, D. G. Senesky, T. Namazu, D. V. Dao, and N. T. Nguyen, "Highly sensitive pressure sensors employing 3C-SiC nanowires fabricated on a free standing structure," *Materials and Design*, vol. 156, pp. 16–21, 10 2018.
- [32] J. S. Park and Y. B. Gianchandani, "A servo-controlled capacitive pressure sensor using a capped-cylinder structure microfabricated by a three-mask process," *Journal of Microelectromechanical Systems*, vol. 12, no. 2, pp. 209–220, 4 2003. [Online]. Available: <http://ieeexplore.ieee.org/document/1192716/>
- [33] H. W. Benzel, T. Kallfass, and E. Lueder, "Highly linear capacitive pressure sensors with optimized electrode shapes," in *Technical Digest - International Electron Devices Meeting*. Publ by IEEE, 1993, pp. 203–206.
- [34] Y. Hezarjaribi, M. N. Hamidon, S. H. Keshmiri, and A. R. Bahadorimehr, "Capacitive pressure sensors based on MEMS, operating in harsh environments," *IEEE International Conference on Semiconductor Electronics, Proceedings, ICSE*, pp. 184–187, 11 2008. [Online]. Available: <http://ieeexplore.ieee.org/document/4770304/>
- [35] S. Jin, S. Rajgopal, and M. Mehregany, "Silicon carbide pressure sensor for high temperature and high pressure applications: Influence of substrate material on performance," in *2011 16th International Solid-State Sensors, Actuators and Microsystems Conference*. IEEE, 6 2011, pp. 2026–2029. [Online]. Available: <http://ieeexplore.ieee.org/document/5969209/>
- [36] X. Han, M. Xu, G. Li, H. Yan, Y. Feng, and D. Li, "Design and experiment of a touch mode MEMS capacitance vacuum gauge with square diaphragm," *Sensors and Actuators A: Physical*, vol. 313, p. 112154, 10 2020. [Online]. Available: <https://linkinghub.elsevier.com/retrieve/pii/S0924424720300856>
- [37] L. Chen and M. Mehregany, "A silicon carbide capacitive pressure sensor for in-cylinder pressure measurement," *Sensors and Actuators A: Physical*, vol. 145–146, no. 1–2, pp. 2–8, 7 2008. [Online]. Available: <https://linkinghub.elsevier.com/retrieve/pii/S0924424707007005>
- [38] Z. Niu, Y. Zhao, and B. Tian, "Design optimization of high pressure and high temperature piezoresistive pressure sensor for high sensitivity," *Review of Scientific Instruments*, vol. 85, no. 1, p. 015001, 1 2014. [Online]. Available: <https://aip.scitation.org/doi/abs/10.1063/1.4856455>
- [39] L. Beker, A. Maralani, L. Lin, and A. P. Pisano, "A silicon carbide differential output pressure sensor by concentrically matched capacitance," *Proceedings of the IEEE International Conference on Micro Electro Mechanical Systems (MEMS)*, pp. 981–984, 2 2017.

- [40] "Manifold Absolute Pressure Sensor - Spectra Premium." [Online]. Available: <https://www.spectrapremium.com/en/aftermarket/north-america/manifold-absolute-pressure-sensor>
- [41] "Exhaust Pressure Sensors (EPS)." [Online]. Available: <https://premierautotrade.com.au/news/exhaust-pressure-sensors-eps.php>
- [42] "MANIFOLD ABSOLUTE PRESSURE SENSOR (MAP SENSOR)." [Online]. Available: <https://autoditex.com/page/manifold-absolute-pressure-sensor-map-sensor-20-1.html>
- [43] "Making sense of your sensors: DPF differential pressure sensor — Delphi Auto Parts." [Online]. Available: <https://www.delphiautoparts.com/gbr/en/resource-center/making-sense-your-sensors-dpf-differential-pressure-sensor>
- [44] "Installation instructions for Differential Pressure Sensor Delta-P Part-No. 60105." [Online]. Available: [www.enginesens.com](http://www.enginesens.com)
- [45] "Vacuum annealing." [Online]. Available: <http://www.coatec.de/Vacuum-annealing.103.0.html?&L=1>
- [46] "Annealing in vacuum - ALD Heat-Treatment-Service." [Online]. Available: <https://www.heat-treatment-services.com/processes-more/annealing/>
- [47] "VACUUM TEMPERING APPLICATIONS." [Online]. Available: <https://www.asminternational.org/documents/10192/1912376/http00505p035.pdf/476b523d-53e0-45d8-8e3d-d4ca62c499bc/HTP00505P035>
- [48] "Tempering - ALD Heat-Treatment-Service." [Online]. Available: <https://www.heat-treatment-services.com/processes-more/tempering/>
- [49] "Low Temperature Vacuum Processing." [Online]. Available: <https://vacaero.com/information-resources/vac-aero-training/153784-low-temperature-vacuum-processing.html>
- [50] "Vacuum Ovens." [Online]. Available: <https://www.mrclab.com/vacuum-ovens>
- [51] D. B. Gil, "2-1 SENSOR REQUIREMENTS FOR ACTIVE GAS TURBINE ENGINE CONTROL," *Prime Faraday Technology Watch- Wolfson School of Mechanical and Manufacturing Engineering*, no. January, p. 51, 2002. [Online]. Available: [https://www.academia.edu/6513673/2.1\\_SENSOR\\_REQUIREMENTS\\_FOR\\_ACTIVE\\_GAS\\_TURBINE\\_ENGINE\\_CONTROL](https://www.academia.edu/6513673/2.1_SENSOR_REQUIREMENTS_FOR_ACTIVE_GAS_TURBINE_ENGINE_CONTROL)
- [52] "Benefits - Glenn Research Center — NASA." [Online]. Available: <https://www1.grc.nasa.gov/research-and-engineering/silicon-carbide-electronics-and-sensors/benefits/>
- [53] V. Rochus, B. Wang, H. A. Tilmans, A. Ray Chaudhuri, P. Helin, S. Severi, and X. Rottenberg, "Fast analytical design of MEMS capacitive pressure sensors with sealed cavities," *Mechatronics*, vol. 40, pp. 244–250, 12 2016.
- [54] M. Kang, C. Ri, and J. Choe, "Capacitance response of concave well substrate touch-mode capacitive pressure sensor: Mathematical analysis and simulation," *Microelectronics Journal*, vol. 114, p. 105118, 8 2021. [Online]. Available: <https://linkinghub.elsevier.com/retrieve/pii/S0026269221001294>
- [55] M. Daigle, J. Corcos, and K. Wu, "An analytical solution to circular touch mode capacitor," *IEEE Sensors Journal*, vol. 7, no. 4, pp. 502–505, 4 2007.
- [56] L. M. Middelburg, "From Silicon toward Silicon Carbide Smart Integrated Sensors," *TU Delft University*, p. 289, 2020.

- [57] M. Rahman and S. Chowdhury, "A highly accurate method to calculate capacitance of MEMS sensors with circular membranes," in *Proceedings of 2009 IEEE International Conference on Electro/Information Technology, EIT 2009*, 2009, pp. 178–181.
- [58] M. A. Varma and S. K. Jindal, "Novel design for performance enhancement of a touch-mode capacitive pressure sensor: theoretical modeling and numerical simulation," *Journal of Computational Electronics*, vol. 17, no. 3, pp. 1324–1333, 9 2018. [Online]. Available: <https://link.springer.com/article/10.1007/s10825-018-1174-0>
- [59] S. Sathyanarayanan and A. V. Juliet, "Design and simulation of touch mode MEMS capacitive pressure sensor," *ICMET 2010 - 2010 International Conference on Mechanical and Electrical Technology, Proceedings*, pp. 180–183, 2010.
- [60] Q. Wang and W. H. Ko, "Modeling of touch mode capacitive sensors and diaphragms," *Sensors and Actuators A: Physical*, vol. 75, no. 3, pp. 230–241, 6 1999. [Online]. Available: <https://linkinghub.elsevier.com/retrieve/pii/S0924424799000680>
- [61] PAM-XIAMEN, "Property of Silicon Carbide," 2012. [Online]. Available: [http://www.qualitymaterial.net/news\\_list85.html](http://www.qualitymaterial.net/news_list85.html)
- [62] S. N. Perevislov, "Determination of the Temperature Coefficient of Linear Expansion of Materials Based on Silicon Carbide," *Refractories and Industrial Ceramics*, vol. 61, no. 6, pp. 665–670, 3 2021. [Online]. Available: <https://link.springer.com/article/10.1007/s11148-021-00539-y>
- [63] M. Vila, D. Cáceres, and C. Prieto, "Mechanical properties of sputtered silicon nitride thin films," *Journal of Applied Physics*, vol. 94, no. 12, pp. 7868–7873, 12 2003.
- [64] AZO Materials, "Properties: Silicon Nitride (Si<sub>3</sub>N<sub>4</sub>) Properties and Applications," pp. 1–6, 2015. [Online]. Available: <https://www.azom.com/properties.aspx?ArticleID=53>
- [65] Engineering ToolBox, "Thermal Expansion - Linear Expansion Coefficients. [online]," 2003. [Online]. Available: [https://www.engineeringtoolbox.com/linear-expansion-coefficients-d\\_95.html](https://www.engineeringtoolbox.com/linear-expansion-coefficients-d_95.html)
- [66] L. Fuller and S. Bolster, "Lithography Using ASML Stepper Introduction to ASML PAS 5500 Wafer Alignment and Exposure Lithography Using ASML Stepper," 4 2014. [Online]. Available: <http://people.rit.edu/lffeee>
- [67] B. Jean-Luc and D. Bruno, "Contamination Monitoring and Analysis in Semiconductor Manufacturing," in *Semiconductor Technologies*. InTech, 4 2010.
- [68] S. Laurén, "Wetting in electronics - How HMDS treatment works?" 7 2021. [Online]. Available: <https://www.biolinscientific.com/blog/wetting-in-electronics-how-hmds-treatment-works>
- [69] J. Griffin, H. Hassan, and E. Spooner, "Spin Coating: Complete Guide to Theory and Techniques — Ossila." [Online]. Available: <https://www.ossila.com/en-eu/pages/spin-coating>
- [70] "Plasma Enhanced Chemical Vapor Deposition (PECVD)." [Online]. Available: <https://corial.plasmatherm.com/en/technologies/pecvd-plasma-enhanced-chemical-vapor-deposition>
- [71] "What is Sputtering? Magnetron Sputtering?" [Online]. Available: <https://www.semicore.com/what-is-sputtering>

- [72] B. Morana, *Silicon Carbide Thin Films for MEMS Nanoreactors for in-situ Transmission Electron Microscopy*, 2015.
- [73] "Reactive Ion Etching Systems — RIE Etch Process — Plasma Etch, Inc." [Online]. Available: <https://www.plasmaetch.com/reactive-ion-etching-systems-rie.php>
- [74] J. A. Woollam, "Guide to using WVASE spectroscopic Ellipsometry Data Acquisition and Analysis Software," Tech. Rep., 1994. [Online]. Available: <http://www.jawoollam.com>
- [75] N. Liu, J. Kim, J. Oh, Q. T. Nguyen, B. B. Sahu, J. G. Han, and S. Kim, "Growth of Multiorientated Polycrystalline MoS<sub>2</sub> Using Plasma-Enhanced Chemical Vapor Deposition for Efficient Hydrogen Evolution Reactions," *Nanomaterials* 2020, Vol. 10, Page 1465, vol. 10, no. 8, p. 1465, 7 2020. [Online]. Available: <https://www.mdpi.com/2079-4991/10/8/1465/html>  
<https://www.mdpi.com/2079-4991/10/8/1465>
- [76] N. Jehanathan, "THERMAL STABILITY OF PLASMA ENHANCED CHEMICAL VAPOR DEPOSITED SILICON NITRIDE THIN FILMS," Ph.D. dissertation, 2007.
- [77] M. Fraga and R. Pessoa, "micromachines Review Progresses in Synthesis and Application of SiC Films: From CVD to ALD and from MEMS to NEMS." [Online]. Available: [www.mdpi.com/journal/micromachines](http://www.mdpi.com/journal/micromachines)
- [78] "Etching, Process to Complete Semiconductor Patterning - 2 — SK hynix Newsroom." [Online]. Available: <https://news.skhynix.com/etching-process-to-complete-semiconductor-patterning-2/>
- [79] Analog Devices, "24-Bit Capacitance-to-Digital Converter with Temperature Sensor. datasheet. 2007," *Nonlinearity*, 2007. [Online]. Available: <http://www.analog.com/media/en/technical-documentation/data-sheets/AD7747.pdf>
- [80] Texas Instruments, "FDC1004 4 Channel capacitance-to-digital converter for capacitive sensing solutions," *Data Sheet*, pp. 1–33, 2015. [Online]. Available: <https://www.ti.com/lit/ds/symlink/fdc1004.pdf>
- [81] A. Devices, "AD7150 Ultralow Power, 2-Channel , Capacitance Converter for Proximity Sensing," 2019. [Online]. Available: <https://www.analog.com/media/en/technical-documentation/data-sheets/ad7150.pdf>
- [82] D. Information, "FDC2x1x EMI-Resistant 28-Bit , 12-Bit Capacitance-to-Digital Converter for Proximity and PACKAGE," 2015. [Online]. Available: <https://www.ti.com/lit/ds/symlink/fdc2212.pdf>
- [83] C.-t.-d. Converter, "PCAPo4 Capacitance-to-Digital Converter," no. Cdc, 2018. [Online]. Available: <https://www.sciosense.com/wp-content/uploads/documents/PCap04-Datasheet.pdf>
- [84] Analog Devices, "AD7147: CapTouch® Programmable Controller for Single-Electrode Capacitance Sensors (REV.D)," *Data Sheet*, [http://www.analog.com/static/imported-files/Data\\_Sheets/AD7147.pdf](http://www.analog.com/static/imported-files/Data_Sheets/AD7147.pdf), 2011. [Online]. Available: <https://www.analog.com/media/en/technical-documentation/data-sheets/AD7147.pdf>
- [85] A. Devices, "AD7142 - Programmable Controller for Capacitance Touch Sensors," *Update*, 2007. [Online]. Available: <https://www.analog.com/media/en/technical-documentation/data-sheets/ad7142.pdf>

- [86] “ESP32 WROOM 4Mb Devkit V1 Board met WiFi Bluetooth en Dual Core processor — ESP32 — OTRONIC Elektronica.” [Online]. Available: <https://www.otronic.nl/a-59613972/esp32/esp32-wroom-4mb-devkit-v1-board-met-wifi-bluetooth-en-dual-core-processor/>
- [87] “Li-ion Charge and Protection circuit 2100mA with DC-DC converter - MH-CD42.” [Online]. Available: <https://www.tinytronics.nl/shop/en/power/bms-and-chargers/li-ion-and-li-po/with-protection-circuit/li-ion-charge-and-protection-circuit-2100ma-with-dc-dc-converter>
- [88] Ds20001942g-Page, “MCP9700/9700A and MCP9701/9701A.” [Online]. Available: <http://ww1.microchip.com/downloads/en/devicedoc/20001942g.pdf>
- [89] “torehan/pcap04-arduino.” [Online]. Available: <https://github.com/torehan/pcap04-arduino>
- [90] “soo500/ESPUI: A simple web user interface library for ESP32 and ESP8266.” [Online]. Available: <https://github.com/soo500/ESPUI>
- [91] “BU-303: Confusion with Voltages - Battery University.” [Online]. Available: <https://batteryuniversity.com/article/bu-303-confusion-with-voltages>
- [92] V. Ziebart, O. Paul, and H. Baltes, “Strongly buckled square micromachined membranes,” *Journal of Microelectromechanical Systems*, vol. 8, no. 4, pp. 423–432, 12 1999.

# A

## APPENDIX: PCB SCHEMATICS

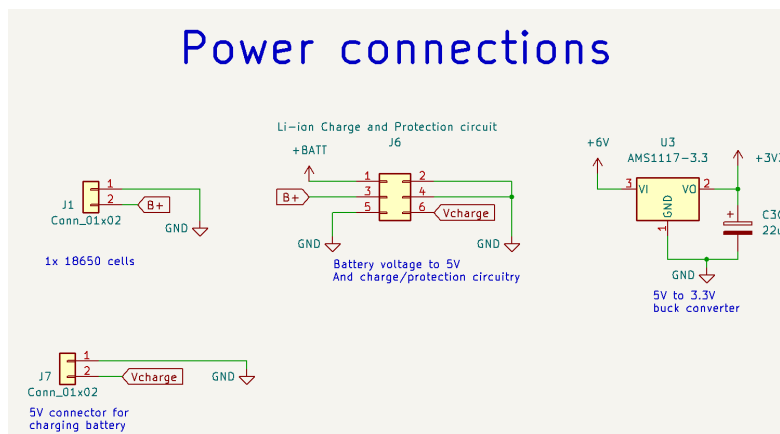
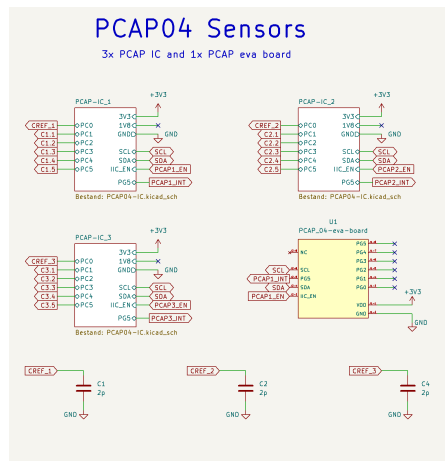
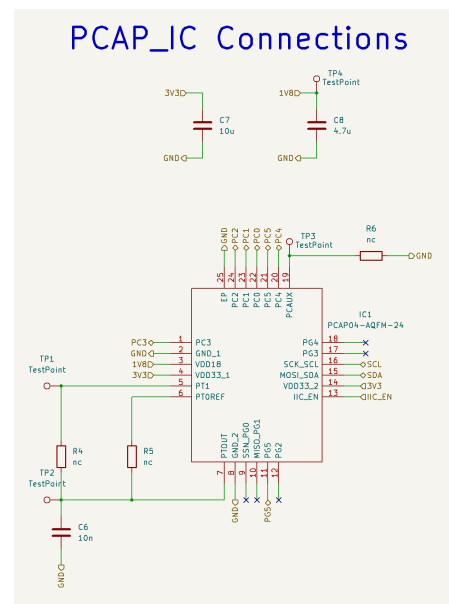


Figure A.1: Schematic design for the PCB power design





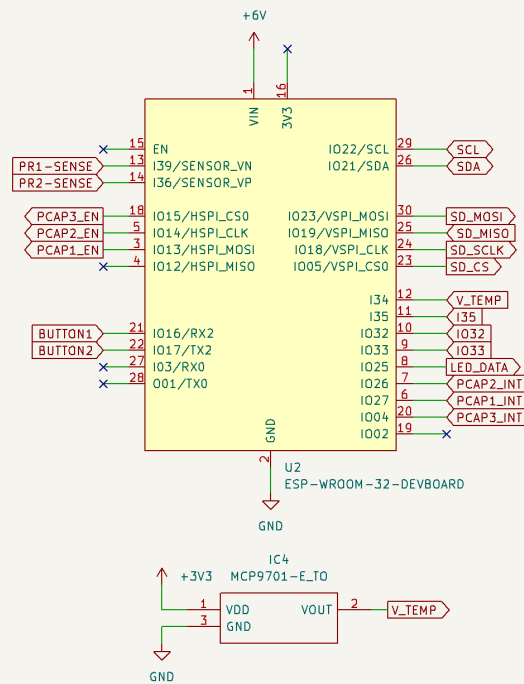
(a) Schematic design for the PCAP sensors



(b) Subsheet for PCAP-IC\_1 to PCAP-IC\_3

Figure A.2: PCAP04 integration schematics

## Microcontroller and temperature sensor



## Piezoresistive readout

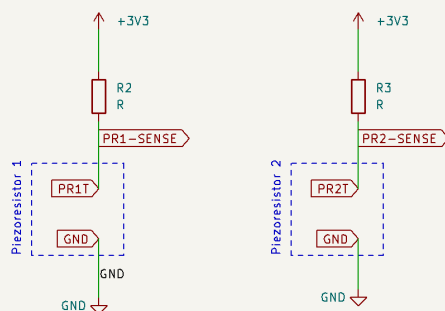


Figure A.3: Schematic design for the Microcontroller, temperature sensor and piezoresistive readout

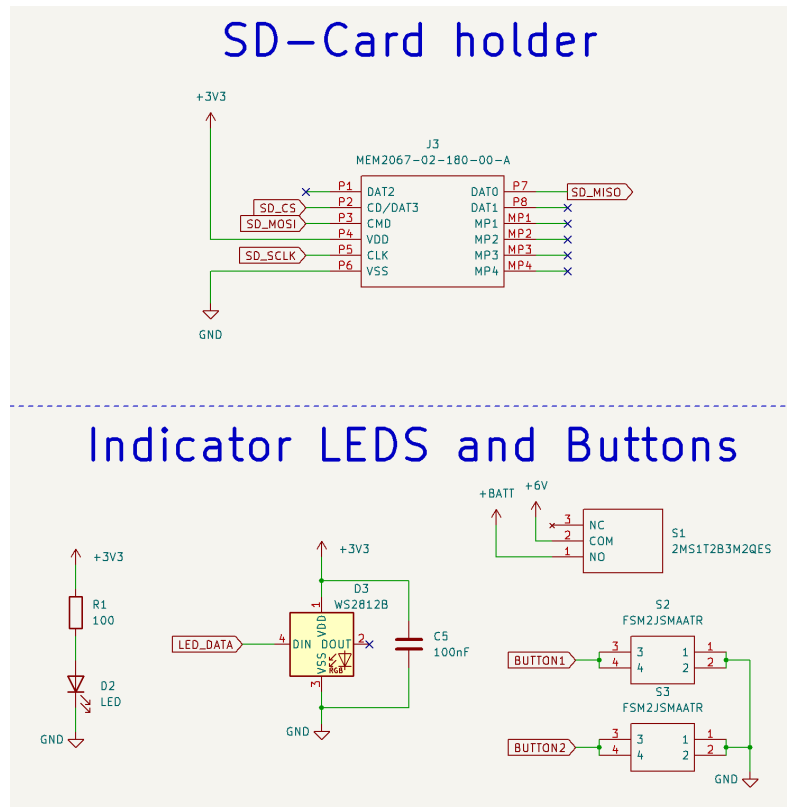


Figure A.4: Schematic design for the SD card slot, buttons and indicator lights

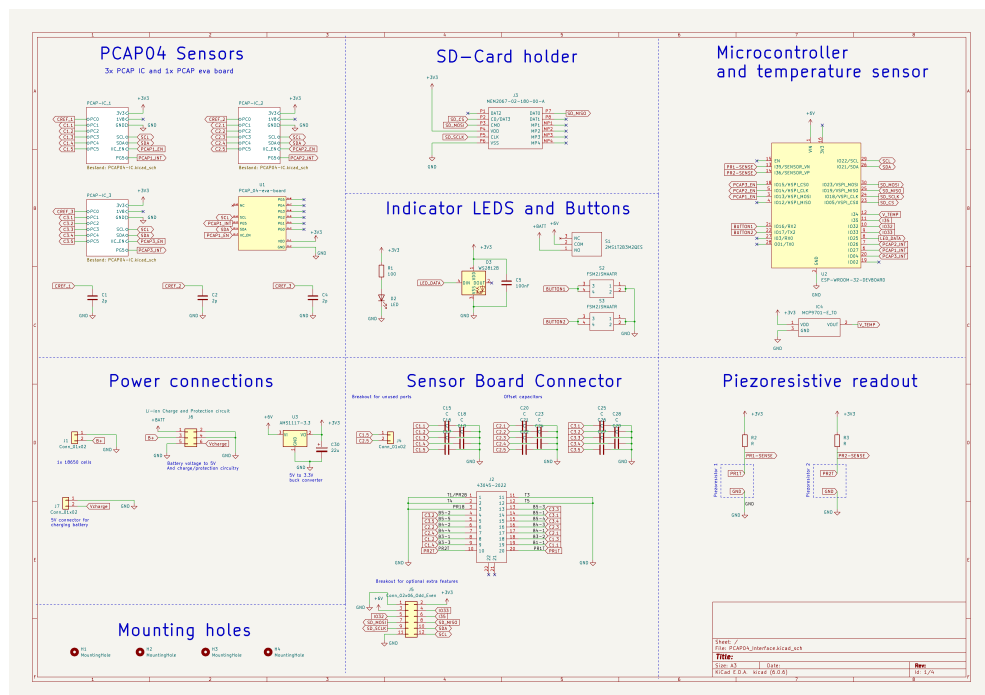


Figure A.5: Schematic design of the full PCB



